STUDY OF ULTRA-STRONG MAGNETIC PROPERTIES OF EXCHANGE-BIASED $Nd_4Fe_{76}Cu_{0.5}Nb_1B_{18.5}$ NANOCOMPOSITE ALLOYS

M. Phil Thesis

by

Taslima Akter

DEPARTMENT OF PHYSICS,
BANGLADESH UNIVERSITY OF ENGINEERING & TECHNOLOGY
DHAKA-1000, BANGLADESH
JUNE-2012

STUDY OF ULTRA-STRONG MAGNETIC PROPERTIES OF EXCHANGE-BIASED $Nd_4Fe_{76}Cu_{0.5}Nb_1B_{18.5}$ NANOCOMPOSITE ALLOYS

by

Taslima Akter
Roll No: 100614020
Session: October 2006

A THESIS SUBMITTED TO THE DEPARTMENT OF PHYSICS,
BANGLADESH UNIVERSITY OF ENGINEERING & TECHNOLOGY, DHAKA-1000
IN PARTIAL FULFILLMENT OF THE REQUIREMENT FOR THE DEGREE OF
MASTER OF PHILOSOPHY

DEPARTMENT OF PHYSICS,
BANGLADESH UNIVERSITY OF ENGINEERING & TECHNOLOGY
DHAKA-1000, BANGLADESH
JUNE-2012

BANGLADESH UNIVERSITY OF ENGINEERING & TECHNOLOGY
DEPARTMENT OF PHYSICS, DHAKA-1000, BANGLADESH

CERTIFICATION OF THESIS

The thesis titled **"STUDY OF ULTRA-STRONG MAGNETIC PROPERTIES OF EXCHANGE-BIASED $Nd_4Fe_{76}Cu_{0.5}Nb_1B_{18.5}$ NANOCOMPOSITE ALLOYS"** submitted by **Taslima Akter**, Roll No: 100614020, Session: October 2006, has been accepted as satisfactory in partial fulfillment of the requirement for the degree of **Master of Philosophy** in Physics on

BOARD OF EXAMINERS

1. (_____) Chairman
   Dr. Md. Feroz Alam Khan (Supervisor),
   Professor, Department of Physics, BUET.

2. (_____) Member
   Dr. Sheikh Manjura Hoque (Co-Supervisor),
   Principal Scientific Officer, Material Science Division, AECD

3. (_____) Member
   Head (Ex-Officio),
   Department of Physics, BUET.

4. (_____) Member
   Dr. Md. Abu Hashan Bhuiyan,
   Professor, Department of Physics, BUET.

5. (_____) Member

   (External)
   Dr. Md. Abdus Satter,
   Professor, Department of Physics, University of Dhaka.

CANDIDATE'S DECLARATION

It is, hereby declared that this thesis or any part of it has not been submitted elsewhere for the award of any degree or diploma.

Signature of the Candidate

....

(*Taslima Akter*)

To my parents and my most beloved ones

CONTENTS

List of Figures

List of Tables

List of Symbols

Anisotropy energy density	E_k
Azimuthal angle	ϕ
Anisotropy field	H_k
Anisotropy of the hard phase	K_k
Anisotropy of the soft phase	K_m
Average anisotropy	<K>
Broadening of diffraction line	B
Calorimetric constant	K
Coercivity	H_c
Critical exponent	b
Critical thickness of the hard phase	b_{ck}
Critical thickness of the soft phase	b_{cm}
Curie temperature	T_c
Curie temperature of residual amorphous matrix	T_c^{am}
DC field demagnetization remanence	$M_d(H)$
Diffraction angle	ɗ
Diametre of crystal partical	t
Differential heat flow rate	$Ý_m$
Energy per unit area of a 180° Bloch wall	ɔ
Enthalpy of crystallization	æH
Equilibrium energy per unit area of a 180° Bloch wall	$ɔ_o$
Equilibrium thickness of the Bloch wall	$ŭ_o$
Exchange correlation length	L_o
Exchange energy density	E_A
Exchange stiffness constant	A
Exchange-bias field	H_{ex}
Energy density	$\boldsymbol{E_{\gamma m}}$
Equilibrium energy density	$\boldsymbol{E_{\gamma ok}}$
Frequency	f
Full width at half maxima	FWHM
Grain size	D
Heating rate	ɓ
Inter planner spacing	d
Irreversible magnetic field	H_{irr}
Magnetization of the hard phase	M_{sk}
Magnetization of the soft phase	M_{sm}
Magnetization	M
Magnetocrystalline anisotropy constant	K_1
Maximum energy product	$(BH)_{max}$
Nucleation field	H_n

Number of turns	N
Packing fraction	p
Peak temperature	T_p
Permeability in vacuum	ε_o
Recoil permeability	ε_r
Remanent ratio	m_r
Resistance	R
Resistivity	Ɉ
Reversible magnetic field	H_{rev}
Reaction heat flow rate	$\acute{Y}_r$
Saturation magnetization	M_s
Saturation polarization	J_s
Skin depth	ŭ
Static magnetic field	H_{dc}
Susceptibility	ɢ
Saturation remanence vector	$ı^{lll}_{rj}$
Thikness of hard phase	b_k
Thikness of the Bloch wall	ŭ
Thikness of the soft phase	b_m
Total flux	ū
Temperature difference	æT
Total volume of material	V
Volume fraction of the hard phase	v_k
Volume fraction of the soft phase	v_m
Wavelength	ə

Acknowledgement

At first, my heartfelt respect to my Supervisor, Dr. Md. Feroz Alam Khan, Professor, Department of Physics, Bangladesh University of Engineering and Technology who is greatly acknowledged for his benevolent support. His excellent co-operation and constructive guidance helped me to overcome the hurdles many times during the period of my research work.

I want to offer my heartfelt gratitude and thereby acknowledge the memorable guidance of my honorable Co-supervisor, Dr. Sheikh Manjura Hoque, Principal Scientific Officer, Material Science Division(MSD), Atomic Energy Centre (AEC), Dhaka who has provided consistent support and kind help during the period of conducting my thesis work.

I would like to express my immense thanks to Prof. Dr. Md. Mostak Hossain, Head of the Department, Department of Physics, Bangladesh University of Engineering and Technology whose motivation and guideline helped me to make a right way of progress. My heartfelt thanks to Prof. Dr. Md. Abu Hashan Bhuiyan , Prof. Dr. Jiban Podder, Prof. Dr. A.K.M. Akther Hossain, and Mrs. Fahima Khanam, Associate Prof. of Department of Physics, Bangladesh University of Engineering and Technology whose encouragement and kind support was a great contribution for my advancement in the field of research. I also express thanks to Dr. Md. Rafi Uddin, Assistant Prof. and all other faculty members of the department.

I sincerely acknowledge and thank to ISP (International Science Programme) of Uppsala University, Sweden for their kind contribution to my research regarding sample preparation and different measurements.

Sincere thanks are expressed for the support provided by A.K.M. Abdul Hakim, Chief Engineer, Materials Science Division (MSD), Atomic Energy Centre (AEC), Dhaka (Retd.).

I am very much grateful to the Director of Atomic Energy Centre, Dhaka (AECD) for allowing me to use the laboratory facilities of Material Science Division (MSD), Atomic Energy Centre (AEC), Dhaka. My sincere thanks to all the laboratory assistants and office stuffs of the Department of Physics, BUET, who cooperated with me at each effort made to proceed my course work.

Thanks to my dearest friend, Israt Zerin who was beside me regarding my work. Special thanks to Subrata Roy whose sincere cooperation helped me to advance my efforts.

I want to express the selfless contribution of my family who are always with me at every footstep of my life till now and have always been the best inspiration and contributor for me.

Lastly, I would like to express my sincere gratitude to the authority of Bangladesh University of Engineering and Technology to kindly approve my M. Phil. project and to provide me all kinds of academic supports.

ABSTRACT

An amorphous alloy of composition $Nd_4Fe_{76}Cu_{0.5}Nb_1B_{18.5}$ prepared by melt spinning technique at wheel speed of 25 m/s in an argon atmosphere has been studied to observe their ultra-hard magnetic properties. In the as-prepared condition sample was in fully amorphous state as has been revealed by X-ray diffraction. Crystallization kinetics was studied by Differential Scanning Calorimetry. When the sample has been annealed above the crystallization temperature it has been devitrified and transformed into a composite consisting of two suitably dispersed ferromagnetic and mutually exchange-coupled phases, one of which is hard phase in order to provide a high coercive field while the other is soft-magnetic phase providing a high squareness ratio. At room temperature hysteresis loop measurements showed the highest value of coercivity H_c of around 3.30 kOe, which has been obtained for the sample annealed at 933K for 10 min. A large value of maximum energy product $(BH)_{max}$ and remanent ratio M_r/M_s of around 9.87 MGOe and 0.765 have been found respectively at this annealing temperature. The demagnetization branch of hysteresis loop is convex when the soft and hard phases are exchange coupled in the optimum condition of annealing. Otherwise, the hysteresis loops are constricted. At 5K the values of H_c and $(BH)_{max}$ are found as 6.02 kOe and 13.2 MGOe respectively for the sample annealed at 933K for 10 min. At temperatures below 150K, the shape of the hysteresis loops has been changed that is related to the spin reorientation in the hard magnetic phase. Otherwise, the hysteresis loops are constricted.

1.1 General Introduction

Discovering new behavior in small scale systems is one of the most exciting aspects of nano science. While new discoveries are difficult to predict, one fact is clear: as the size of a system is reduced to the atomic scale, quantum effects begin to dominate. One such effect is the exchange interaction, which generates spin coupling and magnetism in general. Therefore, one should expect spin and magnetism to be especially important at the nanometer length scale. Indeed, interlayer exchange coupling, giant magnetoresistance (GMR), tunneling magnetoresistance (TMR), spin momentum transfer, and other phenomena have been discovered in nanoscale magnetic systems. Not only are these discoveries fascinating from a scientific point of view, but they also have revolutionized information storage with high density hard drives and radiation hard, non-volatile memories.

In this thesis we investigate some of the scientific and technological aspects of nanostructured magnetic materials. Nanomaterials can be classified into nanocrystalline materials and nanocomposites. The former are polycrystalline bulk materials devitrified from the previously synthesized amorphous precursor through appropriate thermal treatment with grain sizes in the nanometer range (<100nm>) while the later refers to ultra-fine dispersive particles with diameters below 100 nm. The term nanostructured can be defined broadly as materials the structural features of which can be characterized in the range of 1-100 nm corresponding typically to ~50-5×10^7 atoms respectively. Nanocomposite magnetic materials have been developed through appropriate heat treatment of the initial amorphous precursors of Fe-Nd-B based alloys for the exchange spring behavior of hard magnets with high energy product and Fe-Si-B and Co-Si-B based alloys for the ultra-soft magnetic properties with extraordinary high permeability. My present composite material consists of two suitably dispersed and mutually exchange coupled phases. One of which is of soft-phases (m-type) that provides a high saturation magnetization and the other is a hard magnetic phase (k-type) providing coercive field for irreversible magnetization reversal. In this composite material, soft phases enveloped the hard phases to prevent corrosion. Such systems possess high remanence, high energy product $(BH)_{max}$ and reversible demagnetization curve which is called exchange-spring behavior.

The use of Nd-Fe-B magnets is now a dayôs exceeding that of other hard magnets and even some soft magnets .The reason is its increasing demand in global pc market where about

60% of these magnets goes into disc drive applications (primarily in VCMs). Recently magnetic motors are used in motor cars that are based on the penetration of NdFeB which requires a significant cost reduction, an increase in the maximum operating temperature, improvement in corrosion prevention and also reduction in volume and weight.

Here in this research work, we synthesize Fe-based alloys of the above mentioned composition using rapid solidification technique and study their magnetic properties with the evolution of different phases by varying annealing condition. To determine optimum condition of annealing, the Fe based hard nanocomposites were annealed in a vacuum system at different temperatures and holding time under a pressure of 10^{-5} mbar. To determine the crystallization temperature, differential scanning calorimetry was used. X-ray diffraction (CuKŬ) was used to identify the phases present in the samples at different stages of crystallization process. It helps to correlate evolution of nanograins, their volume fraction size and their distribution in the remaining amorphous matrix.

Our present research work is based on exchange spring magnet of composition $Nd_4Fe_{76}Cu_{0.5}Nb_1B_{18.5}$. The exchange spring was introduce by Kneller for nanocrystalline materials comprised of coupled hard and soft magnetic phases, the unique behavior of which is understood in terms of exchange interaction between the phases. In this chapter we will discuss in detail about exchange energy. An equation is derived from quantum mechanical principles that describe the exchange energy of a pair of electrons. In next section we explain different types of magnetic anisotropy, unixial and cubic. Magnetic behavior of permanent magnets depends on microstructural properties such as grain size, particleôs shape, grain boundary type and distribution of magnetically hard and soft phase. The properties of my present nanocomposite magnetic materials can be characterized by many ways: (1) by exchange biased soft and hard phases (2) by high energy product and (3) by high reduced remanence.

In the optimum condition of annealing, the soft phase of this composite would lead to high value of remanence which is expected to be greater than 0.5 while hard phase would lead to high value of coercivity that is expected to be greater than 3 kOe. For developing permanent magnet it is expected that remanent ratio would be greater than 0.5 [13].

1.2 Exchange Spring Behavior

The characteristic exchange-spring behavior results from the reversible rotation of the soft magnetic components for fields not large enough to reverse hard magnetic phase. Intergrain interactions are known to account for remanence enhancement in the composite materials. By using the demagnetization remanence (DCD) technique it has been demonstrated that when a negative field (lower than the critical field for magnetization reversal of the hard phase) is applied to previously saturated sample, a near-reversible rotation of soft phase magnetization is obtained when the field is decreased back to zero giving rise to high recoil permeability . The microscopic reversible and irreversible magnetic behavior in these materials exhibits relatively steep recoil curves with recoil permeability which is expected to be about 5 times as large as that of a conventional magnet with equal coercive field and saturation magnetization [1]. In any case, the exchange coupling between the phases produces a shape of the hysteresis loop like that of a uniform material showing no indication of the presence of two phases with extremely different magnetic hardness. The demagnetization branch of the hysteresis loop is convex. When the sample is over annealed over aging of the nanograins would lead to the demagnetization curve being concave. If there was no exchange coupling we would get a constricted loop [1].

1.3 Historical background

Normal magnets are strong permanent magnets (PMs) made from alloys of rare earth elements. Developed in the 1970s and 80s, rare-earth magnets are the strongest type of permanent magnets made, substantially stronger than ferrite or alnico magnets. The magnetic field typically produced by rare-earth magnets can be in excess of 1.4 teslas, whereas ferrite or ceramic magnets typically exhibit fields of 0.5 to 1 tesla. There are two types: neodymium magnets and samarium-cobalt magnets. Rare earth magnets are extremely brittle and also vulnerable to corrosion, so they are usually plated or coated to protect them from breaking and chipping. The term "rare earth" can be misleading as these metals are not particularly rare or precious; they are about as abundant as tin or lead, and as of 2007 rare earth magnets give the best cost/field ratios of any permanent magnet.

During the last three decades great progress regarding available energy density $(BH)_{max}$ has been achieved with the development of rare-earth PMs. The rare-earth elements are in general not rare at all, but their natural minerals are widely mixed compounds. To produce one particular rare-earth metal, several others, for which no commercial application exists,

have to be refined. This limits the availability of these metals. The first generation of these new alloys based on the composition S111C05 and invented in the 1960s has been commercially produced since the early 1970s. Today it is a well established hard magnetic material. SmCo5 has the advantage of high remanent flux density, high coercive force, high energy product, linear demagnetization curve and low temperature coefficient. The temperature coefficient of B_r is 0.03 to 0.045% /°C and the temperature coefficient of H_c is 0.14 to 0.40% /°C. Maximum service temperature is 300 to 350 UC. It is well suited to build motors with low volume, high power density and class of insulation F or H. The cost is the only drawback. Both Sm and Co are relatively expensive clue to their supply restrictions. With the discovery in the recent years of a second generation of rare-earth magnets on the basis of inexpensive neodymium (Nd), a remarkable progress with regard to lowering raw material costs has been achieved. This new generation of rare-earth PMs was announced by Sumitomo Special Metals, Japan, in 1983 at the 29th Annual Conference of Magnetism and Magnetic Materials held in Pittsburgh. The Nd is a much more abundant rare-earth clement than Sm. NdFeB magnets, which are now produced in increasing quantities have better magnetic properties than those of SmCo, but unfortunately only at room temperaure. The demagnetization curves, especially the coercive force, are strongly temperature dependent. The temperature coefficient of Br is -0.09 to -0.15% /°C and the temperature coefficient of H_c is -0.40 to -0.80% /°C. The maximum service temperature is 250°C and Curie temperature is 350°C. The NdFeB is also susceptible to corrosion. NdFeB magnets have great potential for considerably improving the performance-to-cost ratio for many applications. For this reason they will have a major impact on the development and application of permanent magnet (PM) apparatus in the future.

The latest grades of NdFeB have a higher remanent magnetic flux density and better thermal stability. Metallic or resin coating is employed to improve resistance to corrosion. Nowadays, for the industrial production of rare-earth PMs the powder metallurgical route is mainly used [200]. Neglecting some material specific parameters, this processing technology is, in general, the same for all rare-earth magnet materials. The alloys are produced by vacuum induction melting or by a calciothermic reduction of the oxides. The material is then size-reduced by crushing and milling to a single crystalline powder with particle sizes less than 10 fim. In order to obtain anisotropic PMs with the highest possible $(BH)_{max}$ value, the powders are then aligned in an external magnetic field, pressed and densified to nearly theoretical density by sintering.

1.4 Applications:

Since their prices became competitive in the 1990s, neodymium magnets have been replacing Alnico and ferrite magnets in many applications in modern technology requiring powerful magnets. Their greater strength allows smaller and lighter magnets to be used for a given application.

Nanocomposite magnets consisting of a uniform mixture of exchange coupled magnetically hard and soft phases have been extensively investigated in recent years because of their useful hard magnetic properties. High energy products and relatively high coercivities can be developed in these nanocomposite magnets. Among the advantages of these magnets are the high reduced remanence, m_r (= M_r / M_s), and low material cost due to the reduction in the content of the expensive hard magnetic phase. A small grain size (10-20 nm) and a uniform mixture of the two phases is a prerequisite for exchange coupling. This coupling leads to a smooth hysteresis loop in which the individual character of the constituent phases is concealed Fig.1.1. The challenge of preparing a suitable microstructure is most conveniently handled through non-equilibrium metallurgical techniques such as melt-spinning, mechanical alloying, and sputter deposition.

Common applications of rare-earth magnets include:

- computer hard drives
- audio speakers / headphones
- bicycle dynamos
- fishing reel brakes
- permanent magnet motors in cordless tools
- self-powered torches, employing rare earth magnets for generating electricity in a shaking motion

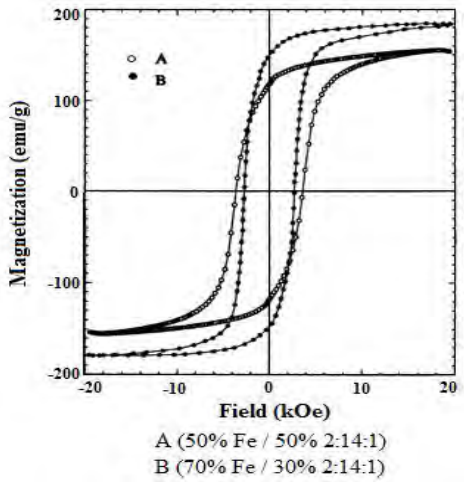

Fig.1.1: Hysteresis loops of Fe-rich Nd-Fe-B magnets.

(a) (b)

Fig.1.2: (a) Hard disks record data on a thin magnetic coating, (b) Magnetic hard separator for heavy minerals.

Magnetic recording media: VHS tapes contain a reel of magnetic tape. The information that makes up the video and sound is encoded on the magnetic coating on the tape. Common audio cassettes also rely on magnetic tape. Similarly, in computers, floppy disks and hard disks record data on a thin magnetic coating.

Speakers and microphones: Most speakers employ a permanent magnet and a current-carrying coil to convert electric energy (the signal) into mechanical energy (movement which creates the sound). The coil is wrapped around a bobbin attached to the speaker cone, and carries the signal as changing current which interacts with the field of the permanent magnet. The voice coil feels a magnetic force and in response moves the cone and pressurizes the neighboring air, thus generating sound. Dynamic microphones employ the

same concept, but in reverse. A microphone has a diaphragm or membrane attached to a coil of wire. The coil rests inside a specially shaped magnet. When sound vibrates the membrane, the coil is vibrated as well. As the coil moves through the magnetic field, a voltage is induced across the coil. This voltage drives a current in the wire that is characteristic of the original sound.

Electric motors and generators: Some electric motors rely upon a combination of an electromagnet and a permanent magnet, and much like loudspeakers; they convert electric energy into mechanical energy. A generator is the reverse: it converts mechanical energy into electric energy by moving a conductor through a magnetic field.

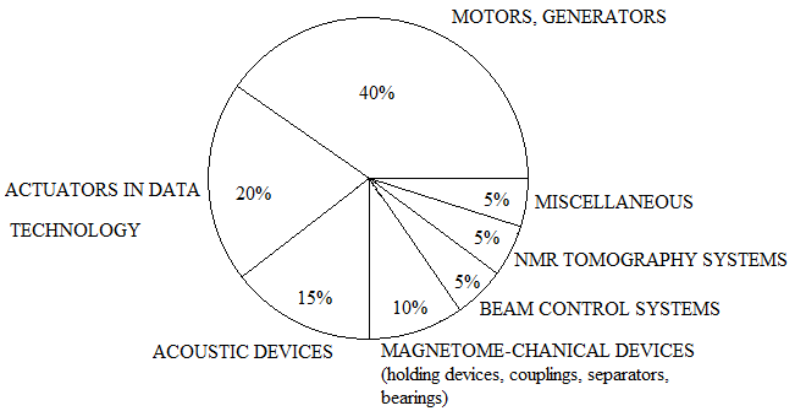

Fig.1.3: Fields of application of rare-earth PMs

1.5 Aim of the present research

a. Study of Fe-based hard nanocomposite magnetic materials where magnetic properties are characterized by exchange-coupled soft and hard nancomposite magnetic materials.
b. Determination of crystallization temperatures by differential scanning calorimetry.
c. Presence of soft and hard nanostructured materials by x-ray diffraction varying annealing condition.
d. Presence of soft phase would lead to high value of remanence, which is expected to be greater than 0.5 while presence of hard phase would lead to high value of coercivity which is expected to be greater than 3 kOe in the optimized annealing condition.
e. Extent of exchange coupling affects the shape of the hysteresis loop. The demagnetization branch of the hysteresis loop is convex when the soft and hard phases of the sample are exchange coupled in the optimum condition of annealing.
f. The recoil permeability of an exchange spring magnet is expected to be about 5 times as large as that of a conventional magnet with equal coercive field and saturation magnetization, which signifies reversibility of magnetic moment in the soft phase below certain critical field.
g. Reversible and irreversible component of magnetization can be studied from dc field demagnetization technique known as DCD technique and recoil hysteresis loops.
h. Temperature dependence of hysteresis loop parameters is expected to lead variation in the shape of the hysteresis loop in the low temperature region i.e. in the range of 5-150 K due to spin reorientation of magnetic moment of $Nd_2Fe_{14}B$ from 30° (from c-axis) to c-axis.

1.6 Review of researches on exchange –spring Magnet

D. Givord *et al*. [7] showed that in $Y_2Fe_{14}B$ and $Nd_2Fe_{14}B$ ferromagnets, 3D interactions are dominant. In $Y_2Fe_{14}B$, c-axis of the quadratic structure is of easy magnetization. The 3D anisotropy is an order of magnitude weaker than in YCo_5. At low temperature, the magnetization reorientation observed results from competition between exchange and anisotropy.

C.L. Harland *et al.* [12] reported that off-stoichiometric $Nd_9Fe_{86}B_5$ maintains a higher degree of interphase exchange coupling but only at low reverse fields; the stoichiometric $Nd_2Fe_{14}B$ maintains a lower degree of magnetic reversibility but sustains it to higher reverse fields.

S. Manjura Hoque *et al.* [13] reported that an amorphous alloys of different compositions such as $(NdPr)_4Fe_{71}Co_5Cu_{0.5}Nb_1B_{18.5}$ after appropriate annealing was found to show exchange spring behavior in the nanocrystalline state. Steep recoil curves of samples annealed at 873K and 973K show typical characteristics of the exchange-spring mechanism having smaller loop area. The temperature dependences of H_c, M_r/M_s and $(BH)_{max}$ in the range of 5 to 380K generally decrease with the increase of temperature. A change in the shape of the hysteresis loop was observed at temperatures below 100K related to spin reorientation in the hard magnetic phase.

M. Dahlgren *et al.* [14] found that the spin reorientation transitions T_{sr} of nanophase $Nd_2Fe_{14}B$ alloys were lower than that of bulk $Nd_2Fe_{14}B$. The smaller the grain size, the lower is T_{sr}. Also the coercivity of the nanophase Nd-Fe-B has less of a temperature dependence than sintered magnets.

I. Panagiotopoulos *et al.* [15] depicted that in case of melt-spun single-phase ($Nd_2Fe_{14}B$-type) and composite ($Nd_2Fe_{14}B$+Ŭ-Fe or $Nd_2Fe_{14}B+Fe_3B$+Ŭ-Fe), the reversibility of demagnetizing curves has been found to increase with increasing content of the soft phase of giving rise to the characteristic exchange-spring behavior only in nanocomposite samples. The relative strength of the magnetostastic interactions is increased in samples with higher soft phase contents.

D. Suess *et al.* [16] reported that exchange spring bilayer media can be optimized in order to achieve a high thermal stability without increasing coercive field. In grains with identical size and coercivity an optimized bilayer reaches an energy barrier exceeding those of optimized single phase media by more than a factor of two. Additionally the lower angular dependence of coercivity of exchange spring media will improve the signal to noise ratio in the magnetic recording system consisting of a hard/soft bilayer.

T. Schrefl *et al.* [17] described that the correlation between the microstructure and the magnetic properties of nanocrystalline permanent magnets. In isotropic nanocrystalline permanent magnets exchange interactions override the anisotropy of the individual grains.

Therefore, the spontaneous magnetic polarization deviates from the easy axes in a region along the grain boundaries. For a fine grain structure with a mean grain size d < 20 nm the remanence is considerably enhanced, since the volume fraction of the boundary regions where the spontaneous magnetic polarization points towards the direction of the applied field becomes significantly high. The inhomogeneous ground state, however, favors the nucleation of reversed domains leading to a direction of the coercive field with decreasing grain size. A uniform grain structure with a very small range in grain size avoids large demagnetizing fields and thus preserves a high coercivity. For a grain of 10 nm isotropic two-phase permanent magnets based on $Nd_2Fe_{14}B$ and Ŭ-Fe show remarkable high energy products, because the volume fraction of the magnetically soft phase can be increased up to 50% without a significant loss of coercivity.

1.7 Organization of the thesis work

An overview of permanent magnets is described in chapter-II. Chapter III depicts the theoretical basis of evolution of exchange spring behavior in the hard nanocomposite alloy along with different parameters like saturation remanence ratio (M_r/M_s), nucleation field $H_{no,}$ coercive field $H_{cM,}$ and volume fraction of phases in its microsturcture. The technological realization of exchange coupling also has been attempted to explain in Chapter III. Chapter IV contains the experimental details including differential Scanning Calorimetry (DSC), X-Ray Diffraction (XRD), Vibrating Sample Magnetometer (VSM) and Superconducting Quantum Interference Device (SQUID). Ribbons of Fe-based hard nanocomposite magnetic materials of the composition $Nd_4Fe_{76}Cu_{0.5}Nb_1B_{18.5}$, prepared by rapid solidification technique using melt spin machine will be studied thoroughly. Ingots of rare earth based hard magnetic materials will be prepared by arc melting the constituent element. Amorphous ribbons will be prepared from the ingot using a melt spin machine with a wheel speed of 25 m/s in an Ar atmosphere. Amorphosity of the ribbon and nanocrystalline structure will be studied by Philips XôPert Pro x-ray diffractometer with Cu K_α radiation. Studies of crystallization behavior will be performed using Differential Scanning Calorimetry (DSC). The ribbons of rare earth based compositions were heat treated in an evacuated quartz tube of 10^{-5} mbar pressure at different temperatures and times to observe the effect of annealing condition on the magnetic properties. Some of the magnetization measurements were performed in a Quantum Design MPMSXL5 Superconducting Quantum Interference Device (SQUID) magnetometer.

The details of the results regarding DSC, XRD method after heat treatment of the samples at different temperature, annealing effects on magnetization curve are discussed in Chapter-V. It also contains the analysis of total magnetization change in which irreversible portion of the exchange-spring system is obtained from the DCD curve and comments on the stability of the reversible state. The temperature dependence of hysteresis loops and their parameters are also discussed in this Chapter. Chapter-VI contains conclusions, achievement of works and future suggestions in connection with this research work.

2.1 Background:

Just like when the Greeks of the old times discovered the first naturally occurring magnetic stone, or natural magnet, we have been observing a property of matter called magnetism. Magnetism is the force of attraction or repulsion in a material. Certain materials such as iron, steel, nickel or magnetite exhibit this force while most other materials do not.

A magnet is any piece of iron, steel, or magnetite that has the property of attracting iron or steel. Magnetite, also known as lodestone, is a naturally occurring rock that is a magnet. This natural magnet was first discovered in a region known as magnesia and was named after the area in which it was discovered. Magnetism may be naturally present in a material or the material may be artificially magnetized by various methods. Magnets may be permanent or temporary. After being magnetized, a permanent magnet will retain the properties of magnetism indefinitely. A temporary magnet is a magnet made of soft iron that is usually easy to magnetize; however, temporary magnet lose most of its magnetic properties when the magnetizing cause is discontinued. Permanent magnet is more difficult to magnetize, but they remain magnetized. Materials which can be magnetized are called ferromagnetic materials.

2.2 Sources of Magnetism

Magnetism, at its root, arises from two sources:

- Electric current or more generally, moving electric charges create magnetic fields.
- Many particles have nonzero ñintrinsicò (or ñspinò) magnetic moment. Just as each particle, by its nature, has a certain mass and charge, each has certain magnetic moment, possibly zero.

In magnetic materials, sources of magnetization are the electronôs orbital angular motion around the nucleus and the electronôs intrinsic magnetic moment. The other potential sources of magnetism are the nuclear magnetic moments of the nuclei in the material which are typically thousands of times smaller than the electronôs magnetic moments. So they are negligible in context of the magnetization of materials.

Ordinarily, the countless electrons in a material are arranged such that their magnetic moments (both orbital and intrinsic) cancel out. This is due to some extent, the electrons combining into pairs with opposite intrinsic magnetic moments (as a result of the Pauli Exclusion Principle) or combining into ñfilled subshellsò zero net orbital motion; in both cases, the electron arrangement is so as to exactly cancel the magnetic moments from each

electron. Moreover, even when the electron configuration is such that there are unpaired electrons or non-filled subshells, it is often the case that the various electrons in the solid will contribute magnetic moments that points in different, random directions, so that the material will not be magnetic.

However, sometimes (either spontaneously or owing to an applied external magnetic field) each of the electron magnetic moments will be, on average, lined up. Then the material can produce a net total magnetic field, which can potentially be quite strong.

Magnetic behavior of a material depends on its structure (particularly its electron configuration) and also on temperature.

Magnetism, electricity, and special relativity

As a consequence of Einstein's theory of special relativity, electricity and magnetism are understood to be fundamentally interlinked. Both magnetism lacking electricity, and electricity without magnetism, are inconsistent with special relativity, due to such effects as length contraction, time dilation, and the fact that the magnetic force is velocity-dependent. However, when both electricity and magnetism are taken into account, the resulting theory (electromagnetism) is fully consistent with special relativity. In particular, a phenomenon that appears purely electric to one observer may be purely magnetic to another, or more generally the relative contributions of electricity and magnetism are dependent on the frame of reference. Thus, special relativity "mixes" electricity and magnetism into a single, inseparable phenomenon called electromagnetism (analogous to how relativity mixes" space and time into spacetime).

2.3 Types of magnetism

Diamagnetism:

Diamagnetism appears in all materials, and is the tendency of a material to oppose an applied magnetic field, and therefore, to be repelled by a magnetic field. However, in a material with paramagnetic properties (that is, with a tendency to enhance an external magnetic field), the paramagnetic properties dominates. Thus, despite its universal occurrence, diamagnetic behavior is observed only in a purely diamagnetic material. In a diamagnetic material, there are no unpaired electrons, so the intrinsic electron magnetic moments cannot produce any bulk effect. In these cases the magnetization arises from electronsô orbital motions, which can be understood classically as follows:

When a material is put in a magnetic field, the electrons circling the nucleus will experience. In addition to their coulomb attraction to the nucleus, a Lorentz force from the magnetic field. Depending on which direction the electron is orbiting, this force may increase the centripetal force on electrons, pulling them in towards the nucleus, or it may decrease the force, pulling them away from the nucleus. This effect systematically increases the orbital magnetic moments that were aligned opposite the field, and decreases the ones aligned parallel to the field (in accordance with Lenzôs law). This results in a small bulk magnetic moment, with an opposite direction to the applied field. This description is meant only as a heuristic; a proper understanding requires a quantum-mechanical description. All materials undergo this orbital response. However, in paramagnetic and ferromagnetic substances, the diamagnetic effect is overwhelmed by the much stronger effects caused by the unpaired electrons.

Paramagnetism:

In a paramagnetic material there are unpaired electrons, i.e. atomic or molecular orbital with exactly one electron in them. While paired electrons are required by the Pauli Exclusion Principle to have their intrinsic ('spin') magnetic moments pointing in opposite directions, causing their magnetic fields to cancel out, an unpaired electron is free to align its magnetic moment in any direction. When an external magnetic field is applied, these magnetic moments will tend to align themselves in the same direction as the applied field, thus reinforcing it.

Ferromagnetism:

A ferromagnet, like a paramagnetic substance, has unpaired electrons. However, in addition to the electrons' intrinsic magnetic moment's tendency to be parallel to an applied field, there is also in these materials a tendency for these magnetic moments to orient parallel to each other to maintain a lowered energy state. Thus, even when the applied field is removed, the electrons in the material maintain a parallel orientation.

Every ferromagnetic substance has its own individual temperature, called the Curie temperature, or Curie point, above which it loses its ferromagnetic properties. This is because the thermal tendency to disorder overwhelms the energy-lowering due to ferromagnetic order. Some well-known ferromagnetic materials that exhibit easily detectable magnetic properties (to form magnets) are nickel, iron, cobalt, gadolinium and their alloys.

Antiferromagnetism:

In an antiferromagnet, unlike a ferromagnet, there is a tendency for the intrinsic magnetic moments of neighboring valence electrons to point in opposite directions. When all atoms are arranged in a substance so that each neighbor is 'anti-aligned', the substance is antiferromagnetic. Antiferromagnets have a zero net magnetic moment, meaning no field is produced by them. Antiferromagnets are less common compared to the other types of behaviors, and are mostly observed at low temperatures. In varying temperatures, antiferromagnets can be seen to exhibit diamagnetic and ferrimagnetic properties. In some materials, neighboring electrons want to point in opposite directions, but there is no geometrical arrangement in which each pair of neighbors is anti-aligned. This is called a spin glass, and is an example of geometrical frustration.

Ferrimagnetism:

Like ferromagnetism, ferrimagnets retain their magnetization in the absence of a field. However, like antiferromagnets, neighboring pairs of electron spins like to point in opposite directions. These two properties are not contradictory, because in the optimal geometrical arrangement, there is more magnetic moment from the sublattice of electrons that point in one direction, than from the sublattice that point in the opposite direction.

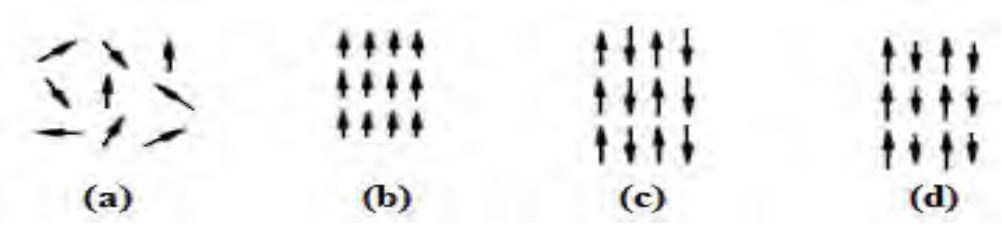

Fig.2.1: (a) Paramagnetic ordering (b) Ferromagnetic ordering
(c) Antiferromagnetic ordering (d) Ferrimagnetic ordering

Magnetic domains

The magnetic moment of atoms in a ferromagnetic material cause them to behave something like tiny permanent magnets. They stick together and align themselves into small regions of more or less uniform alignment called magnetic domains or Weiss domains. Magnetic domains can be observed with a magnetic force microscope to reveal magnetic

domain boundaries that resemble white lines in the sketch. There are many scientific experiments that can physically show magnetic fields.

When a domain contains too many molecules, it becomes unstable and divides into two domains aligned in opposite directions so that they stick together more stably as shown in Fig.2.2(a). When exposed to a magnetic field, the domain boundaries move so that the domains aligned with the magnetic field grow and dominate the structure as shown in Fig.2.2(b). When the magnetizing field is removed, the domains may not return to an unmagnetized state. This result in the ferromagnetic material's being magnetized, forming a permanent magnet.

When magnetized strongly enough that the prevailing domain overruns all others to result in only one single domain, the material is magnetically saturated. When a magnetized ferromagnetic material is heated to the Curie point temperature, the molecules are agitated to the point that the magnetic domains lose the organization and the magnetic properties they cause cease. When the material is cooled, this domain alignment structure spontaneously returns, in a manner roughly analogous to how a liquid can freeze into a crystalline solid.

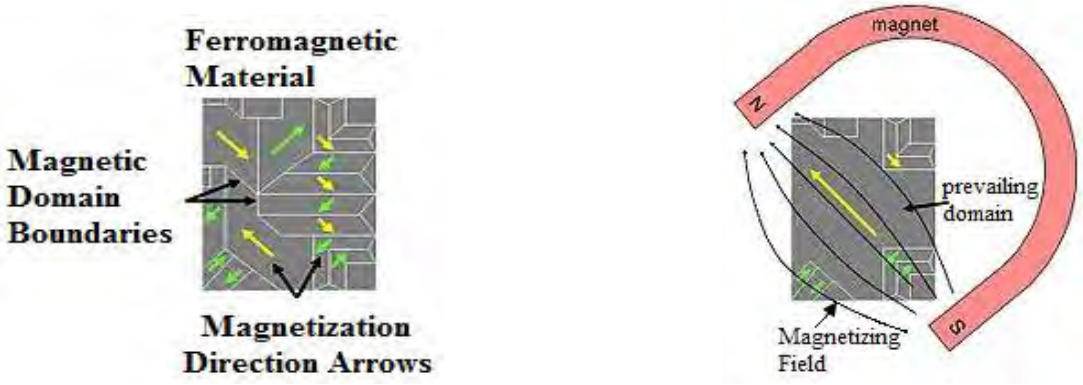

Fig.2.2: (a) Magnetic domains in ferromagnetic material (b) Effect of a magnet on the domains.

2.4 Relation between Magnetic fields and forces

The phenomenon of magnetism is "mediated" by the magnetic field. An electric current or magnetic dipole creates a magnetic field, and that field, in turn, imparts magnetic forces on other particles that are in the fields.

Maxwell's equations (which simplify to the Biot-Savart law in the case of steady currents) describe the origin and behavior of the fields that govern these forces. Therefore magnetism is seen whenever electrically charged particles in motion---for example, from movement of electrons in an electric current, or in certain cases from the orbital motion of electrons around an atom's nucleus. They also arise from "intrinsic" magnetic dipoles arising from quantum-mechanical spin.

The same situations that create magnetic fields (charge moving in a current or in an atom, and intrinsic magnetic dipoles) are also the situations in which a magnetic field has an effect, creating a force. When a charged particle moves through a magnetic field B, it feels a force F given by the cross product:

$$F = q\,(v \times B)$$

where q is the electric charge of the particle,
v is the velocity vector of the particle, and
B is the magnetic field.

Because this is a cross product, the force is perpendicular to both the motion of the particle and the magnetic field. It follows that the magnetic force does not work on the particle; it may change the direction of the particle's movement, but it cannot cause it to speed up or slow down. The magnitude of the force is

$$F = qv\,B\sin\theta$$

where ɗ is the angle between v and B.

One tool for determining the direction of the velocity vector of a moving charge, the magnetic field, and the force exerted is labeling the index finger "V", the middle finger "B", and the thumb "F" with your right hand. When making a gun-like configuration (with the middle finger crossing under the index finger), the fingers represent the velocity vector, magnetic field vector, and force vector, respectively.

Electromagnet

An electromagnet is a type of magnet whose magnetism is produced by the flow of electric current. The magnetic field disappears when the current ceases.

2.5 Magnetic dipoles and Magnetic monopoles

Magnetic dipoles

A very common source of magnetic field shown in nature is a dipole, with a "South pole" and a "North pole", terms dating back to the use of magnets as compasses, interacting with the Earthôs magnetic field to indicate North and South on the globe. Since opposite ends of magnets are attracted, the north pole of a magnet is attracted to the south pole of another magnet. The Earth's North magnetic pole (currently in the Arctic Ocean, north of Canada) is physically a south pole, as it attracts the north pole of a compass.

A magnetic field contains energy, and physical systems move toward configurations with lower energy. When diamagnetic material is placed in a magnetic field, a magnetic dipole tends to align itself in opposed polarity to that field, thereby lowering the net field strength. When ferromagnetic material is placed within a magnetic field, the magnetic dipoles align to the applied field, thus expanding the domain walls of the magnetic domains.

Magnetic monopoles

Since a bar magnet gets its ferromagnetism from electrons distributed evenly throughout the bar, when a bar magnet is cut in half, each of the resulting pieces is a smaller bar magnet. Even though a magnet is said to have a north pole and a south pole, these two poles cannot be separated from each other. A monopole ð if such a thing exists ð would be a new and fundamentally different kind of magnetic object. It would act as an isolated north pole, not attached to a south pole, or vice versa. Monopoles would carry "magnetic charge" analogous to electric charge. Despite systematic searches since 1931, as of 2006, they have never been observed, and could very well not exist.

Nevertheless, some theoretical physics models predict the existence of these magnetic monopoles. Paul Dirac observed in 1931 that, because electricity and magnetism show a certain symmetry, just as quantum theory predicts that individual positive or negative electric charges can be observed without the opposing charge, isolated South or North magnetic poles should be observable. Using quantum theory Dirac showed that if magnetic monopoles exist, then one could explain the quantization of electric charge-that is, why the

observed elementary particles carry charges that are multiples of the charge of the electron. Certain grand unified theories predict the existence of monopoles which, unlike elementary particles, are solitons (localized energy packets).

2.6 Origin of magnetism- two points of view

Microscopic origin of magnetism

Every electron, on account of its spin, is a small magnet (electron magnetic dipole moment). In most materials, the countless electrons have randomly oriented spins, leaving no magnetic effect on average. However, in a bar magnet many of the electron spins are aligned in the same direction, so they act cooperatively, creating a net magnetic field.

In addition to the electron's intrinsic magnetic field, there is sometimes an additional magnetic field that results from the electron's orbital motion around the nucleus. This effect is analogous to how a current-carrying loop of wire generates a magnetic field (Magnetic dipole). Again, ordinarily, the motion of the electrons is such that there is no average field from the material, but in certain conditions, the motion can line up so as to produce a measurable total field.

Quantum-mechanical origin of magnetism

In principle all kinds of magnetism originate from specific quantum-mechanical phenomena which are not easily explained (e.g. Mathematical formulation of quantum mechanics, in particular on the spin and on the Pauli principle). A successful model was developed already in 1927, by Walter Heitler and Fritz London, who derived quantum-mechanically, how hydrogen molecules are formed from hydrogen atoms, i.e. from the atomic hydrogen orbitals u_A and u_B centered at the nuclei A and B. That this leads to magnetism, is not at all obvious, but will be explained in the following.

According the Heitler-London theory, so-called two-body molecular ů-orbitals are formed, namely the resulting orbital is:

$$ı\,(r_{1,}\ r_1) = \frac{1}{\sqrt{2}} ıı_{1}ır_{1}\,ıı_{1}ır_{1}ı + ı_{1}ır_{1}\,ıı_{1}ır_{1}ıı$$

Here the last product means that a first electron, r_1, is in an atomic hydrogen-orbital centered at the second nucleus, whereas the second electron runs around the first nucleus. This "exchange" phenomenon is an expression for the quantum-mechanical property that particles with identical properties cannot be distinguished. It is specific not only for the formation of chemical bonds, but as we will see, also for magnetism, i.e. in this connection

the term exchange interaction arises, a term which is essential for the origin of magnetism, and which is stronger, roughly by factors 100 and even by 1000, than the energies arising from the electrodynamic dipole-dipole interaction.

As for the spin function σ(s_1,s_2), which is responsible for the magnetism, we have the already mentioned Pauli's principle, namely that a symmetric orbital (i.e. with the + sign as above) must be multiplied with an antisymmetric spin function (i.e. with a - sign), and vice versa. Thus:

$$\psi(s_1, s_2) = \frac{1}{\sqrt{2}}|\alpha_1 \beta_2| \pm |\beta_1 \alpha_2|,$$

i.e., not only u_A and u_B must be substituted by α and β, respectively (the first entity means "spin up", the second one "spin down"), but also the sign + by the ± sign, and finally r_i by the discrete values s_i (= ±½); thereby we have Ψ(+1/2) = β(−1/2) = 1 and Ψ(−1/2) = β(+1/2) = 0. The "singlet state", i.e. the - sign, means: the spins are antiparallel, i.e. for the solid we have antiferromagnetism, and for two-atomic molecules one has diamagnetism. The tendency to form a (homoeopolar) chemical bond (this means: the formation of a symmetric molecular orbital, i.e. with the + sign) results through the Pauli principle automatically in an antisymmetric spin state (i.e. with the - sign). In contrast, the Coulomb repulsion of the electrons, i.e., the tendency that they try to avoid each other by this repulsion, would lead to an antisymmetric orbital function (i.e. with the - sign) of these two particles, and complementary to a symmetric spin function (i.e. with the + sign, one of the so-called "triplet functions"). Thus, now the spins would be parallel (ferromagnetism in a solid, paramagnetism in two-atomic gases).

The last-mentioned tendency dominates in the metals Fe, Co and Ni, and in some rare earths, which are ferromagnetic, whereas most of the other metals, where the first-mentioned tendency dominates, are nonmagnetic (as e.g. Na, Al, and Mg) or antiferromagnetic (as e.g. Mn). Also the diatomic gases are almost exclusively diamagnetic and not paramagnetic (the oxygen molecule, because of the involvement of ´-orbitals, makes an exception). The Heitler-London considerations can be generalized to the Heisenberg model of magnetism (Heisenberg 1928). The explanation of the phenomena is thus essentially based on all subtleties of quantum mechanics, whereas the electrodynamics covers mainly the phenomenology.

Magnetization and demagnetization

Ferromagnetic materials can be magnetized in the following ways:

- Heating the object above its Curie temperature, allowing it to cool in a magnetic field and hammering it as it cools. This is the most effective method, and is similar to the industrial processes used to create permanent magnets.
- Placing the item in an external magnetic field will result in the item retaining some of the magnetism on removal. Vibration has been shown to increase the effect. Ferrous materials aligned with the Earth's magnetic field and which are subject to vibration (e.g., frame of a conveyor) have been shown to acquire significant residual magnetism. A magnetic field much stronger than the Earth's can be generated inside a solenoid by passing direct current through it.
- Stroking: An existing magnet is moved from one end of the item to the other repeatedly in the same direction.

Magnetized materials can be demagnetized in the following ways:

- Heating a magnet past its Curie temperature; the molecular motion destroys the alignment of the magnetic domains. This always removes all magnetization.
- Hammering or jarring: the mechanical disturbance tends to randomize the magnetic domains. Will leave some residual magnetization.
- Placing the magnet in an alternating magnetic field with intensity above the material's coercivity and then either slowly drawing the magnet out or slowly decreasing the magnetic field to zero. This is the principle used in commercial demagnetizers to demagnetize tools and erase credit cards and hard disk, and degaussing coils used to demagnetize CRTs.

2.7 Permanent Magnet

A permanent magnet is an object made from a material that is magnetized and creates its own persistent magnetic field. An everyday example is a refrigerator magnet used to hold notes on a refrigerator door. Materials that can be magnetized which are also the ones that are strongly attracted to a magnet are called ferromagnetic (or ferrimagnetic). These include iron, nickel, cobalt, some alloys of rare earth metals, and some naturally occurring minerals such as lodestone. Although ferromagnetic (and ferrimagnetic) materials are the only ones attracted to a magnet strongly enough to be commonly considered magnetic, all other substances respond weakly to a magnetic field by one of several other types of magnetism.

Ferromagnetic materials can be divided into magnetically "soft" materials like annealed iron which can be magnetized but don't tend to stay magnetized and magnetically "hard" materials, which do. Permanent magnets are made from "hard" ferromagnetic materials which are subjected to special processing in a powerful magnetic field during manufacture, to align their internal microcrystalline structure, making them very hard to demagnetize. To demagnetize a saturated magnet, a certain magnetic field must be applied and this threshold depends on coercivity of the respective material. "Hard" materials have high coercivity whereas "soft" materials have low coercivity.

An electromagnet is made from a coil of wire which acts as a magnet when an electric current passes through it, but stops being a magnet when the current stops. Often an electromagnet is wrapped around a core of ferromagnetic material like steel, which enhances the magnetic field produced by the coil. The overall strength of a magnet is measured by its magnetic moment, while the local strength of the magnetism in a material is measured by its magnetization.

2.8 Types of permanent magnets

Magnetic metallic elements

Many materials have unpaired electron spins, and the majority of these materials are paramagnetic. When the spins interact with each other in such a way that the spins align spontaneously, the materials are called ferromagnetic (what is often loosely termed as *magnetic*). Because of the way their regular crystalline atomic structure causes their spins to interact, some metals are (ferro) magnetic when found in their natural states, as ores. These include iron ore (magnetite or lodestone), cobalt and nickel, as well the rare earth metals gadolinium and dysprosium (when at a very low temperature). Such naturally occurring (ferro) magnets were used in the first experiments with magnetism. Technology has since expanded the availability of magnetic materials to include various man made products, all based, however, on naturally magnetic elements.

Composites

Ceramic or ferrite

Ceramic, or ferrite, magnets are made of a sintered composite of powdered iron oxide and barium/strontium carbonate ceramic. Given the low cost of the materials and manufacturing methods, inexpensive magnets (or non-magnetized ferromagnetic cores, for use in electronic component such as radio antennas, for example) of various shapes can be easily

mass-produced. The resulting magnets are non-corroding, but brittle and must be treated like other ceramics.

Alnico

Alnico magnets are made by casting or sintering a combination of aluminium, nickel and cobalt with iron and small amounts of other elements added to enhance the properties of the magnet. Sintering offers superior mechanical characteristics, whereas casting delivers higher magnetic fields and allows for the design of intricate shapes. Alnico magnets resist corrosion and have physical properties more forgiving than ferrite, but not quite as desirable as a metal.

Ticonal

Ticonal magnets are an alloy of titanium, cobalt, nickel, and aluminium, with iron and small amounts of other elements. It was developed by Philips for loudspeakers.

Injection molded

Injection molded magnets are a composite of various types of resin and magnetic powders, allowing parts of complex shapes to be manufactured by injection molding. The physical and magnetic properties of the product depend on the raw materials, but are generally lower in magnetic strength and resemble plastics in their physical properties.

Flexible

Flexible magnets are similar to injection molded magnets, using a flexible resin or binder such as vinyl, and produced in flat strips, shapes or sheets. These magnets are lower in magnetic strength but can be very flexible, depending on the binder used. Flexible magnets can be used in industrial printers.

Rare earth magnets

Rare earth (lanthanoid) elements have a partially occupied *f* electron shell (which can accommodate up to 14 electrons.) The spin of these electrons can be aligned, resulting in very strong magnetic fields, and therefore these elements are used in compact high-strength magnets where their higher price is not a concern. The most common types of rare earth magnets are samarium-cobalt and neodymium-iron-boron (NIB) magnets.

Single-molecule magnets (SMMs) and single-chain magnets (SCMs)

In the 1990s, it was discovered that certain molecules containing paramagnetic metal ions are capable of storing a magnetic moment at very low temperatures. These are very different from conventional magnets that store information at a magnetic domain level and theoretically could provide a far denser storage medium than conventional magnets. In this

direction research on monolayers of SMMs is currently under way. Very briefly, the two main attributes of an SMM are:

1. a large ground state spin value (S), which is provided by ferromagnetic or ferrimagnetic coupling between the paramagnetic metal centres.
2. a negative value of the anisotropy of the zero field splitting (D)

Most SMMs contain manganese, but can also be found with vanadium, iron, nickel and cobalt clusters. More recently it has been found that some chain systems can also display a magnetization which persists for long times at higher temperatures. These systems have been called single-chain magnets.

Nano-structured magnets

Some nano-structured materials exhibit energy waves called magnons that coalesce into a common ground state in the manner of a Bose-Einstein-condensate.

Costs

The current cheapest permanent magnets, allowing for field strengths, are flexible and ceramic magnets, but these are also among the weakest types. Neodymium-iron-boron (NIB) magnets are among the strongest. These cost more per kilogram than most other magnetic materials, but owing to their intense field, are smaller and cheaper in many applications.

Temperature

Temperature sensitivity varies, but when a magnet is heated to a temperature known as the Curie point, it loses all of its magnetism, even after cooling below that temperature. The magnets can often be remagnetized however. Additionally some magnets are brittle and can fracture at high temperatures.

2.9 Key Principles of Hard Magnetic Materials

Some important properties used to compare permanent magnets are: remanence (B_r), which measures the strength of the magnetic field; coercivity (H_{ci}), the material's resistance to becoming demagnetized; energy product (BH_{max}), the density of magnetic energy; and Curie temperature (T_c), the temperature at which the material loses its magnetism. Rare earth magnets have higher remanence, much higher coercivity and energy product, but (for neodymium) lower Curie temperature than other types.

Energy product $(BH)_{max}$: Also known as ñQuality productò, it is the product of the corresponding values of flux density B and field strength H on the demagnetization curve. Its maximum value is called the ñmaximum Quality productò or more briefly, the $(BH)_{max}$

value Fig.2.3. With the coercive field strength H_c and the remanence B_r, It is one of the most important characteristics of a permanent magnet material.

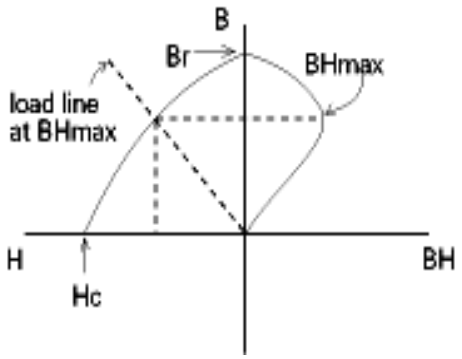

Fig 2.3: B-H Curve

B-H Curves

B-H curves may be plotted with the use of a permeameter. These curves completely characterize the magnetic properties of the material at a specific temperature. In order to plot a B-H curve, a sample of specific size must be used, then cycled through a magnetization/demagnetization cycle. This test is expensive to perform due to the length of time required to complete. The test is destructive to the sample piece in many cases, and is not practical to perform on a large sample of finished magnets. However, when magnets are machined from a larger block, the supplier may be requested to provide B-H curves for the starting raw stock of magnet material.

A good permanent magnet should produce a high magnetic field with a low mass, and should be stable against the influences which would demagnetize it. The desirable properties of such magnets are typically stated in terms of the remanence and coercivity of the magnet materials.

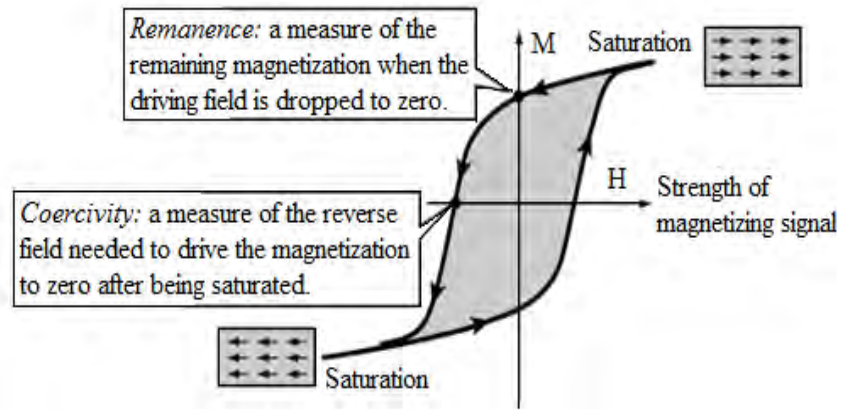

Fig.2.4: Hysteresis loop showing its remanence and coercivity.

When a ferromagnetic material is magnetized in one direction, it will not relax back to zero magnetization when the imposed magnetizing field is removed. The amount of magnetization it retains at zero driving fields is called its remanence. It must be driven back to zero by a field in the opposite direction; the amount of reverse driving field required to demagnetize it is called its coercivity. If an alternating magnetic field is applied to the material, its magnetization will trace out a loop called a hysteresis loop. The lack of retraceability of the magnetization curve is the property called hysteresis and it is related to the existence of magnetic domains in the material. Once the magnetic domains are reoriented, it takes some energy to turn them back again. This property of ferrromagnetic materials is useful as a magnetic "memory". Some compositions of ferromagnetic materials will retain an imposed magnetization indefinitely and are useful as "permanent magnets".

Interlayer Exchange Coupling

Discovering new behavior in small systems is one of the most exciting aspects of nanoscale science. While new discoveries are difficult to predict, one fact is clear: as the size of a system is reduced to the atomic scale, quantum effects begin to dominate. One such effect is the exchange interaction, which generates spin coupling and magnetism in general. Therefore, one should expect spin and magnetism to be especially important at the nanometer length scale.

It is well known that pairs of magnetic objects such as large bar magnets interact through magnetic fields that produce magnetic forces and torques. In the nanoscale regime, these magnetic dipolar interactions are still present, but a new phenomenon called interlayer exchange coupling can be even stronger. For two ultrathin magnetic films separated by a thin non-magnetic metal spacer, the two magnetic moments can interact by transmitting

spin-polarized electrons across the spacer. The net effect is to produce an exchange coupling between the two magnetic layers that can favor either parallel alignment or antiparallel alignment of their magnetizations. This behavior was discovered in 1986 by Grunberg (recognized by 2007 Nobel Prize) and is among the first important results in the modern field of spintronics. Just recently, interlayer exchange coupling was realized across an *insulating* spacer, specifically MgO. This is interesting because the transmission of spin-polarized electrons across the spacer is via *tunneling* instead of metallic conduction, and thus probes a new regime of exchange coupling.

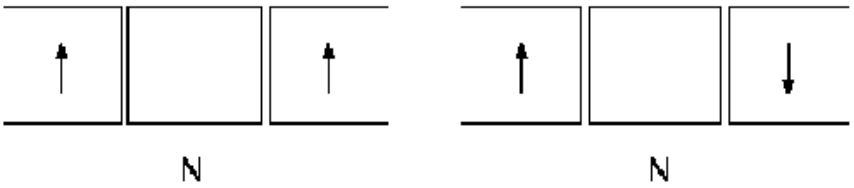

Fig.2.5: Interlayer exchange coupling

The greatest interest has been in the simplest form of the coupling, called bilinear because

$$E/A = - J\, m_1.m_2$$

the energy per area is linear in the directions of both magnetizations m_i, with this form of the interaction, positive values of the coupling constant J favor parallel alignment of the magnetizations and negative values favor antiparallel alignment.

Hysteresis

Hysteresis refers to systems that have memory, where the effects of the current input (or stimulus) to the system are experienced with a certain delay in time. Such a system may exhibit path dependence, or "rate-independent memory". Hysteresis phenomena occur in magnetic materials, ferromagnetic materials and ferroelectric materials, as well as in the elastic, electric, and magnetic behavior of materials, in which a lag occurs between the application and the removal of a force or field and its subsequent effect. Electric hysteresis occurs when applying a varying electric field and elastic hysteresis occurs in response to a varying force. The term "hysteresis" is sometimes used in other fields, such as economics or biology, where it describes a memory, or lagging effect.

When a ferromagnetic material is magnetized in one direction, it will not relax back to zero magnetization when the imposed magnetizing field is removed. It must be driven back to zero by a field in the opposite direction. If an alternating magnetic field is applied to the material, its magnetization will trace out a loop called a hysteresis loop. The lack of

retraceability of the magnetization curve is the property called hysteresis and it is related to the existence of magnetic domains in the material. Once the magnetic domains are reoriented, it takes some energy to turn them back again. This property of ferrromagnetic materials is useful as a magnetic "memory". Some compositions of ferromagnetic materials will retain an imposed magnetization indefinitely and are useful as "permanent magnets".

Hysteresis Loop

It is customary to plot the magnetization M of the sample as a function of the magnetic field strength H, since H is a measure of the externally applied field which drives the magnetization.

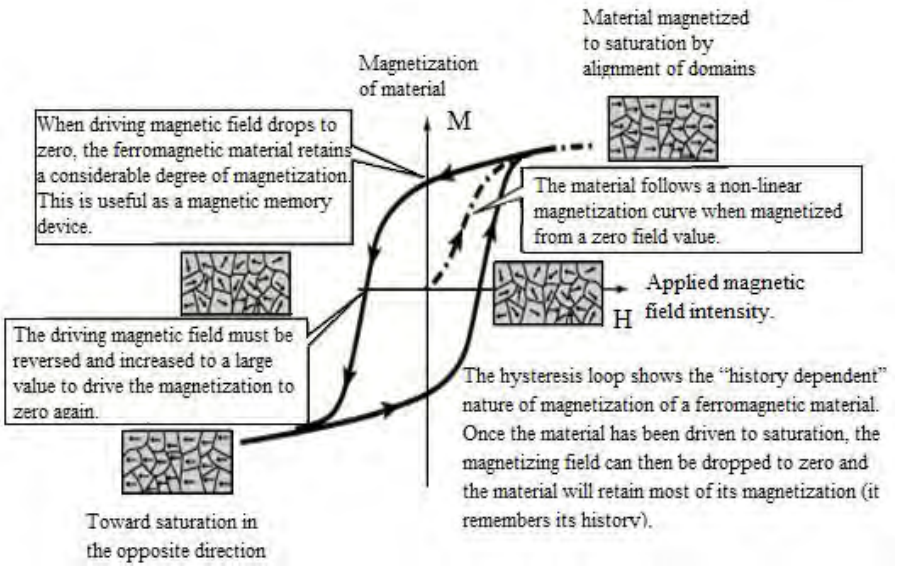

Fig.2.6: Magnetic ordering at different portions of a hysteresis loop

Variations in Hysteresis Curves

There is considerable variation in the hysteresis of different magnetic materials.

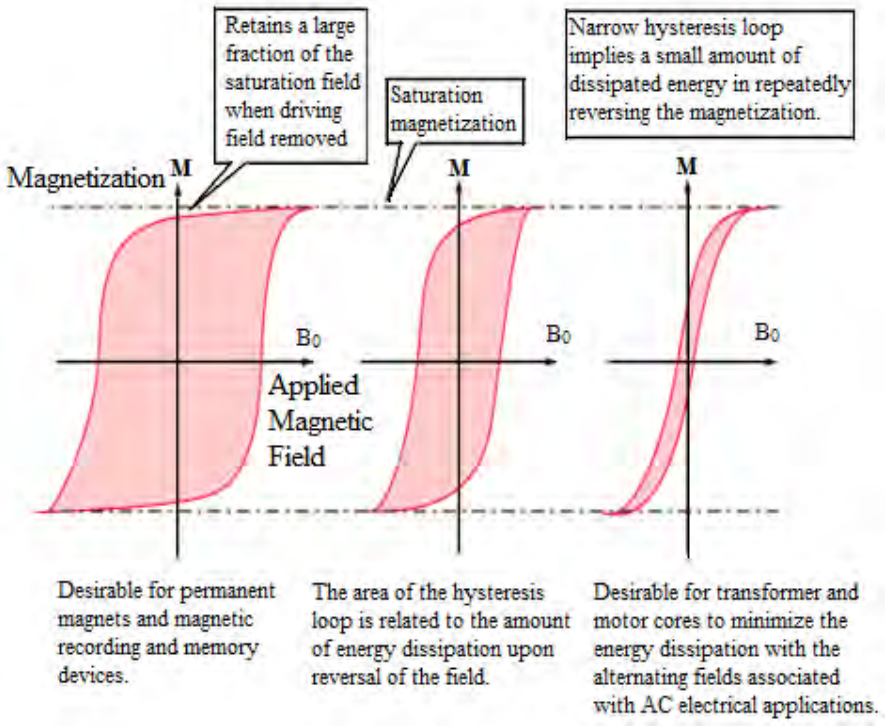

Fig.2.7: Hysteresis loops for different magnetic materials

3.1 Theoretical fundamentals of Differential Scanning Calorimetry (DSC)

The theory of DSC is discussed for both heat flux and power compensated instruments, temperature calibration and caloric calibration are described on the basis of thermodynamic principles. Estimation of the measurement curve in different ways is presented as a method for evaluating the curves of fast transitions.

In all DSCôs a temperature difference æT ï given as a voltage is the original measurement signal. In almost all instruments a heat flow rate $\acute{Y}_m$ (Differential heat flow rate) is internally assigned to. Independent of whether the user obtains or forms the respective DSC, knowledge of the functional relation between the measured signals (æT, $\acute{Y}_m$) and the quantity searched (the reaction heat flow rate $\acute{Y}_r$ consumed / produced by the sample) is important for:

- The time related assignment of $\acute{Y}_r$ to æT or $\acute{Y}_m$ (investigation in to the kinetics of a reaction)
- The determination of partial heats of reaction.
- The evolution and assessment of the influences of operating parameters and properties of the measuring system with regard to this relation.
- The estimate of the overall uncertainty of measurements.

The relation between $\acute{Y}_r$ and æT or $\acute{Y}_m$ can be derived in varying degrees of approximation to real DSC s. analytical solutions are possible only for simple boundary and initial conditions and for quasi ï steady ï states. Numerical procedures and solutions can approximate the actual conditions more exactly, however, without the clarity of the functional relations by an analytical solution. Basic considerations in this field are given by Gray, 1968.

To ensure better differentiation from $\acute{Y}_{r,}$ in the following section, æT of $\bar{u}_m$ is assumed to be the measurement signal, i.e. we search the relation $\acute{Y}_r$ (æT). The two quantities æT, $\acute{Y}_m$ are strictly proportional, with the expectation of the opposite Sign.

3.2 The theory of X-ray diffraction (XRD)

The X-ray diffraction (XRD) provides substantial information on the crystal structure. XRD is one of the oldest and effective tools for the determination of the atomic arrangement in a crystal. X ï rays are the electromagnetic waves whose wavelengths are in the neighborhood of 1Å. The wavelength of an X ï ray is thus of the same order of magnitude as the lattice constant of crystals and it is this which makes X ï rays so useful in structural analysis of crystal.

Whenever x-rays are incident on a crystal surface, they are reflected from it. The reflection abides by the Braggôs law is given below

$$2d \sin\theta = n\lambda$$

Where d is the distance between two successive crystal planes, ɗ is the glancing angle; ə is the wavelength of the X ï ray and n is the positive integer. Braggôs law also suggested that the diffraction is only possible when ə < 2d.

X ï ray diffractograms of all the samples were recorded using monochromatic Cu KŬ ï radiation (ə = 1.54053 Å) to ensure the formation of single ï phase nature of the sintered product. XRD pattern information is: scanning speed 2º, chart speed 20 mm starting from 20º and ending at 90º. Peak intensities are recorded corresponding to their 2ɗ values. The interplanner distances d were calculated from these 2ɗ values of the diffraction peaks using the Braggôs law.

3.3 Determination Of Nanometric Grain Size By X-Ray Diffraction

Nanocrystalline alloys are basically crystalline, and because of their crystallinity they exhibit Bragg scattering peaks in X-ray diffraction experiments. However, due to their small size, significant fine particle broadening is observed in the Bragg peaks. The X-ray scattering from a crystalline solid is given by Braggôs low:

$$2d \sin\theta = n\lambda \qquad (1)$$

This equates the path difference of X-rays scattered from parallel crystalline planes spaced d = d_{hkl} apart to an integral number (n) of X-ray wavelength ə. Here ɗ is the X-ray angle of incidence (and of diffraction) measured with respect to the crystalline planes. For an infinite crystal Bragg scattering occurs at discrete values of 2ɗ satisfying the Bragg condition, i.e. Bragg peaks are ŭ-functions. For finite sized crystals the peaks are broadened over a range of angles as shown in Fig.3.1.

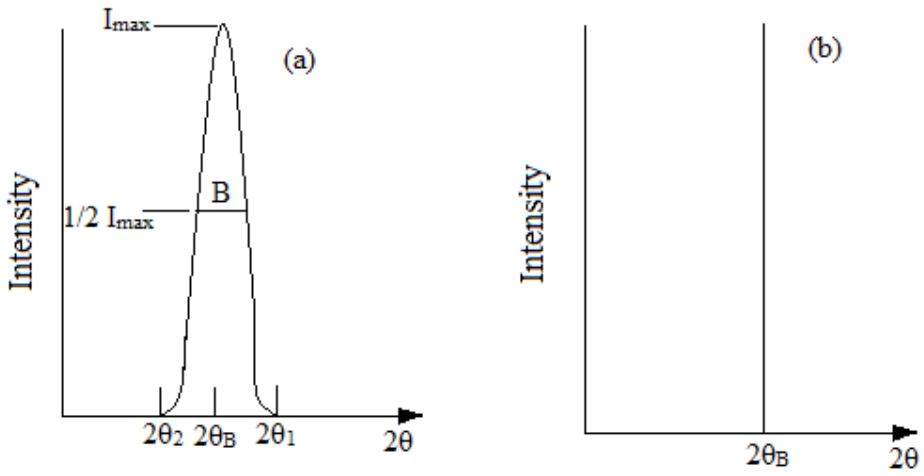

Fig.3.1: Effect of fine particle broadening in XRD (a) fine particles and (b) perfect crystal.

To better understand the phenomenon of fine particle broadening following the arguments of B. D. Cullity, is outline below. We consider a finite crystal of thickness, $D_g = m.d$, where m is an integer, and d is the distance between crystalline planes, i.e. there are m planes in D_g. Considering Fig.3.1 if the broadened Bragg peak begins at an angle $2\theta_2$ and ends at $2\theta_1$, the breadth of the peak or full width at half maximum is given as:

$$\beta = \frac{1}{1}(2\theta_1 - 2\theta_2) = \theta_1 - \theta_2 \qquad \text{(a)}$$

Now consider the path differences for each of the two angles θ_1 and θ_2, for X-rays traveling through the full thickness of the crystal. The width β is usually measured in radians, an intensity equal to half the maximum intensity. As a rough measure of β we can take half the differences between the two extreme angles at which the intensity is zero, which amounts to assuming that the diffraction line is triangular in shape. We now write path difference between adjacent planes.

$$2D_g \sin\theta_1 = (m+1)\lambda \qquad \text{(b)}$$

$$2D_g \sin\theta_2 = (m-1)\lambda \qquad \text{(c)}$$

By subtraction we find:

$$D_g \sin(\theta_1 - \theta_2) = \lambda \qquad \text{(d)}$$

$$D_g 2\cos\left(\frac{\theta_1+\theta_2}{1}\right)\sin\left(\frac{\theta_1-\theta_2}{1}\right) = \lambda \qquad \text{(e)}$$

But θ_1 and θ_2 are both very nearly equal to θ, so that $\theta_1 + \theta_2 \approx 2\theta$ and $\sin\left(\frac{\theta_1-\theta_2}{1}\right) \approx \left(\frac{\theta_1-\theta_2}{1}\right)$ so that equation (e) can be written as:

$$2D_g\cos\left(\frac{\theta_1+\theta_2}{1}\right) = \lambda \qquad \text{(f)}$$

From equation (a) and equation (f) we get:

$$\beta . D_g \cos\theta = \lambda$$

$$D_g = \frac{1}{1\,1\,1\,1\,1} \qquad (g)$$

A more exact empirical treatment yields:

$$D_g = \frac{1\ 1}{1\,1\,1\,1\,1} \qquad (h)$$

$$D_g = \frac{1\ .1\ 1}{1\,1\,1\,1\,1} \qquad (i)$$

Here K is a dimensionless constant that may range from 0.89 to 1.39 depending on the specific geometry of the scattering objects. This is known as the Scherrerôs formula. It is used to estimate the particle size of very small crystals from the measured width of their diffraction curves.

3.4 Exchange-spring systems

Exchange spring systems are magnetic heterostructures that consists of magnetically soft and hard compounds that are exchange coupled across the compound interfaces. Various nanostructures have been devised, typically clustered structures where hard inclusions are embedded into a soft matrix (Fig.3.2a), or multilayered systems of alternating hard and soft layers (Fig.3.2b). In the following we will focus on the former.

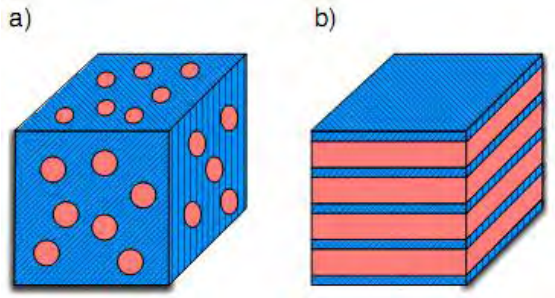

Fig.3.2: Types of exchange spring system, with magnetically hard (red) and soft (blue) materials. (a) Clustered structured (b) Multilayered structured.

3.5 Exchange Energy

The conduction energy band and the energy band of the valence electrons overlap in conductors, so that a fraction of the valence electrons can freely move around the solid state as conduction electrons (Kittel 1996, chap7). The remaining valence electrons are bound to the ions into the lattice. There quantum mechanical wave functions are extending to a distance of the respective nucleus depending on the orbital they are allocated at. Thus, they overlap with electrons of neighboring ions, causing a additional energy term that is purely of quantum mechanical nature and that has no classical equivalent. It will be shown that the exchange interaction favors alignment of neighboring electron spins. This energy is extremely short-ranged, as the electron wave function decays exponentially. Together with the long-ranged dipolar interaction, the exchange interaction is responsible for the formation of domains, a phenomenon that stretches to almost microscopic length-scales. In this respect, the observation of domains reveals the quantum mechanical foundation of nature.

3.6 Anisotropy Energy

When a physical property of a material is a directional function, this property is said to exhibit anisotropy. The preference for the magnetization to lie in a particular direction of a sample is called magnetic anisotropy. There are different kinds of anisotropies in the context of magnetism: magnetocrystalline, strain induced, shape and surface anisotropy. One anisotropy considered here, the magnetocrystalline anisotropy, has its origin in the crystal symmetry of the sample and the *LS* coupling (or spin-orbit coupling) of the electron angular momenta: the crystallographic structure influences the shape and orientation of the electron orbits. This in turn, affects the electron spins via the LS coupling in a way that the spins tend to align along the crystallographic axes. When the spontaneous magnetization exhibits a preferred direction this is evidently a minimum- energy position for it. Thus we may argue that, if the magnetization is rotated out of this direction by the application of a field, there must be an increase of energy, in the material, which we describe as the anisotropy energy. In absolute terms we may write down an expression for the total free energy of a crystal as a sum of a number of terms. These terms include the usual thermodynamic ones of enthalpy and entropy and, for a magnetic crystal, also the magnetic energy. The anisotropy energy is a further term which will vary with the angle, ϕ, by which the magnetization deviates from a preferred direction, being zero for $\phi = 0$. The simplest view, however, is to regard this as the energy which must be supplied in order to rotate the magnetization through the angle ϕ.

3.7 Phenomenology of Anisotropy

Experiments reveal the character of the anisotropy for different materials: when an external field is used to magnetize a probe, the magnetization process depends on the angle between the applied field and a crystal reference direction, e.g. in iron, the magnetization process is said to easy in the [110] direction (along the edge of the crystal cell), and hard in the [111] direction (along the body diagonal of the crystal cell); that is, the field needed to magnetize iron to saturation in smaller in [100] than in any other direction (Fig.3.3 in the following page).

The anisotropy energy density $\mathring{U}_a$ is defined as the energy density difference required to saturate a sample (saturation magnetization M_s) alongside a given direction and alongside a hard axis (shaded area in the plots of Fig.3.3). Different sample materials with different crystal symmetry show different anisotropy types. The anisotropy types are now discussed (*O, Handley, 1999*).

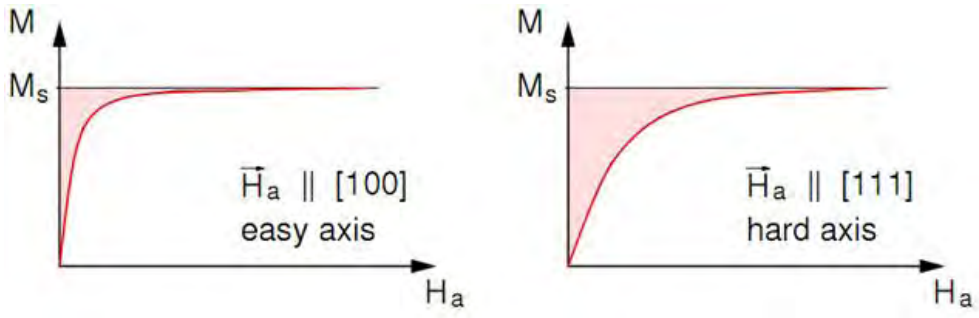

Fig.3.3: Schematic hysteresis loops of a material with an easy axis in [100] and a hard axis in [111], *e.g.* iron. The left plot shows the function of the magnetization M over the applied field H_a along the easy axis, the right plot along the hard axis. The shaded area in each plot indicates the energy required to magnetize the sample up to saturation.

3.8 Uniaxial anisotropy

The simplest case in a uniaxial anisotropy, as observed in cobalt: Magnetic measurements for different directions suggest the existence of an axis that minimizes the anisotropy energy. Plotting the anisotropy energy as function of the angle ɗ enclosed by this easy axis (defined as the z axis, without loss of generality) and the magnetization, shows a onefold symmetry Fig.3.4. The anisotropy energy does not depend on the azimuthal angle ϕ in this system, and it is maximal in the basal plane (ɗ = 90°), the hard plane.

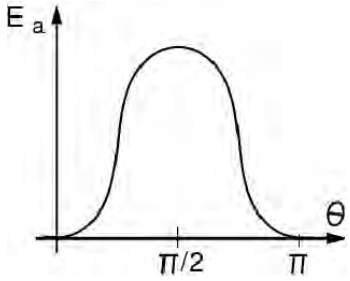

Fig.3.4: Sketches of the anisotropy energy, as a 2D plot over ɗ

3.9 Cubic anisotropy

Most materials, i.e. iron and nickel, does not feature the simple and easy-to-handle the uniaxial anisotropy due to the nature of their crystal lattice structure. Experiment reveals that these materials bear the cubic anisotropy. Here the anisotropy depends on the three angles ɔ1ɔ2ɔ3 (Fig.3.5) rather than one angle ɗ. Measurement of the anisotropy in the basal plane show a fourfold symmetry (Fig.3.6) with either an easy axis for $\phi = 0°$ (i.e. iron, 3.6a), or a hard axis (i.e. nickel, 3.6b).

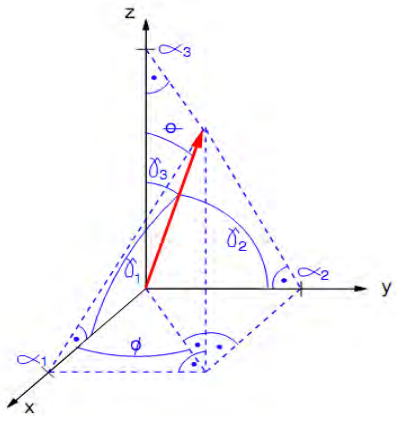

Fig.3.5: Definition of Ŭi in a Cartesian coordinate system (black): the Ŭi are the projection lengths of a unit vector (red) onto the coordinate axes. The angles enclosing the unit vector and the coordinate axes are named: ɔi. The spherical coordinates ϕ and ɗ are depicted as well. Projection lines and angles are displayed in blue clour.

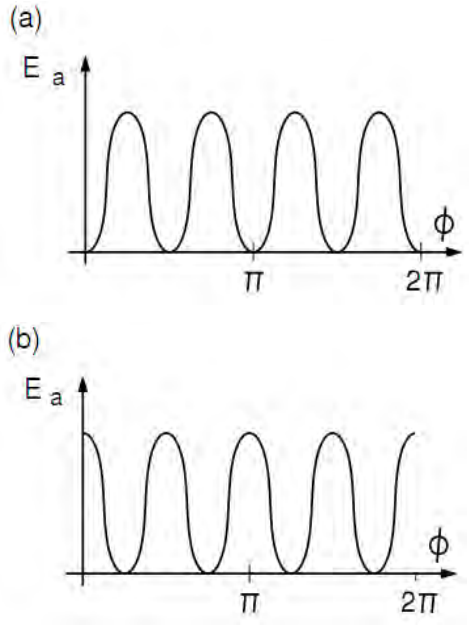

Fig.3.6: Schematic result of an in-plane measurement of the anisotropy energy as a function of the azimuthal angle ϕ.

3.10 Fe-based hard nanocomposite magnetic materials

Nanocomposite magnetic materials exhibits Exchange ï Spring behavior, which results from the reversible rotation of soft magnetic component for field not large enough to reverse the hard magnetic phase. Recently, isotropic nanocrystalline magnetic materials with uniaxial anisotropy have been found to have a remanence to saturation magnetization ratio above the value of M_r/M_s = 0.5 predicted by Stoner-Wohlfarth model [15]. This remanence enhancement is attributed to intergrain exchange interactions [11,17,20] and it has been observed both in single-phase [11,17] and nanocomposite materials consisting of a fine mixture of soft and hard phases [1,10,21]. Exchange coupling between the phases allows one to optimize the magnetic properties of nanocomposite magnets by combining the high magnetization due to the presence of the soft phases with the high anisotropy of the hard phase. Kneller and Hawing [1] has provided the theory of the Exchange spring behavior of Fe_3B/Nd_2Fe_4B based alloy. A brief review on theoretical aspect has been presented below.

The theoretical limit for the maximum energy product of a given material is expressed by the following equation

$$(BH)_{max} \leq 1_1^1/4\mu_o \text{ é é é é é é é é é é é é é é ..(1)}$$

From this equation it is seen that maximum energy product $(BH)_{max}$ depends only on its saturation polarization $1_1 = \mu_o M_s$. Besides this, the following conditions also govern the

value of maximum energy product $B_r = ı_1$ that requires the solid ferromagnetic materials i.e. packing fraction $P = 1$ and alignment of the easy axis parallel to the field axis, critical field for irreversible magnetization reversible i.e. nucleation field $H_n \geq ı_1/2\mu_o = M_s/2$. According these conditions, the limit (1) may in principle be reached only with materials that have a sufficiently high nonplanar magnetocrystallines anisotropy constant. The magnitude of the ratio $k = ı /(ı_1^1/4\mu_o) = 4K/\mu_o M_s^2$ characterizes the basic magnetic behavior of the material. The magnetic behavior is dominated by magnetocrystalline anisotropy when k >> 1, such materials are called hard magnetic (k material). If k << 1, the behavior is governed by magnetostatic energy and such materials are called soft magnetic (m-material). In these terms limit (1) is attainable only with k-material.

It is found that most of the hard magnetic materials possess, saturation magnetization ($J_ı$) lower than for many common m-materials whereas the coercivity H_{cM} of (*k*-material) hard magnetic material may exceed the value $M_s/2$ necessary to reach the limit of the equation (1). Moreover the best of the hard magnetic material contain about 25 wt % or more of a rare-earth metal which creates (raises) serious problems with respect to chemical stability and also raises the cost (add to their high price) of the materials while most of the soft magnetic materials are much less reactive and inexpensive. In this composite, hard phase contain the rare earth element and the soft phase envelops the hard phase to prevent their corrosion. Therefore composite materials of soft and hard phase are inexpensive and less coercive.

Therefore it is considered that composite materials consist of two suitably dispersed and exchange coupled phases one of which is of the hard phase and the other is of a soft phase. The former provides a high enough nucleation field for irreversible magnetization reversible and the later provides a high saturation magnetization M_s.

Knller and Hawing [1], in their research work, first estimate the critical dimension of the phases and discuss corresponding models of microstructure. On that basis they derived the typical magnetic properties of such composites. Finally they have shown how a material of this kind may be realized technologically and magnetic behavior corresponds entirely to the prediction of the theory.

3.11 Microstructure

The microstructure must be such as to permit no easy (low energy) mechanism of irreversible magnetization reversal in either of the phases. Let us consider a one dimensional model in Fig. 3.7 in order to derive a rough estimate of the corresponding

critical dimension of the phases. This model consisting of a sequence along x axis of alternating hard (k-phase) and soft phase (m-phase), regions of width $2b_k$ and $2b_m$ respectively which are crystallographically coherent and exchange coupled through the phase boundaries [1].

The magnetocrystalline anisotropy is assumed uniaxial (for simplicity) in both phases, with both easy axes being parallel to the z axis perpendicular to x. The anisotropy energy density depends on the angle ū between ı̈ı̈ı and the easy axis as

$$E_k = K \sin^2 \Phi \quad \text{é é é é é é é é é é é é é é .. (2)}$$

Where $K > 0$. As per definition it may be mentioned that for the k-phase $k_k = 4K_k / \mu_o$ı $_{11}^{1}$ $>> 1$ and for the m-phase $k_m = 4K_m/\mu_o$ı $_{11}^{1}$ $<< 1$. The ratio k_k/k_m is of the order of 10^2 to10^3 according to table (3.1). This is due mainly to the magnitude of the ratio K_k/K_m of the order of 10^2. The values of M_{sk} and M_{sm} are mostly of the same order, with the ratio ı $_{11}^{1}$ /ı $_{11}^{1}$ not exceeding 10 in practical case. The exchange energy density may be written in the form

$$E_A = A\,(d\psi/dx)^2 \quad \text{é é é é é é é é é é é é é é (3)}$$

Where A is a constant of the order 10^{-11} J/m at room temperature. A depends on the curie temperature, T_c and on temperature T as $A \propto T_c\,[M_s(T)/M_s(o)]^2$ and ψ is for the present model the angle between M_s and z-axis in the yz plane. With the questions, the energy per unit area of a 180° Bloch Wall in a homogeneous material may be written approximately as,

$$\gamma \backsimeq \delta K + \delta A(\pi/\delta)^2 \quad \text{é é é é é é é é é é é é é .. (4)}$$

where δ is the wall thickness. In equilibrium $\gamma(\delta)$ has a minimum $(d\gamma/d\delta = 0)$, from where the equilibrium quantities δ_o, γ_o are obtained:

$$\delta_o \backsimeq \pi(A/K)^{1/2} \quad \text{é é é é é é é é é é é é é é é (5)}$$

$$\gamma_o \backsimeq 2\pi(A.K)^{1/2} \quad \text{é é é é é é é é é é é é é é ... (6)}$$

Critical dimensions for a high energy magnetization reversal in the one-dimensional system in Fig.3.7 are obtained from a consideration of the reversal process.

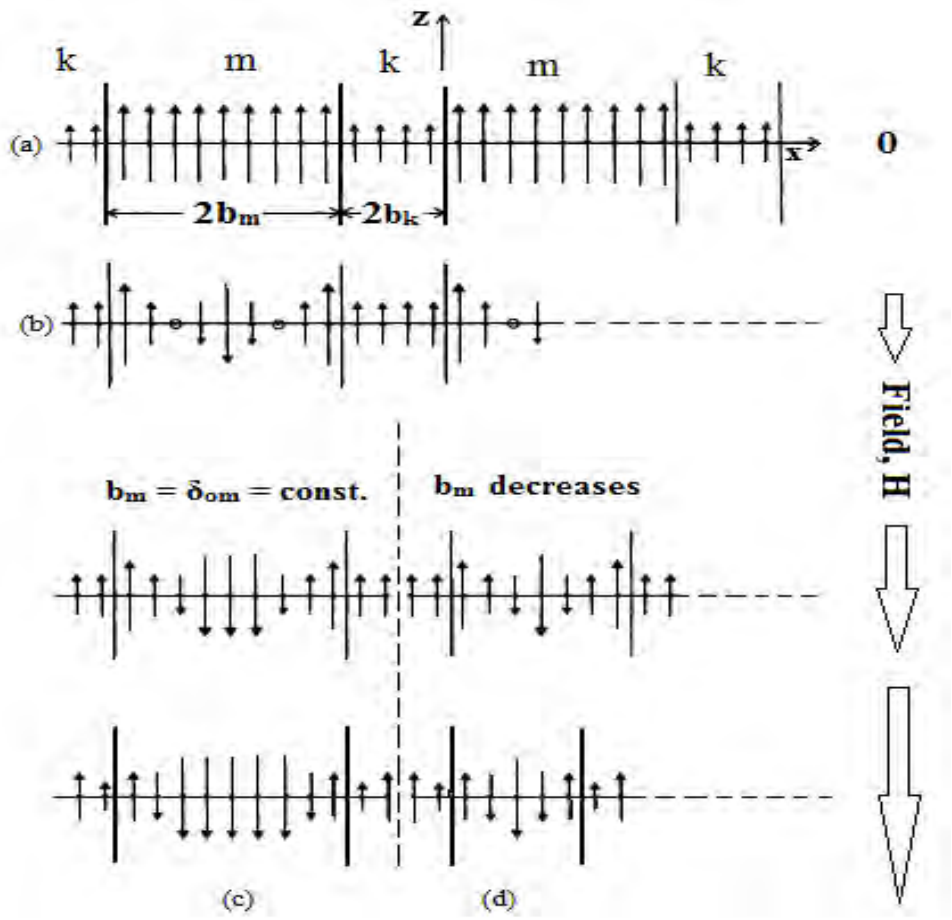

Fig.3.7: Schematic one-dimensional model of the microstructure and micromagnetic structure of the exchange-coupled composite material as a basis for the calculation of the critical of the phase regions.

Let us assume that the hard phase has a reasonable thickness, *e.g.*, $b_k \backsimeq \delta_{ok} = \pi(A_k / K_k)^{½}$ corresponding to about its critical thickness. Starting from the saturation remanence along the easy direction +Z axis Fig.3.7(a) when the reversible field H is increased the magnetization will invariably being to change reversibly in the soft m-phase.

For larger b_m, $b_m \backsimeq \delta_{om} = \pi(A_m/K_m)^{½} \gg \delta_{ok} \backsimeq b_k$ (since $K_m << K_k$), two equilibrium 180° walls will form reversibly in the m-phase Fig.3.7(b). When H is further increased, the energy density in these walls will increase above its equilibrium value $E_{\gamma m} = \gamma_m/\delta_m > E_{\gamma om} = \gamma_{om}/\delta_{om}$ but the magnetization in the k-phase M_{sk} remains essentially unchanged as $K_k >> K_m$. This process will continue until energy density of soft phase $E_{\gamma m}$ approaches the equilibrium energy density of the hard phase $E_{\gamma ok}$.

$$\boldsymbol{E_{\gamma m} = \gamma_m/\delta_m \backsimeq E_{\gamma ok} = \gamma_{ok}/\delta_{ok} = 2K_k} \text{ é é é é .. (7)}$$

At this condition the wall will invade into the k-phase, thus leading to irreversible magnetization reversal of the both m and k phase regions. It should be noted at this point that the corresponding critical field H_{no} is definitely lower than the anisotropy field of the k-phase $H_{no} < H_{AK} = 2K_k/M_{sk}$, yet it will have about the same order of magnitude.

The coercive field H_{cM} is define by $M(H_{cM}) = 0$ and is much smaller, $H_{cM} << H_{no}$ as $M_{sm} > M_{sk}$ and also because it has been assumed that $b_m >> b_k$. Thus the demagnetization curve between M_r (H = 0) and M (H_{cM}) = 0 is completely reversible. If b_m is now reduced to values $b_m < \delta_{cm}$, H_{no} remains unchanged, but H_{cM} increases, because for $H < H_{no}$, the wall thickness of the 180° walls in the m phase is essentially confined to $\delta_m \backsimeq b_m < \delta_{om}$. Hence the critical width of the m phase b_{cm}, giving the maximum coercivity H_{cM}, is determined by the condition (7) with $\delta_m = b_{cm}$. For small $\delta_m(\delta_m << \delta_{om})$, from equation (4) $\gamma_m(\delta_m) \backsimeq \delta_m A_m (\pi/\delta_m)^2$, from where the energy density $E_{\gamma m} = \gamma_m/\delta_m \backsimeq A_m (\pi/\delta_m)^2$. Inserting this result into (7) and setting $\delta_m = b_{cm}$ yields the critical dimension of the *m*-phase:

$$\boldsymbol{b_m \backsimeq \pi (A_m/2K_k)^{½}} \text{ é é é é é é é é é é (8)}$$

With representative values $A_m = 10^{-11}$ J/m, $K_k = 2.10^6$ J/m^3, one gets for b_{cm} the order $b_{cm} \backsimeq$ 5 nm. For the k-phase a critical thickness cannot be derived theoretically. For practical purposes it seems reasonable to take b_{ck} about equal to the equilibrium wall thickness in the k-phase $b_{ck} \backsimeq \delta_{ok} = \pi(A_k/K_k)^{½}$ as has been assumed initially. Since mostly $A_k < A_m$ on account of the generally low curie temperatures of the k-materials, this gives for b_{ck} about the same magnitude as b_{cm}:

$$\boldsymbol{b_{ck} \backsimeq b_{cm}} \text{ é é é é é é é é é é é é é é é é .(8a)}$$

3.12 Volume Fractions of Phases

Under the conditions of about equal lateral dimensions of the two phases $b_{cm} \backsimeq b_{ck}$ {equation 8(a)} and the chemical protection of the k-phase by m-phase, the optimum geometry of the microstructure minimizes the volume fraction of the k-phase; $v_k = V_k/V$ where V_k is the volume of the k-phase and V is the total volume of material. A mathematical solution of this problem would be of no practical value, because in technological realizing such material one must put up with the microstructure that nature produces with a suitable pair of phases.

Thus it may be said that, the type of microstructure to look for is a homogeneous precipitation of k-phase in m-phase and not vice versa. With the reasonable assumptions that precipitates with diameters of the order of some nm are spherical (minimum surface to volume ratio) and are spatially distributed approximately according to an fcc lattice (equal diffusion path) as shown in Fig.3.8 It is obtained with $v_k = \pi/24\tilde{a}2 \backsimeq 0.09$. Virtually the same result is obtained with a bcc lattice: $v_k = \pi\tilde{a}3/64 \backsimeq 0.09$

Once v_k is known, the average saturation magnetization of the material is given by

$$\boldsymbol{M_s} = \boldsymbol{v_k}\,\boldsymbol{M_{sk}} + (1- \boldsymbol{v_k})\boldsymbol{M_{sm}} \text{ é é é é é é é } . (9)$$

Under the initial assumption $M_{sk} < M_{sm}$ and with $v_k = 0.09$, equation (9) yields $M_s \backsimeq M_{sm}$, whereas for platelets of alternating k-phases and m-phases as in model Fig.3.7, $v_k \backsimeq 0.5$ and $M_s = (M_{sk} + M_{sm})/2$.

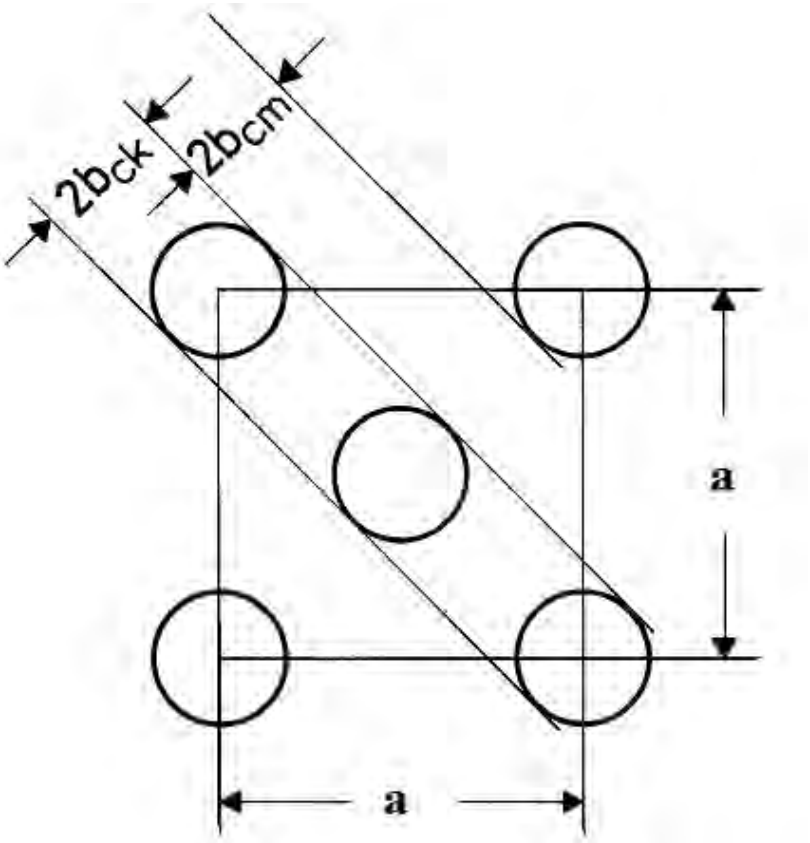

Fig.3.8: Schematic model of a favorable microstructure. The hard magnetic *k*-phase regions are spherical precipitates on an fcc space lattice in soft magnetic *m*-phase. At $b_{ck} = b_{cm}$ the volume fraction of the *k*-phase is $\boldsymbol{v_k} = \boldsymbol{\pi}/24\tilde{a}2 \simeq 0.09$.

Table 3.1 Room temperature values of magnetic properties of some magnetically hard (k - type) and some magnetically soft (m-type) materials

Category	Material	Crystal Symmetry	T_c (°C/K)	M_s (10^6 A/m)	K (10^6 J/ m^3)	$k = \frac{4\pi}{\mu_0 M_s^2}$	H_A (10^6 A/m)	$\mu_0 H_A$(T)	J_s (T)	$\frac{K}{4\pi}$ (10^5 J/m)
k-type hard ($k \gg 1$) $\delta = \frac{\gamma}{\mu_0 M_s}$	$BaO{\cdot}6Fe_2O_3$	hex	450/723	0.38	0.32	7.2	1.35	1.7	0.47	0.45
	MnBi	tetr	360/633	0.58	1.16	9.2	2.94	3.7	0.72	1.3
	$Nd_2Fe_{14}B$	tetr	312/585	1.25	9.4	19	12	15.1	1.57	4.9
	Co_5Sm	hex	730/1003	0.84	11.9	54	23	28.6	1.05	2.2
(k=1) $\frac{\gamma}{\mu_0 M_s}/\frac{\gamma}{\mu_0 M_s}$	Co	hex	1120/1393	1.40	0.53	0.84	0.70/0.60	0.88/0.75	1.76	6.2
k-type soft ($k \ll 1$) $\delta = \frac{\gamma}{\gamma}$	Üï Fe	cub	760/1043	1.70	0.047	0.05	0.85	1.06	2.13	9.0
	$Fe_{23}B_6$	cub	425/698	1.35	0.01	0.03	0.67	0.86	1.70	5.7
	Fe_3B	cub	510/783	1.28	≈ 0.2	0.39	0.64	0.80	1.60	5.1

3.13 Magnetic Behavior

According to the foregoing analysis, the demagnetization curve after previous saturation of such a material will be reversible in reverse fields $H < H_{no}$, i.e., before the magnetization of the k-phase begins to switch, as is illustrated schematically in the Fig.3.9(a) and 3.9(b). On account of exchange coupling between the two phases, the material has unidirectional anisotropy at $H < H_{no}$. For a given pair of the phases, the reversible range in M, ΔM_{rev} depends on the volume fraction of the hard phase v_k or the soft phase $v_m = 1 - v_k$, respectively, on the ratio M_{sm} / M_{sk} and on the lateral dimension of the m-phase b_m. At fixed v_k and M_{sm} / M_{sk}, ΔM_{rev} is smallest for $b_m \backsimeq b_{cm}$ in the optimum microstructure Fig.3.9(a) while the value of M_{sm} / M_{sk} increases as $b_m > b_{cm}$ in the overage state Fig.3.9(b), because H_{no} remain constant. At large v_m, $v_m \backsimeq 0.8$ for example, ΔM_{rev} may well exceed the saturation remanence $\Delta M_{rev} > M_r$ Fig.3.9(b). It is for this specific and quite typical magnetic behavior, in a sense resembling a mechanical spring that such magnets have been termed exchange-spring magnets. There striking reversibility in conjunction with a high remanence and a high coercivity distinguishes them uniquely from the conventional single ferromagnetic phase permanent magnets, where the demagnetization curves reflect essentially the distribution of the critical switching fields and are, therefore, mainly irreversible Fig.3.9(c). In order to further illustrate these features, some minor loops are drawn in the Fig.3.9(a) - (c), as the will be obtained upon reducing to zero and reincreasing the field at various points along the demagnetization curve. The recoil permeability μ_r of an exchange spring magnet is expected to be about 5 times as large as that of a conventional magnet with equal coercive field and saturation magnetization.

As for the general shape of the demagnetization curve $M(H)$, it is immediately obvious from the exchange-spring mechanism that an optimum microstructure ($b_m \backsimeq b_{cm}$) will yield a ñnormalò convex $M(H)$ curve (Fig.3.9(a)) between M_r and $M = 0$, like a conventional permanent magnet (Fig.3.9(c)). Whereas $b_m >> b_{cm}$ an overaged microstructure must lead to a quite characteristic shape of the demagnetization curve being concave throughout from short below the remanence on until saturation in the reverse direction. In any case, the exchange coupling between the phases produces a shape of the saturation loop like that of a uniform material showing no indication of the presence of two phases with extremely different magnetic hardness. If there was no exchange coupling, one would get a constricted loop as in Fig.3.9(d).

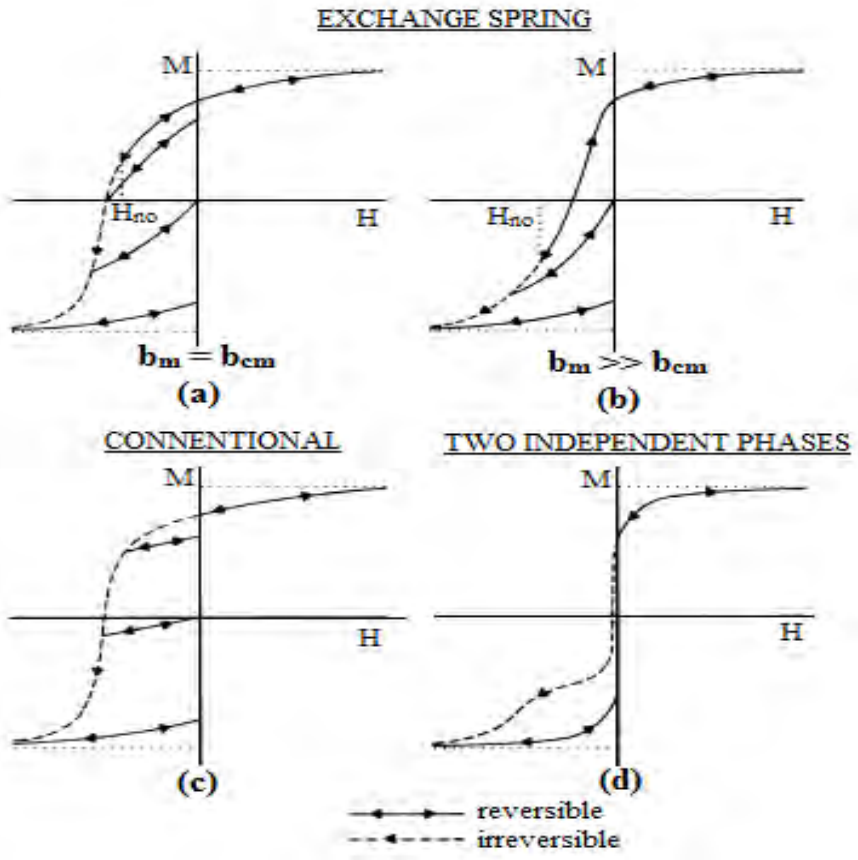

Fig.3.9: Typical demagnetization curves M(H)(schematic). (a) Exchange-spring magnet with optimum microstructure (b) with overaged microstructure (c) Conventional single ferromagnetic phase magnet (d) Mixture of two independent ferromagnetic phases with largely different hardness (constricted loop).

3.14 Saturation Remanence Ratio $m_r = M_r/M_s$

The value of mr depends on the phases employed. A quantitative calculation of m_r for a given pair of phases is in general difficult, because it requires the micromagnetic treatment of complex many body magnetic systems. Kneller and Hawing [1] described here only the character of the problem and on that basis derived approximate solutions for two simple cases in order to illustrate how the parameters of the system determine the result.

It will be generally assumed that the microstructure originates by precipitation of the *k*-phase in an m-matrix and thus corresponds in essence to the model Fig.3.8 and that the number of *k*-precipitates in a single m-grain is large enough to apply statistics where appropriate. Moreover, it is assumed that the *k*-phase has a uniaxial crystal structure, *e.g.,* tetragonal or hexagonal with the c_k-axis being the easy magnetic axis, whereas the *m*-phase may have any symmetry, in particular cubic symmetry.

Since there must be magnetic exchange coupling between the k and *m*-phase regions, the phases must be crystallographically coherent. It implies that the orientations of the c_k-axis (easy axis of the *k*-precipitates) in the m-matrix are not arbitrary, but must be parallel to specific crystallographic axes $[h_ok_ol_o]$ of the *m*-crystal lattice. Since the precipitate will generally from at a temperature above Curie temperatures of both phases, it may be presumed that the c_k-axes of the *k*-precipitates are distributed equally among these distinguished orientations $[h_ok_ol_o]$.

Kneller and Hawig then considered a single spherical (in order to exclude shape anisotropy) m-grain disregarded demagnetization effects. Since $K_k >> K_m$ the resulting saturation remanence of the *k*-precipitates in the grain $\mathbf{I}_{rk}$ then pointed in the direction $[h_sk_sl_s]_\theta$, which was symmetric with respect to the c_k-axes, $[h_ok_ol_o]$ and formed the smallest angle ϑ with the previously applied saturation field $\mathbf{I}$. For simplicity, they assumed for the following that all of these symmetry axes $[h_sk_sl_s]$ with respect to $[h_ok_ol_o]$ were crystallographically equivalent and formed the same angle α_k with all possible c_k-axes $[h_ok_ol_o]$. In such cases the relative magnitude of $\mathbf{I}_{rk}$ became $M_{rk}/M_{sk} = m_{rk} \backsimeq \cos \alpha_k$. The magnetization of the soft m-matrix is exchange coupled with the magnetization of the k-precipitates along their mutual phase boundaries. Therefore the resulting remanence of the m-matrix $\mathbf{I}_{rm}$ will be parallel to $\mathbf{I}_{rk}$. The relative size of $\mathbf{I}_{rm}$, $M_{rm} / M_{sm} = m_{rm}$ will however, be greater than $m_{rk} = \cos \alpha_k$, because the exchange coupling within the m-matrix will smooth out the local magnetization $\mathbf{I}_{sm}$ $(\mathbf{r})$ ($\mathbf{r}$ = position vector) between the nearly fixed (because $K_k >> K_m$) magnetization directions in the surrounding k-precipitates in such a way that the local free energy is

minimized. Thus in the remanent state, the magnetization $\vec{M}_{sm}(\mathbf{r})$ of the m-matrix will be, in general, inhomogeneous, and the resultant m_{rm} must be calculated micromagnetically from the condition of minimum total energy, which may be complicated.

Consequently there exist in such grain of the material j, depending on the crystal symmetry of the m-phase and the crystallographic coherency conditions for the *k*-precipitates, one or several equivalent axes $[h_s k_s l_s]$ for the total resultant saturation remanence vector $\vec{M}_{rj}$, whose relative magnitude

$$\boldsymbol{m_{rj}} = \boldsymbol{M_{rj}}/\boldsymbol{M_s} = (1/\boldsymbol{M_s})[\boldsymbol{v_k m_{rk} M_{sk}} + (1\text{-}\boldsymbol{v_k})\boldsymbol{m_{rm}}\,\boldsymbol{M_{sm}}] \quad (10)$$

is the same for all grain.

For a polycrystalline sample of magnetically independent grains with their crystallographic axes oriented at random, the relative remanence m_r is then obtained by averaging over the angles ϑ between the direction of the previous saturation field H and the corresponding directions $[h_s k_s l_s]$ of $\vec{M}_{rj}$ in the grains:

$$\boldsymbol{m_r} = \boldsymbol{M_r}/\boldsymbol{M_s} = \boldsymbol{m_{rj}}\langle\cos\theta\rangle \quad (11)$$

Any numerical evaluation of (11) requires the knowledge of the crystal symmetry of the m-phase, the crystallographic reorientaions $[h_o k_o l_o]$ of the c_k axes, and volume fractions and saturation magnetizations of the phases. This is illustrated by two simple examples.

Example 1: The m-phase has a uniaxial symmetry (hexagonal or tetragonal), and the ck-axes of the *k*-precipitates form parallel to the c_m-axis of the m-matrix, i.e., $[h_o k_o l_o] = [001]$. In this case, $m_{rk} = m_{rm} = 1$, and from (10) with M_r from (9), $m_{rj} = 1$. Since ϑ may have any value $0 \le \theta \le 90°$ in space, $\langle\cos\theta\rangle = \int_0^{\pi/2} \cos\theta \sin\theta \, d\theta = 0.5$. With this values, (11) yields for a random polycrystalline sample

$$\boldsymbol{m_r} = \boldsymbol{m_{rj}}\langle 0.5\rangle = \boldsymbol{0.5} \quad (11a)$$

independently of the volume fractions and magnetizations of the phase. However, this material may be aligned.

Example 2: The m-phase is cubic, the c_k axes form parallel to the cube edges of the m-matrix, $[h_o k_o l_o] = [100]$, $v_k = 0.1$, and $M_{sm} = 2\,M_{sk}$. In that case, M_{rj} is along $[h_s k_s l_s] = [111]$, i.e. $\alpha_k = 54.5°$ and $m_{rk} = \cos\alpha_k = 0.58$. m_{rm} on the other hand, must be calculated micromagnetically. However, a lower bound of m_{rm} may be obtained by averaging over all space angles Ò $\alpha_k = 54.5°$, giving $m_{rm} \gtrsim 0.79$. With these result, (10) yields with M_r from (9), $m_{rj} \gtrsim 0.78$. since $\vec{M}_{rj}$ will always lie in the [111] direction next to the direction of the previous saturation field $\vec{M}$, $\langle\cos\theta\rangle = 0.87$, and we obtain from (11)

$$\boldsymbol{m_r} \simeq \boldsymbol{m_{rj}}\langle\cos\theta\rangle \gtrsim 0.68 \quad ..(11b)$$

i.e., an isotropic remanence ratio m_r considerably above 0.5, although the angular distribution of the easy axes of the uniaxial magnetically hard phase constituents is by all means isotropic in a polycrystalline sample with random grain orientations. This result is a consequence of the exchange coupling between k and m-phases as well as within the magnetically soft matrix, and also to some extent of the cubic symmetry of the soft phase.

Thus it may be calculated a large isotropic remanence ratio $m_r > 0.5$ is a possible but with regard to example 1, not a universal feature of exchange-spring magnet.

In connecting these two results with the foregoing characteristics of the hysteresis loop, it appears that a largely reversible demagnetization curve in conjunction with an isotropic saturation remanence ratio $m_r \geq 0.5$ may be considered a criterion for the presence of the exchange-spring mechanism.

3.15 Nucleation Field H_{no} and Coercive Field H_{cM}

Of the characteristic properties of an exchange spring magnet, the nucleation field H_{no} for irreversible magnetization reversal and likewise the coercive field $H_{c\mathrm{M}}$ are the most complex and least reliably predictable quantities. Only rough estimates were attempted. With regard to (7) and the way it was derive one would get for a completely aligned microstructure as in Fig.3.7 $H_{no} \backsimeq 2K_k/\mu_o M_{sm}$, and for an isotropic polycrystal about one half of this value

$$\boldsymbol{H_{no} \backsimeq K_k / \mu_o M_{sm}} \quad \text{é é é é é é é é é é é é é é} \quad (12)$$

With representative quantities $K_k = 2.10^6$ J/m^3, $\mu_o M_{sm} = 1.8$T. this would give for H_{no} the order 106 A/m, which seems rather high and may be considered an upper limit to H_{no}.

For an optimum microstructure, $b_m = b_{cm}$, one would expect $H_{cM} \backsimeq H_{no}$. For an overaged microstructure, i.e., $b_m > b_{cm}$, H_{cM} will depend on b_m as

$$\boldsymbol{H_{cM}} \backsimeq \frac{1_1\ 1^1}{1\,1_1\,1\ _{11}} . \frac{1}{1\,1^1_1} \qquad \text{é é é é é é é é é é} \quad (13)$$

For $b_m = b_{cm} = \acute{}\ (A_m/2K_k)^{½}$, (13) transforms into (12), $H_{cM} \backsimeq H_{no}$. With representative values $A_m \backsimeq 10^{-11}$ J/m, $\mu_o M_{sm} = 1.8T$. (13) becomes $H_{cM} \backsimeq 3.\ 10^{-11}/b_m^2$ A/m, giving with, *e.g*, $b_m = 10$ nm, $H_{cM} \backsimeq 3.\ 10^5$ A/m.

With regard to (12), H_{no} and similarly H_{cM} must vary with temperature about as K_k/M_{sm}. In particular, if the Curie temperature of the k-phase is substantially lower than that of the soft m-phase $T_{ck} < T_{cm}$, H_{cM} will decrease rapidly with rising temperature and at T_{ck} will reach the low value of the soft phase.

3.16. Technological Realization

Microstructure

Essential conditions for the microstructure of such material are a fine and regular dispersion of phases on a scale of the order 10 nm ($b_{ck} \backsimeq b_{cm} \backsimeq 5$ nm) and exchange coupling between the k- and m-phase regions, which implies the crystallographically coherent formation of two phases with generally different structures. Such conditions are known to arise during the continuous decomposition of a metastably supersaturated phase that has crystallized from a glassy state. This means that materials with the desired properties may be produced by liquid quenching of a suitable alloy to the glassy state and subsequent heating of the glass. In fact the usefulness of the glassy state as a precursor for producing permanent magnet materials has been widely recognized for over ten years [18,19,22-27] mainly because very finely grained microstructures may be obtained by this method.

Coehoorn *et al.* [19] in his recent publication, reported that liquid quenching and subsequent heating of alloys in the vicinity of $Nd_4Fe_{77}B_{19}$ leads to remarkable permanent magnet properties that possess H_{cM} = 280 kA/m, $(BH)_{max}$ = 95 kJ/m^3) and unusually high isotropic remanence ratio (m_r) greater than 0.5. The material was found to consist of 85% definitely soft magnetic phases (73% Fe_3B and 12% Ŭ-Fe) and only 15% hard phases ($Nd_2Fe_{14}B$). Therefore Kneller and Hawig studied alloys of the similar composition especially $Nd_{3.8}Fe_{77.2}B_{19}$ which they have named alloy (A) and $Nd_{3.8}Fe_{73.3}B_{18}Si_1V_{3.9}$, which they have named alloy (B) and confirmed the study of Coehoorn *et al.* [19]. Kneller, Hawig [1] prepared and studied these alloys in their own laboratories with particular attention to the structural development during heating of the glass, which was observed by a continuous X-ray structural analysis technique using dynamic temperature X-ray diffraction (DTXD).

In the optimum magnetic state of the alloy (A) as obtained by annealing the glass for 10 min at 675°C, the material was found to consist of exactly the phases given in [19] reached the remarkable coercivity $H_{cM} \backsimeq 160$ kA/m. The study of DTXD analysis of the crystallization process of alloy (A) by Kneller and Hawig [1] have revealed that none of the phases present in the optimum magnetic state Ŭ-Fe, Fe_3B and $Nd_2Fe_{14}B$ emerges directly from the glassy state. The glassy state crystallize completely in the matestable $Cr_{23}C_6$-type namely $Fe_{23}B_6$. Very broad and therefore barely detectable reflections seem to result from its supersaturation with the comparatively large Nd atoms. Almost immediately after crystallization, the $Fe_{23}B_6$ phase decomposes first and to the most part into Fe_3B and some

Ŭ-Fe and finally, at a somewhat higher temperature, also $Nd_2Fe_{14}B$. None of these phases dissolves an appreciable amount of Nd. The formation of Fe_3B and Ŭ-Fe phases further increases the supersaturation in Nd of the remaining $Fe_{23}B_6$ phase regions up to a concentration where these transform into $Nd_2Fe_{14}B$. When all of these three phases actually developed from a common crystalline $Fe_{23}B_6$ phase matrix, they are crystallographically coherent. These characteristics thus provided an essential condition for the exchange spring mechanism. Kneller and Hawig studied alloy (A) and alloy (B) and found some interesting results. The primary crystallization from the glass of the phase $Fe_{23}B_6$ is essential, because this phase turned out to be the only one of the phases involved that is capable of dissolving metastably an appreciable amount of the large Nd atoms such that the hard phase $Nd_2Fe_{14}B$ can later precipitate homogenously in that matrix. In addition, $Fe_{23}B_6$ is magnetically soft with a comparatively high magnetization (table 3.1) and has cubic crystal symmetry, thus favoring a high isotropic remanence ratio m_r, as has been explained.

A departure from the ideal exchange-spring behavior is signaled by multiphase magnetic reversal and irreversible magnetic changes that are evident at intermediate magnetic fields. These changes may be monitored via the major demagnetization curve and recoil curves. Analysis of the demagnetization curve yields the exchange-bias field H_{ex} and the irreversible magnetic field H_{irr}. The reorientation of the soft layer is characterized by H_{ex}. For $H < H_{ex}$ the magnetization of the soft layer remains parallel to that of the hard layer and for $H_{irr} > H > H_{ex}$ soft layer moments rotate away from the hard layer alignment direction, lowering the magnetization component along that direction. The irreversible magnetic field H_{irr} describes the reverse field magnitude that causes the hard phase reversal [5]. Reversible and irreversible component of the magnetization change as a function of the reverse field can be determined by analyzing the dc demagnetizing curve *Md(H)* between the saturation remanence M_r and the reverse saturation $-M_s$, which gives the curve *D(H)* ∫ $[M_r - M_d(H)]/2M_r = -æM_{irrev}(H)/2M_r$ versus *H*, the irreversible portion is described by the dc field demagnetization remanence $M_d(H)$ being the remanence acquired after saturation in one direction and subsequent application of a dc field H in the opposition direction. The derivative $dD(H)/dH = f(H_n)$ is the distribution function of critical field H_n for irreversible magnetization reversals [1].

The experimental curve *D(H)* may be interpreted according to the model in Fig.3.7, i.e., by purely inhomogeneously magnetization rotation, assuming equal probabilities of angles $0 \le ı \le 90°$ in the xz plane between the field ıµ and the z axis. In that case, $H_n(\theta) = H_n(0)/$

$cos\theta \equiv H_{no} / cos\theta$. When the reverse field H increases from $H = 0$, no irreversible magnetization reversal occurs as long as $H_1 = H_{no} / cos\theta_1$, for example, all regeoins with $0< ı \leq ı_1$ have reversed and the total irreversible change in magnetization is $-æM_{irrev} = 2M_r ı_1^{ı_1} ııı ı_1 = 2M_r \sin ɗ_1$, from where $D(H_1) = \sin ɗ_1$. The best fit of a corresponding plot of sin ɗ versus $H_{no} / cos\theta$ to the experimental curve $D(H)$ is obtained with the value $H_{no} = 3.0 \times 10^5$ A/m.

The reversible and irreversible components of the magnetization provide further insights as the material is cycled through the hysteresis loop. These components can be obtained from the recoil curve, which results from the successive removal to remanence and reapplication of an increasingly negative demagnetization field from the major demagnetization curve. In exchange spring system, any magnetization not recovered during a recoil measurement- the irreversible magnetization change ï consists of a portion of the system that has already permanently switched polarity at a given reverse field. The steepness of the recoil curve, or the recoil susceptibility, characterizes the ease of remagnetization ñspringinessò of that portion of system undergoing rotation during recoil [5]. Kneller and Hawig [1] note that exchange-spring magnets have recoil susceptibilities five times greater than those found in conventional sintered permanent magnets, it is often noted that recoil curves measured from nanocrystalline magnetic materials are open, indicating the amount of materials reversing during the recoil.

In the general case, fully reversible exchange-spring behavior may persist until application of critical negative field that causes irreversible changes in the magnetic polarization, with larger critical fields associate with a stronger exchange-spring response. These irreversible changes will be manifested as a departure from the ideal recoil remanence ratio of unity and produce recoil loops of varied area. As this critical negative field signals incoherent magnetic reversal in the system, it will be referred to as the ñbreakdownò field [5,12]. As this field the system is no longer fully exchange coupled throughout the volume. Quantitative analysis of the areas enclose by the recoil curves thus provides information about the interactions inherent to exchange-spring system [5]. Harland *et al.* [12] reported that the development of the area of the recoil curve with reverse field and temperature provides information about the breakdown in coherent of the magnetic reversal is signaled by the appearance of open recoil loops. The recoil loops widen as individual decoupled regions of the nanocrystalline materials are driven around mini hysteresis loops during the course of the demagnetization and remagnetization processes.

4.1 Perspective of Experiments

Permanent magnets based on $Nd_2Fe_{14}B$ compounds have been successfully produced mainly by two techniques: liquid-phase sintering and rapid quenching by melt spinning. Anisotropic magnet produced by sintering technique consists of aggregates of relatively large grains or crystallites which have been magnetically aligned prior to sintering. The average grain size is typically between 2 and 10 εm, and the coercivity mechanism is controlled by nucleation of reverse domains at the grain boundaries. The magnets produced by the melt spinning process are composed of ultra-fine crystallites of average diameter typically in the range of 50 to 100 nm, which is smaller than the critical size for single-domain particles for $Nd_2Fe_{14}B$ phase (225 nm at 300K). For a given magnetic material, single-domain particles provide the highest coercivity, and hence, magnet produced by melt spinning route generally show a higher coercivity than those produced by sintering. On the other hand, the magnets produced by melt spinning are crystallographically and magnetically isotropic because of their random grain orientation, resulting in a low remanence that is only half of the saturation magnetization. Hence compared with the anisotropic sintered magnets, the energy products for these types of magnet are significantly smaller [14].

It has been shown that isotropic nanophase Nd-Fe-B processed by melt spinning can be divided into three main groups with respect to Nd content [14].

1) Ribbons of low Nd content (8-11 at percent) have an even greater remanence because of the polarization of the α-Fe phase which has higher spontaneous magnetization than the $Nd_2Fe_{14}B$ phase. A coercivity of 1.4 MA/m at room temperature is easily obtained.
2) Ribbons of stoichiometric or near-stoichiometric Nd (11-13 at percent) alloys show enhanced remanence due to extensive exchange coupling between the ultra-fine $Nd_2Fe_{14}B$ grains a coercivity of about 0.8 MA/m is achievable. It is worth nothing that single phase $Nd_2Fe_{14}B$ alloys with a large grain size shows no coercivity.
3) Ribbons of high Nd content (>13 at percent) have a very high coercivity due to well-isolated single domain particles.

4.2 Melt spin system:

Amorphous alloys in the form of ribbons have been prepared by single roller melt-spinning technique in air. Melt spin system presented in Fig.5.1 is a small laboratory system, especially designed for production of amorphous and microcrystalline ribbons. Melting of material is performed by a high frequency generator with water-cooled induction coil. Molten material flows through a slot on a fast rotating copper wheel. The melt is quenched with a cooling rate of more than 10^6 K/s, which solidifies in an amorphous structure.

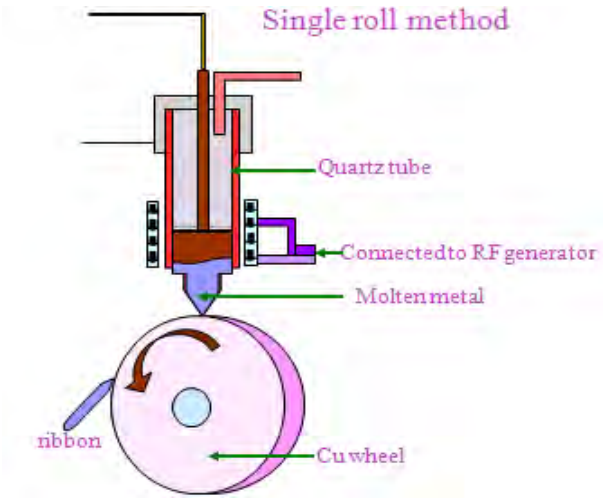

Fig.4.1: Schematic diagram of melt spin system

4.3 Preparation of Fe-based hard magnetic ribbon by melt spin system

Exchange spring alloys of composition of $Nd_4Fe_{76}Cu_{0.5}Nb_1B_{18.5}$ were prepared in the form of ribbons using melt-spin machine. The purity and origin of constituent elements were Fe(99.98%), Cu(99+%), Nb(99.8%), B(99.5%), Nd(99.9%) from Johnson Matthey (Alfa Aesar). Constituent elements in the correct proportions were mixed and melted in the arc-melting furnace under vacuum of 10^{-6} mbar pressure. In order to homogenize perfectly, the alloys were melted three times. The ingots were then poured into a quartz tube having an orifice diameter of 1 mm. quartz tube was placed inside an induction coil associated with machine. A steel casing covers whole assembly of single roller melt-spin machine. In the beginning the chamber inside the casing was flashed by Ar gas three times. The chamber was then filled with Ar gas. The alloy ingots were then melted by induction melting. Appropriate temperature of the melt was assumed from the color by eye estimation. When the color of the melt was appropriate amorphous ribbons were obtained in Ar atmosphere by purging the melt using Ar pressure. Wheel speed of single roller melt spin machine was

around 25 m/s. The resulting ribbons were heat treated in an evacuated quartz tube of 10^{-5} mbar pressure at different temperatures and times to observe the effect of annealing condition on the magnetic properties.

4.4 Thermal Analysis Techniques

Thermal analysis comprises of a group if techniques in which a physical property of a substance is measured as a function of temperature, while the substance is subjected to a controlled temperature program. In differential thermal analysis, the temperature difference that develops between a sample and an inert reference material is measured. When both are subjected to identical heat treatments. The related technique of differential scanning calorimetry relies on differences in energy required to maintain the sample and reference at an identical temperature.

4.5 Differential scanning calorimetry (DSC)

Differential scanning calorimetry (DSC) is a thermo analytical technique for measuring the energy necessary to establish a nearly zero temperature difference between a substance and an inert reference material, as the two specimens are subjected to identical temperature regimes in an environment heated or cooled at a controlled rate.

Principle of Operation

The basic principle underlying this technique is that, when the sample undergoes a physical transformation such as phase transition, more (or less) heat will need to flow to it than the reference to maintain both at the same temperature. Whether more or less heat must flow to the sample depends on whether the process is exothermic or endothermic. In powerï compensation DSC the temperatures of the sample and reference are controlled independently using separate, identical furnaces. The temperatures of the sample and reference are made identical by varying the power input to the two furnaces; the energy required to do this is a measure of the enthalpy or heat capacity changes in the sample relative to the reference.

In heatï flux DSC, the sample and reference are connected by a lowï resistance heatï flow path (a metal disc). The assembly is enclosed in a single furnace. Enthalpy or heat capacity changes in the sample cause a difference in its temperature relative to the reference; the resulting heat flow is small compared with that in differential thermal analysis (DTA)

because the sample and reference are in good thermal contact. The temperature deference is recorded and related to enthalpy change in the sample using calibration experiments.

DSC Instrumentation

A typical differential scanning calorimeter consists of two sealed pans: a sample pan and a reference pan (which is generally an empty sample pan). These pans are often covered by or composed of aluminum, which acts as a radiation shield. The two pans are heated, or cooled, uniformly while the heat flow difference between the two monitored. This can be done at a constant rate, a mode of operation also called temperature scanning.

During the determination, the instrument detects differences in the heat flow between the sample and the reference. This information is sent to an output device, most often a computer, resulting in a plot of the differential heat flow between the reference and the sample cell as a function of temperature. When there is no thermodynamic physical or chemical process occurring, the heat flow difference between the sample and the reference varies only slightly with temperature, and shows up as a flat or very shallow base line on the plot. However, an exothermic or endothermic process within the sample results in a significant deviation in the difference between the two heat flows. The result is a peak in the DSC curve. Generally, the differential heat flow is calculated by subtracting the sample heat flow from the reference heat flow. When following this convention, exothermic process will show up as a positive peak (above the baseline) while peaks resulting from endothermic process are negative (below the baseline). The sample (in a condensed form such as powder, liquid, or crystal) is generally placed in an aluminum sample pan, which is then placed in the sample cell. The reference consists of a matched empty aluminum sample pan that is placed in the reference cell of the instrument. The sample pans are designed to have a very high thermal conductivity. Sample sizes generally range from 0.1 to 100 mg. The instrument cells are often airtight to shield the sample and the reference from the external thermal perturbations. This also allows experiments to be performed under variable pressure and atmospheres.

There are two main types of differential scanning calorimeters:

a. Heat flux DSC b. Power compensation DSC.

Heat flux DSC

In a heat flux calorimeter, shown in Fig.5.2, heat is transferred to the sample and reference through a disk made of the alloy constantan or in some cases, silver. The heat transported to the sample and the reference is controlled while the instrument monitors the temperature difference between the two. In addition to its function in the heat transfer, this disk serves as part of the temperature-sensing unit. The sample and reference reside on raised platforms on the disk. Under each of these platforms there is a chromel (chromel is an alloy containing chromium, nickel and sometimes iron) wafer. The junction between these two alloys forms a chromel-constant thermocouple. The signal from these sensors is then used to measure the differential heat flow. The temperature is typically monitored by chromel-alumel thermocouples attached beneath the chromel wafers.

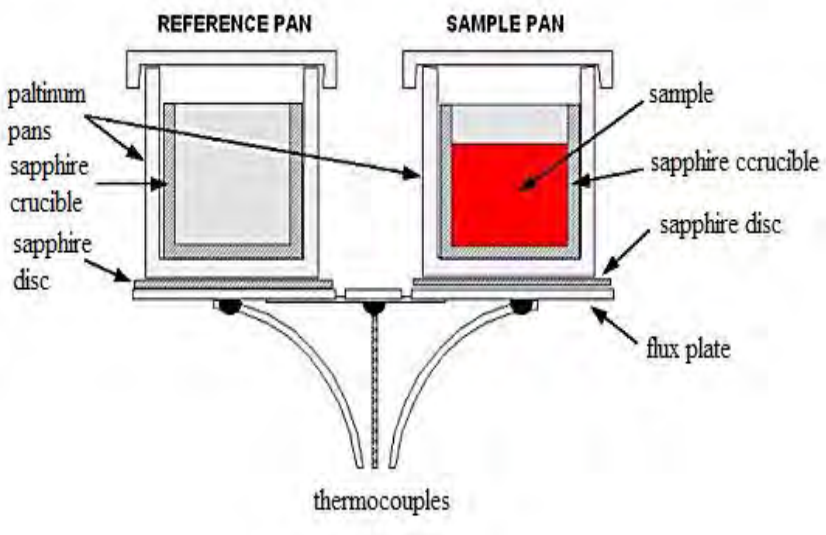

Fig.4.2: Diagram of a heat flux differential scanning calorimeter

Power Compensated DSC

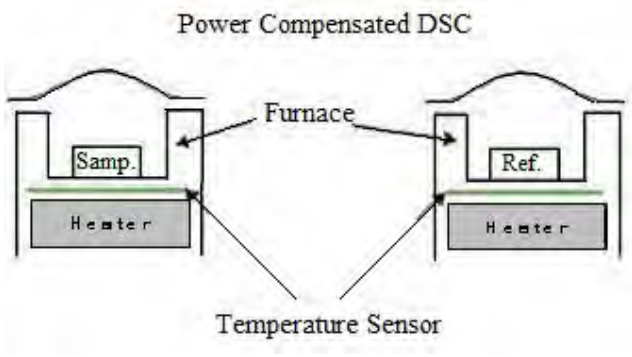

Fig.4.3: Diagram of a Power compensated differential scanning calorimeter.

In power compensated calorimeters, shown in Fig.5.3, separate heaters are used for the sample and reference. Both the sample and reference are maintained at the same temperature while monitoring the electrical power used by their heaters. The heating elements are kept very small (weighing about 1 gram) in order to ensure that heating, cooling, and thermal equilibration can occur as quickly as possible. The sample and the reference are located above their respective heaters and temperatures are monitored using electric temperature sensors located just beneath the samples. Generally platinum resistance thermometers are used due to the high melting point of platinum.

Electronically, the instruments consist of two temperature control circuits. An average temperature control circuit is used to monitor the progress of the temperature control program. This circuit is designed to assure that the temperature scanning program set by the operator is the average temperature of the sample and reference. A differential temperature control circuit is used to determine the relative temperatures of the sample and the reference, and adjust the power going to the respective heaters in such a way as to maintain both at the same temperature. The output of the differential temperature control circuit is used to generate the DSC curve.

DSC Curves

The result of a DSC experiments is a heating or cooling curve as shown in Fig.5.4. This curve can be used to calculate enthalpies of transitions. This is done by integrating the peak corresponding to a given transition. It can be shown that the enthalpy of transition can be expressed using the following equation, $\Delta H=KA$, where ΔH is the enthalpy of transition, K is the calorimetric constant, and A is the area under the curve. The calorimetric constant will vary to instrument, and can be determined by analyzing a well-characterized sample with known enthalpies of transition.

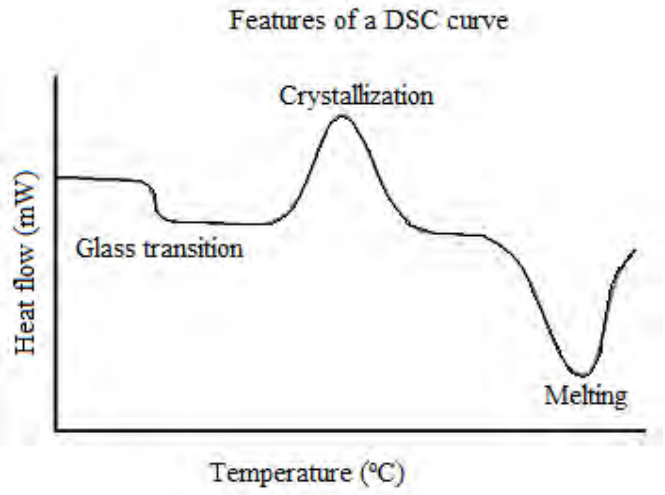

Fig.4.4: A schematic DSC curve demonstrating the appearance of several common features

Applications

DSC is commonly used to measure a variety of properties in both organic and inorganic materials, from metals and simple compounds to polymers and pharmaceuticals. The properties measured include:

- Glass transitions
- Phase changes
- Melting
- Crystallization
- Product stability
- Cure / cure kinetics

- Oxidative stability
- Heat capacity and heat of fusion measurements

4.6 Examples

The technique is widely used across a range of applications, both as routine quality test and a research tool. The equipment is easy to calibrate, using low melting indium for example, and is a rapid and reliable method of thermal analysis.

Liquid crystals

DSC may also be used in the study of liquid crystal. As matter transitions between solid and liquid it often goes through a third state, which displays properties of both phases. This anisotropic liquid is known as liquid crystalline or mesomorphous state. Using DSC, it is possible to observe the small changes that occur as matter transitions from a solid to liquid crystal and from a liquid crystal to an isotropic liquid.

Oxidative stability

Using the differential scanning calorimetry to study the oxidative stability of samples generally requires an airtight sample chamber. Usually, such tests are done isothermally (at constant temperature) by changing the atmosphere of the sample. First, the sample is brought to the desire test temperature under an inert atmosphere, usually nitrogen. Then oxygen is added to the system. Any oxidation that occurs is observed as a deviation in the baseline. Such analysis can be used to determine the stability and optimum storage conditions for a compound.

Drug Analysis

DSC is widely used in the pharmaceuticals and polymer industries. For the polymer chemist, DSC is a handy tool for studying curing processes, which allows the fine tuning of polymer properties. The cross-linking of polymer molecules that occurs in the curing process is exothermic, resulting in a positive peak in the DSC curve that usually appears soon after the glass transition.

In the pharmaceutical industry it is necessary to have well-characterized drug compounds in order to define processing parameters. For instance, if it is necessary to deliver a drug in the amorphous form, it is desirable to process the drug at temperature below those at which crystallization can occur.

Food science

In food science research, DSC is used in conjunction with other thermal analytical techniques to determine water dynamics. Changes in water distribution may be correlated with changes in texture. Similar to material science studies, the effects of curing on confectionery products can also be analyzed.

General chemical analysis

Freezing-point depression (it is what allows salt to de-ice sidewalks and antifreeze to keep vehicles running in the winter) can also be used as a purity analysis tool when analyzed by differential scanning calorimetry. This is possible because the temperature range over which a mixture of compound melts is dependent on their relative amounts. Consequently, less pure compound will exhibits a broadened melting peak that begins at lower temperature than a pure compound.

SDT 2960 Simultaneous DSC-TGA measures heat flow to or from a sample as a function of temperature and time. The heat flow and temperature of the sample are monitored in comparison on the reference material. The amount of energy absorbed (endotherm) or evolved (exotherm) as the sample undergoes physical or chemical changes (e.g. melting, crystallization, curing) is measured in calories as a function of temperature change. Any material reactions involving changes in heat capacity (e.g. glass transition) are also detected. DSC can be performed from ambient to 1773K using this model of DSC instrument.

4.7 Annealing

Annealing, in metallurgy and materials science, is a heat treatment wherein a material is altered, causing changes in its properties such as strength and hardness. It is a process that produces conditions by heating to above the critical temperature, maintaining a suitable temperature, and then cooling. Annealing is used to induce ductility, soften material, relieve internal stresses, refine the structure by making it homogeneous, and improve cold working properties.

In the cases of copper, steel, silver, and brass, this process is performed by substantially heating the material (generally until glowing) for a while and allowing it to cool. Unlike ferrous metalsð which must be cooled slowly to annealð copper, silver and brass can be cooled slowly in air or quickly by quenching in water. In this fashion the metal is softened and prepared for further work such as shaping, stamping, or forming.

Annealing occurs by the diffusion of atoms within a solid material, so that the material progresses towards its equilibrium state. Heat is needed to increase the rate of diffusion by providing the energy needed to break bonds. The movement of atoms has the effect of redistributing and destroying the dislocations in metals and (to a lesser extent) in ceramics. This alteration in dislocations allows metals to deform more easily, so increases their ductility.

Stages

There are three stages in the annealing process, with the first being the recovery phase, which results in softening of the metal through removal of crystal defects (the primary type of which is the linear defect called a dislocation) and the internal stresses which they cause. Recovery phase covers all annealing phenomena that occur before the appearance of new strain-free grains. The second phase is recrystallization, where new strain-free grains nucleate and grow to replace those deformed by internal stresses. If annealing is allowed to continue once recrystallization has been completed, grain growth will occur, in which the microstructure starts to coarsen and may cause the metal to have less than satisfactory mechanical properties.

Setup and equipment

Typically, large ovens are used for the annealing process. The inside of the oven is large enough to place the workpiece in a position to receive maximum exposure to the circulating heated air. For high volume process annealing, gas fired conveyor furnaces are often used. For large workpieces or high quantity parts Car-bottom furnaces will be used in order to move the parts in and out with ease. Once the annealing process has been successfully completed, the workpieces are sometimes left in the oven in order for the parts to have a controlled cooling process. While some workpieces are left in the oven to cool in a controlled fashion, other materials and alloys are removed from the oven. After being removed from the oven, the workpieces are often quickly cooled off in a process known as quench hardening. Some typical methods of quench hardening materials involve the use of media such as air, water, oil, or salt. Quench hardening is generally applicable to some ferrous alloys, but not copper alloys.

4.8 Powder / polycrystalline diffraction

About 90 % of all solid materials can be described as crystalline. When X-ray interact with a crystalline substance (Phase), one gets a diffraction pattern. The X-ray diffraction pattern of a pure substance is, therefore, like a fingerprint of the substance. The powder diffraction method is thus ideally suited for characterization and identification of polycrystalline phases. Today about 50000 inorganic and 25000 organic single components, crystalline phase and diffraction patterns have been collected and stored on magnetic or optical media as standers. The main use of powder diffraction is to identify components in a sample by a search/match procedure. Furthermore, the areas under the peak are related to the amount of each phase present in the sample.

4.8.1 Theoretical Considerations

In order to better convey an understanding of the fundamental principles of X-ray diffraction instruments, let us quickly look at the theory behind these systems. An electron in an alternating electromagnetic field will oscillate with the same frequency as the field. When an X-ray beam hits an atom, the electrons around the atom starts to oscillate with the same frequency as the incoming beam. In almost all directions we will have destructive interference, that is, the combining waves are out of phase and there is no resultant energy leaving the solid sample. However, the atoms in a crystal are arranged in a regular pattern, and in a very few directions we will have constructive interference. The waves will be in phase and there will be well-defined X-ray beams leaving the sample at various directions. Hence, a diffracted beam may be described as a beam composed of a large number of scattered rays mutually reinforcing one another.

The orientation and interplanar spacing of these planes are defined by the three integers h, k, l called indices. A given sets of planes with indices h, k, l cut the a-axis of the unit cell in h sections, the b axis in k sections and the c axis in 1 sections. A zero indicates that the planes are parallel to the corresponding axis. For example the 2 2 0 planes, in Fig.5.5, cut the a- and the b- axes in half, but are parallel to the c-axis.

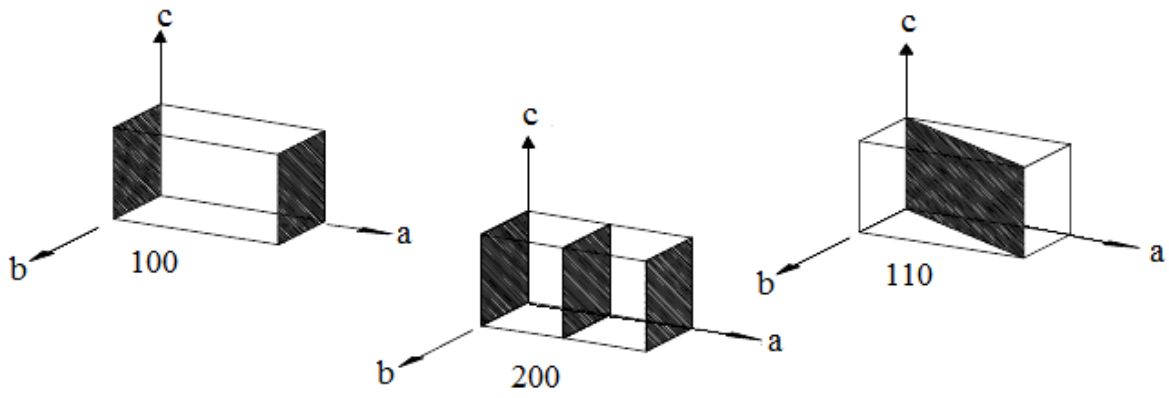

Fig.4.5: Orientations of the planes are defined by the miller indices.

If we use the three dimensional diffraction grating as a mathematical model, the three indices h, k, l become the order of diffraction along the unit cell axes a, b and c respectively. Let us consider the theoretical model depending on what we use the terms X-ray reflection and X-ray diffraction as synonyms.

When a crystal is bombarded with X-rays of a fixed wavelength (similar to spacing of the atomic-scale crystal lattice planes) and at certain incident angles, intense reflected X-rays are produced when the wavelengths of the scattered X-rays interfere constructively. In order for the waves to interfere constructively, the differences in the travel path must be equal to integer multiples of the wavelength. When this constructive interference occurs, a diffracted beam of X-rays will leave the crystal at an angle equal to that of the incident beam.

To illustrate this feature, consider a crystal with crystal lattice planar distances d (right). Where the travel path length difference between the ray paths ABC and A'B'C' is an integer multiple of the wavelength, constructive interference will occur for a combination of that specific wavelength, crystal lattice planar spacing and angle of incidence (Ū). Each rational plane of atoms in a crystal will undergo refraction at a single, unique angle (for X-rays of a fixed wavelength).

The general relationship between the wavelength of the incident X-rays, angle of incidence and spacing between the crystal lattice planes of atoms is known as Bragg's Law, expressed as:

$$n \lambda = 2d \sin\bar{U}$$

where n (an integer) is the "order" of reflection, λ is the wavelength of the incident X-rays, d is the interplanar spacing of the crystal and Ū is the angle of incidence.

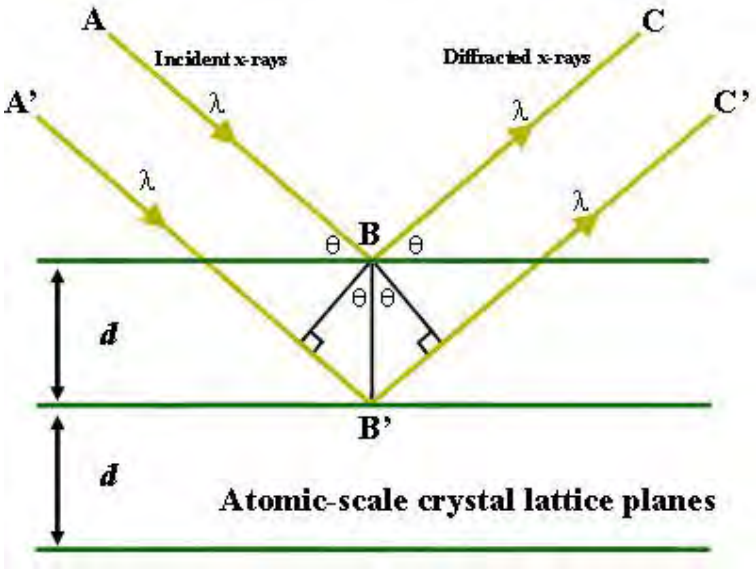

Fig.4.6: Bragg reflection of two parallel incident rays A and Aô

Therefore the two possible values where we can have reflections are determined by the unit cell dimensions. However, the intensities of the reflection are determined by the distribution of the electrons in the unit cell. The highest electron density is found around atoms. Therefore, the intensities depend on what kind of atoms we have and where in the unit cell they are located. Planes going through areas with high electron density will reflect strongly, planes with low electron density will give weak intensities.

Diffraction Slit System

The diffractometer slit system has been presented in Fig 4.9. The focal spot for a standard focus X-ray tube is about 10 mm long and 1 mm wide, with a power capability of 2000 watt, which equals to a power loading of 200 watt/mm^2. Power ratings are dependent on the thermal conductivity of the target material. The maximum power loading of an Cu X-ray tube is 463 watt/mm^2. This power is achieved by a long fine focus of the tube with a target size of 12 mm long and 0.4 mm wide. In powder diffraction the line focus or line source of the tube is normally utilized the line source emits radiation in all directions, but in order to enhance the focusing it is necessary to limit the divergence in the direction along the line focus. This is realized by passing the incident beam through a solar slit, which contains a set of closely space thin metal plates. In order to maintain a constant focusing distance it is necessary to keep the sample at an angle THETA (Omega) and the detector at an angle of 2-THETA with respect to the incident beam. For an THETA: THETA goniometer the tube has to be at an angle of THETA (Omega) and the detector at an angle of THETA with respect to the sample.

Diffraction Spectra

A typical diffraction spectrum consists of a plot of reflected intensities versus the detector angle 2ɗ or ɗ depending on the goniometer configuration. The 2ɗ values for the peak depend on the wavelength of the anode material of the X-ray tube. It is therefore customary to reduce a peak position to the interplanar spacing d that corresponds to the h, k, l planes that caused the reflection. The values of the d-spacing depend only on the shape of the unit cell. We get the d-spacing as a function of 2ɗ from Braggôs law, d = ɔ/2 sin ɗ. Each reflection is fully defined when we know the d-spacing, the intensity (area under the peak) and the indices h, k, l. if we know the d-spacing and the corresponding indices h, k, l we can calculate the dimension of the unit cell.

ICDD Data Base

International Center diffraction data (ICDD) or formerly known as (JCPDS) Joint Committee on Powder Diffraction Standard is the organization that maintain the data base of inorganic and organic spectraôs. The data base is available from the diffraction equipment manufacturers or from ICDD direct. Currently the data base is supplied either on magnetic or optical media. Two data base versions are available the PDF I and the PDF II.

The PDF I data base contains information on d-spacing, chemical formula, relative intensity, RIR quality information and routing digit. The information is stored in an ASC II format in a file called PDF I data. For search/match purposes most diffraction manufactures are reformatting the file in a more efficient binary format.

The PDF II data base contains full information a particular phase including cell parameters. Scintagôs newest search/match and look-up software package is using the PDF II format. Optimized data base format, index files and high performance PC-computers make PDF II search times extremely efficient. The data base format consists of a set number and a sequence number. The set number is incremented every calendar year and the sequence number starts from 1 for every year. The yearly releases of the data base are available in September of each year.

4.8.2 Applications

Identification of phases: the most common use of powder (polycrystalline) diffraction is chemical analysis. This can include phase identification (search/match), investigation of high/low temperature phase, solid solutions and determination of unit cell parameters of new materials.

Polymer Crystallinity:

A polymer can be considered partly crystalline and partly amorphous. The crystalline domains act as a reinforcing grid, like the iron framework in concrete, and improve the performance over a wide range of temperature. However, too much crystallinity causes brittleness. The crystallinity parts give sharp narrow diffraction peaks and the amorphous component gives a very broad peak (halo). The ratio between these intensities can be used to calculate the amount of crystallinity in the material.

Residual Stress:

Residual stress is the stress that remains in the material after the external force that caused the stress have been removed. Stress is defined as force per unit area. Positive values indicate tensile (expansion) stress, negative values indicate a compressive stress. The deformation per unit length is called strain. The residual stress can be introduced by any mechanical, chemical or thermal process, e.g. machining, plating and welding.

The principle of the stress analysis by the X-ray diffraction is based on measuring angular lattice strain distributions. That is, we chose a reflection at high 2-Theta and measure the change in the d-spacing with deferent orientations of the sample. Using Hookôs law the stress can be calculated from the strain distribution.

Texture Analysis: The determination of the preferred orientation of the crystallines in polycrystalline arrogates is referred to as texture analysis, and the term texture is used as a broad synonym for preferred crystallographic orientation in the polycrystalline material, normally a single phase.

Grain Size Determination: When the size of the individual crystals is less than about 1000 A, grain size can be determined from line broadening, B = 0.9ə/t cosƈ where B = broadening of diffraction line measured at half its maximum intensity (radians) and t = diameter of crystal particle. All diffraction lines have a measurable breadth, even when the crystal size exceeds 1000 A, due to such causes as divergence of the incident beam and size of the sample (in Debye cameras) and width of the X-ray source (in diffractometers). The breadth B refers however, to the extra breadth, or broadening, due to the particle-size effect alone. In other words, B is essentially zero when particle-size effect alone. In other words, B is essentially zero when particle-size about 1000A.

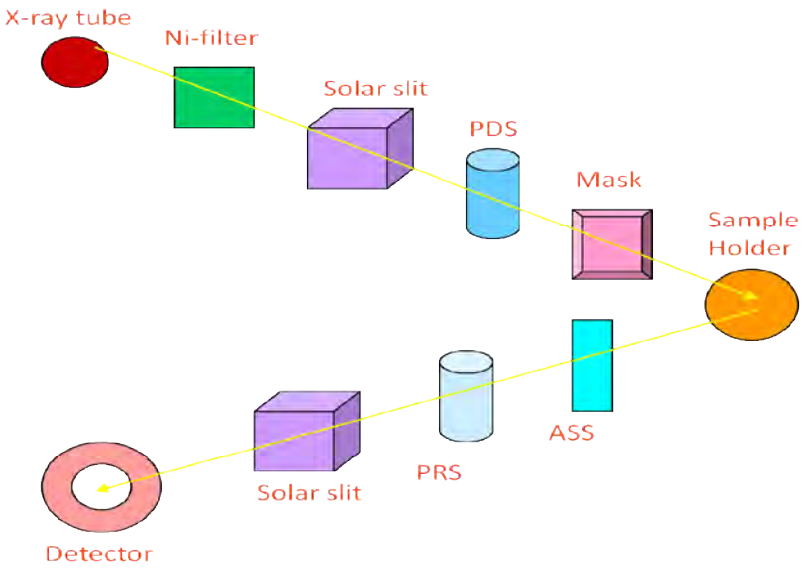

Fig.4.7: Diffractometer Slit System

4.8.3 Philips X'Pert Pro Multipurpose X-ray Diffractometer

The XôPert PRO diffraction system utilizes a modular system approach to provide performance for applications ranging from routine characterization to in-depth research investigations. The PreFIX (Pre-aligned Fast Interchangeable X-ray Optics) concept enables the diffraction system to be reconfigured in a few minutes without the need for re-alignment to handle different types of analysis. A suite of data analysis software from Philips is available. During X-ray diffraction analysis, X-ray beams are reflected off a specific wavelength, for any given d-spacing (distance between adjacent atomic planes) there are only specific angles at which the exiting rays will be óin phaseô and therefore, will be picked up by the detector producing a peak on the ódiffractogramô. Just like a ófingerprintô, every mineral has its own distinct set of diffraction peak that can be used to identify it.

The system enables us to do the analysis on phase identification and quantification, as well as crystal structure studies. The specifications of the system are:

- X-RAY SOURCES: 3 kW Copper tube
- OPTICS: focusing and parallel PreFix optics, programmable slits, tunable diffracted beam monochromator.
- DETECTORS: Xe proportional counter and solid state Xôcellerator
- SAMPLES STAGES: Single sample holder, 15-sample changer

- VARIABLE TEMPERATURE CAPABILITY: Anton-Parr 77 ï 725 K and 300 ï 1475 K cameras
- SOFTWARE AND DATABASES: Data collector, X'Pert Plus crystallographic analysis software with Rietveld capability, ProFit line profile analysis software.
- INSTRUMENT STATISTICS: The system uses Cu K_α radiation that has a wavelength of 1.54 A. Analysis are commonly run using a 40 kV 45mA x-ray tube voltage, a 0.04° soller slit, 1° divergence and antiscatter slits, and a 1/2° (for powder) or 1/4° (for clays) receiving slit.

4.9 Vibrating sample magnetometer (VSM)

The vibrating sample magnetometer has become a widely used instrument for determining magnetic properties of a large variety of materials: diamagnetics, paramagnetics, ferromagnetics, ferromagnetics and antiferromagnetics. This experimental technique was invented in 1956 by Simon Foner, a scientist of the MIT. It has a flexible design and combines high sensitivity with easy of sample mounting and exchange. Samples may be interchange rapidly even at any operating temperature. Measurements of magnetic moments as small as $5x10^{-5}$ emu are possible in magnetic fields from zero to 9 Tesla (or higher). Maximum applied fields of 2-3 Tesla or 9 Tesla are reached using conventional laboratory electromagnets and superconducting solenoids, respectively. Vibrating sample magnetometers normally operate over a temperature range of 2.0 to 1050K. Powders, bulk and thin films can be measured and studied.

4.9.1 Principle

A vibrating sample magnetometer (VSM) operates on Faraday's Law of Induction, which tells us that a changing magnetic field will produce an electric field. This electric field can be measured and can tell us information about the changing magnetic field. A VSM is used to measure the magnetic behavior of magnetic materials.

A VSM operates by first placing the sample to be studied in a constant magnetic field. If the sample is magnetic, this constant magnetic field will magnetize the sample by aligning the magnetic domains, or the individual magnetic spins, with the field. The stronger the constant field, the larger the magnetization will be. The magnetic dipole moment of the sample will create a magnetic field around the sample, sometimes called the magnetic stray field. As the sample is moved up and down, this magnetic stray field is changing as a function of time and can be sensed by a set of pick-up coils. The alternating magnetic field will cause an electric field in the pick-up coils according to Faraday's Law of Induction.

This current will be proportional to the magnetization of the sample. The greater the magnetization, the greater the induced current. The induction current is amplified by a transimpedance amplifier and lock-in amplifier. The various components are hooked up to a computer interface. Using controlling and monitoring software, the system can tell you how much the sample is magnetized and how its magnetization depends on the strength of the constant magnetic field. A typical measurement of a sample is taken in the following manner:

- the strength of the constant magnetic field is set.
- the sample begins to vibrate
- the signal received from the probe is translated into a value for the magnetic moment of the sample
- the strength of the constant magnetic field changes to a new value. no data is taken during this transition
- the strength of the constant magnetic field reaches its new value
- the signal from the probe again gets translated into a value for the magnetization of the sample
- the constant magnetic field varies over a given range, and a plot of magnetization (M) versus magnetic field strength (H) is generated.

Parts of the VSM

The VSM consists of ten parts:

1. water cooled electromagnet and power supply:

   The water cooled electromagnet, along with the power supply, generates the constant magnetic field used to magnetize the sample.

2. vibration exciter and sample holder (with angle indicator):

   The sample holder rod is attached to the vibration exciter, and the end of it hangs down in between the pole pieces. The exciter moves the sample up and down at a set frequency, typically 85Hz. The sample rod can be rotated to achieve the desired orientation of the sample to the constant magnetic field. There are also three knobs for controlling the x,y, and z positions of the sample.

3. sensor coils:

   The sample produces an alternating current in these coils at the same frequency as the vibration of the sample. The signal generated contains the information about the magnetization of the sample.
4. Hall probe
5. Amplifier:

   The amplifier does just that - amplifies the signal created by the sensor coils.
6. control chassis:

   This controls the 85Hz oscillation of the exciter.
7. lock in amplifier:

   This amplifier is tuned to pick up only signals at the vibrating frequency. This eliminates noise from the environment, such as from the overhead lights or hovering spacecraft nearby (unless the noise happens to be an 85Hz signal).
8. Meter:

   This is used to measure something important.
9. computer interface:

   The software makes data collection easier by automating the control of the various components during data collection. The data can be graphed and plotted on the printer.

4.9.2 Applications

Using a vibrating sample magnetometer one can measure the DC magnetic moment as a function of temperature, magnetic field, angle and time. So, it allows to perform susceptibility and magnetization studies. Some of the most common measurements done are: hysteresis loops, susceptibility or saturation magnetization as a function of temperature (thermomagnetic analysis), magnetization curves as a function as a function of angle (anisotropy), and magnetization as a function of time.

Fig.4.8: EV9 Vibrating Sample Magnetometer

4.9.3 Benefits of Using the EV9 VSM

- Noise below 0.5 µemu when used with the EV1-LNA temperature option
- Noise below 0.1 µemu at a usable sample space
- Field noise <5mOe with optional 1x probe or 15 mOe with standard 10x probe
- Highest magnetic field of >2.15T with temperature chamber and/or vector coils in place of any similarly sized system
- No hardware change between cooling and heating from 77K to 1000K or 1050K
- New helium temperature option 4.2K to 450K
- Temperature option always ready to use installed on magnet base.
- Safe and reliable air-cooled magnet power supply
- System can be used without water cooling for low field or medium duty cycle measurements
- 3 systems in one with optional Torque Magnetometer and Magneto Resistance options
- Small footprint: 1 cabinet + measurement station

High Accuracy

The high precision real time, direct field control used in conjunction with high performance signal acquisition and processing, leads to increased accuracy of the measured graphs and measured parameters, while at the same time facilitating measurements on soft magnetic

samples with field resolution of 1 mOe. The EV9 VSM system offers a dynamic field resolution whereby the field resolution switches, during the measurement, to the best available for the given field range. This is critical when measuring low coercivity materials after setting a higher initial field to saturate.

Flexible Options: Three Systems in One

All EV VSMs offer a unique combination system including torque, and/or magneto-resistance (MR) options, which can be added to the VSM without increasing the system footprint and are less expensive than buying separate systems.

The torque option measures the torque of materials as a function of rotation angle and applied field, resulting in Anisotropy data. The MR measures the resistance of thin film samples as a function of magnetic field, temperature, and angle. Measurements (with > 5000 points) take less than two minutes.

Fast and Easy To Use

A unique sample vibrating mechanism makes sample mounting and alignment fast and convenient. Samples can quickly and easily be aligned properly to maximize the measurement accuracy and repeatability. Thanks to the direct field control and high sensitivity the EV9 is typically 3 times faster than competing systems. The temperature options (Helium temperature chamber shown here) always remain installed on the system and can be moved in and out of place using a simple lever-slide mechanism. This allows very fast changes between room temperature and low or high temperature measurements.

Great Low and High Field Capabilities

The EV9 VSM is unique in its combination of a very high maximum field for a compact system combined with unrivaled low field measurement performance. The EV9 also offers the highest signal to noise ratio under most normal measurement circumstances.

Due to a proprietary real-time field control system, this system is suited for measuring samples with extremely low magnetic signals and/or very low coercivities. The EV9 is the most compact electromagnet based VSM that can reach a maximum field of 2.15T with the temperature option or vector coil option in place.

Versatility

The EV Series VSM supports all known types of magnetic measurements such as Hysteresis and minor loops, IRM and DCD Remanence Loops, SFD, Delta M, delta H and Henkel Plots, as well as Angular and AC Remanence Loops, Temperature scans and Time decay measurements. Also, the user has the option to custom create measurements with full

control over system functions. Any series of measurements can be run without user intervention, using the flexible Easy VSM software.

The Model EV9 will be installed as three units:

1) The Measurement Station (includes the magnet/vibrator frame)

2) The Electronics Cabinet

3) The System Computer

The Measurement Station and Electronics Cabinet should be spaced within 3 feet of each other. They will be connected to each other by cables. The computer should be placed on a customer-supplied workstation close to the Electronics Cabinet.

4.10 SQUID MAGNETOMETER

A SQUID (superconducting Quantum Interference Device) is the most sensitive available device for measuring magnetization. Based on this sensitive device the so-called óSQUID magnetometerô has been developed. SQUID magnetometers are used to characterize materials when the highest detection sensitivity over a broad temperature range and using applied magnetic fields up to several Tesla is needed. Nowadays, this instrument is widely used worldwide in research laboratories. The system is designed to measure the magnetic moment of a sample, from which the magnetization and magnetic susceptibility can be obtained. Therefore, SQUID magnetometers are versatile instruments that perform both, DC and AC magnetic moment measurement.

SQUID magnetometers are classified within the flux methods of measuring magnetization of a sample. Fig.4.9 illustrates schematically its principle: the measurement of the flux change through a pick-up coil system with a SQUID. This signal is proportional to the magnetic moment of a sample, which is magnetized by the magnetic field produced by a superconducting magnet.

4.10.1 Basic Components

The main components of SQUID magnetometers are: (a) superconducting magnet (that must be acquired together its programmable bipolar power supply): (b) superconducting detection coil which is coupled inductively to the sample: (c) a SQUID connected to the detection coil: (d) superconducting magnetic shield. In the following a description of each one is given:

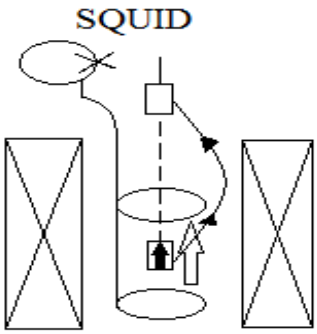

Fig.4.9: SQUID magnetometer principle

Superconducting magnet

A superconducting magnet is a solenoid made of superconducting wire. Fig.4.10 shows a cut away view of a typical superconducting magnet used in a SQUID magnetometer. This solenoid must be kept at liquid-helium temperature in a liquid helium dewar. The uniform magnetic field is produced along the axial cylindrical bore of the coil. Currently, superconducting solenoids that produce magnetic fields in the range 5-18 Tesla are commercially available. To operate a superconducting magnet requires an appropriate programmable bipolar power supply.

Superconducting detection coil

This is a single piece of superconducting wire configured as a second-order gradiometer (Fig.4.10b) this pick-up coil system is placed in the uniform magnetic field region of the solenoidal superconducting magnet.

SQUID: high sensitivity is possible because this device responds to a fraction of the flux quantum. The SQUID device is usually a thin film that functions as an extremely sensitive current-to-voltage-converter. A measure is done in this equipment by moving the sample through the second-order gradiometer. Hence, the magnetic moment of the sample induces an electric current in the pick-up coil system. A change in the magnetic flux in these coils changes the persistent current in the detection circuit. So, the change in the current in the detection coils produce variation in the SQUID up to voltage proportional to the magnetic moment of sample

Superconducting magnetic shield

Superconducting magnetic shield is used to shield the SQUID sensor from the fluctuations of the ambient magnetic field of the place where the magnetometer is located and from the large magnetic field produced by the superconducting magnet.

Applications

Using this kind of equipment one can measure: (a) The real and imaginary components of the AC magnetic susceptibility as a function of frequency, temperature, AC magnetic field amplitude and DC magnetic field value. (b) The DC magnetic moment as a function of temperature, DC magnetic field, and time. Using a specially designed sample with lo intrinsic magnetic moment or low mass are measured. In thin films, for instance, the mass may be smaller than 1 microgram. These materials are therefore difficult to characterize using a extraction or vibrating sample magnetometer but not with a SQUID magnetometer. Also for measurements of magnetic viscosity in permanent magnets; where small changes of magnetization as a function of time must be recorded, a SQUID magnetometer is the best choice.

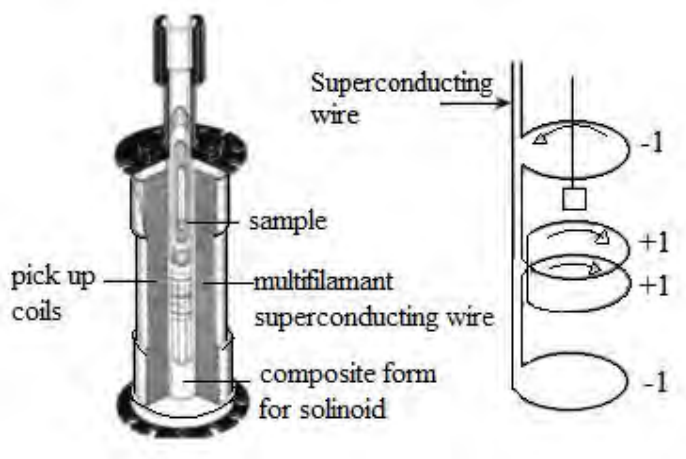

Fig.4.10: (a) Cut view of a typical superconducting pick-up coils.
(b) Second-order gradiometer magnet.

4.10.2 The Features of MPMS XL

Improved sensitivity: The MPMS XL features the new reciprocating sample measurement system. Unlike DC measurements where the sample is moved through the coil in discrete steps the RSO measurements are performed using a servo motor which rapidly oscillates the sample, as shown in Fig.4.11. These measurements have a sensitivity of 5×10^{-9} EMU.

A shaft encoder on the servo motor records the position of the sample synchronous with the SQUID signal. The data received is fitted to an ideal dipole moment response. To ensure this assumption is applicable, sample need to be small: the calibration sample is a cylinder of 3 mm diameter and 3 mm height. Samples of this size or smaller match an ideal point dipole to an accuracy of approximately 0.1%. RSO measurements can be made in one of two configurations: Center or Maximum slope. Center scans use large oscillations (2 to 3cm) around the center point of the pick-up coils. These scans take a long time but the sample always remains properly located and a large number of measurements are recorded. These give the most accurate reading.

The Maximum Slope method oscillates the sample over a small region (2mm) at the most linear part of the SQUID response (as shown in Fig.4.11). The smaller amplitude makes measurements quicker and prevents the sample being subjected to significant magnetic field variation; however it also makes the measurement less accurate and susceptible to drift in the sample position.

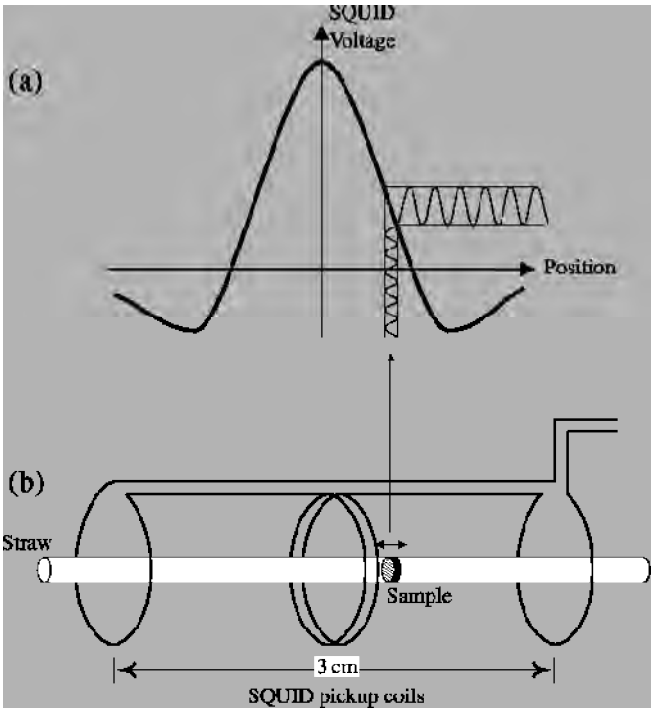

Fig.4.11: Illustration of an RSO measurement with a small amplitude. (a) shows the ideal SQUID response for a dipole and (b) shows the movement of the sample within the SQUID pickup coils.

Extended Low Temperature Capability: The MPMS XL features significant improvements in the temperature control system. Utilizing a new design for the helium flow impedance, the MPMS XL has the capability to operate continuously at temperature below 4.2K for indefinite period of time-completely removing time limitations for making measurements in this temperature regime.

The new MPMS XL eliminates the operations associated with filling and recycling the He reservoir. Thus, the system solves the traditional problems of temperature instability and hysteresis associated with rapid boil off liquid helium when warming through 4.2K. The results are smooth monotonic transitions across 4.2K during both warming and cooling temperature sweeps. All these capabilities are fully automated for precise systems control and user-friendly operation.

Enhanced Thermometry and Temperature Sweep Operation: in addition to a redesigned impedance system, the MPMS XL uses a new thermometer design for improved temperature accuracy and precise thermal control. The new thermometry designed and developed at Quantum design, is installed in close proximity to the sample within the sensitive coil detection region. This improved design is combined with new temperature control capabilities to provide more accurate measurements of the sample chamber, even under extreme temperature changes.

The new temperature sweep mode of operation provides MPMS XL users with the ability to take magnetic measurements while sweeping the system temperature at a controlled rate-automatically-with no manual intervention. This mode provides a controlled, monotonic change in temperature during a measurement sequence at rates up to 10 K/min. measurements of temperature dependence over large temperature ranges, which previously required time consuming temperature stabilization, can now be made quickly and precisely using Temperature Sweep Mode.

Software Control / Automation: a new software interface completes the flexibility and usability of the MPMS XL. Running under Microsoft Windows the state-of-the-art MPMS Multi VU software interface provides a level of control for system operation, graphics and system analysis previously unavailable. With Multi VU, simultaneously viewing data files in multiple formats is easily accomplished. Similarly, display of multi graphs allows for easy comparison of results from different experiments. Operationally, Multi VU is a valuable tool in setting up and editing several measurement protocol files simultaneously.

4.10.3 Specifications

Reciprocating Sample measurement System

Features:

- ⇨ New servo powered, shaft encoded transport allows precision oscillating sample motion
- ⇨ New thermal rod with low thermal expansion and radial sample centering features
- ⇨ New high precision data acquisition electronics including a digital signal processor
- ⇨ New MPMS software revision including a digital signal processor.
- ⇨ New MPMS software revision, including support for all Reciprocating Sample

  Features:

  - SQUID signal analysis phase locked to sample motion.
  - Support of longitudinal and transverse measurements axes.
  - Sample centering methods
  - Support all measurements with new sample transport (AC, DC, Reciprocating Samples)
- ⇨ 16 measurement ranges from 10^{-5} emu to 5 emu.
- ⇨ Frequency ranges: 0.5-4.0 Hz.
- ⇨ Oscillation amplitude range: 0.5 to 50 mm p-p
- ⇨ Max DC scan length: 87 mm
- ⇨ Relative sensitivity: Max. of $<1\times10^{-8}$ emu or 0.1% (0-2500 Oe)
- ⇨ Upgrade available for all basic MPMS system

Continuous Low Temperature control and Enhanced Thermometry

Features:

- ⇨ New dual impedance design allows continuous operation below 4.2K.
- ⇨ New sample space thermometry improves temperature control
- ⇨ Transition through 4.2K requires no ^{4}He reservoir refilling and recycling (no pot fill)
- ⇨ New MPMS software revision for all continuous Low Temperature features

- ⇨ Temperature stability: ±0.5% (1.9-4.2K)
- ⇨ Include temperature sweep feature. Sweep rate range: 0.001-10 K/mim
- ⇨ Upgrade available for all basic MPMS system

Configurations

The MPMS XL is offered in two high homogeneity magnet configurations - MPMS XL 5 (5 Tesla) and MPMS XL 7 (7 Tesla). Each system includes:

- ⇨ Reciprocating sample measurement system
- ⇨ Continuous Low Temperature control/ Temperature sweep
- ⇨ MPMS Multi Vu software Interface

5.1 Identification of Crystallization Temperature by DSC (Differential Scanning Calorimetry):

The crystallization temperature of composition $Nd_4Fe_{76}Cu_{0.5}Nb_1B_{18.5}$ was identified by differential scanning calorimetry (DSC) shown in Fig.5.1. The DSC trace has been measured on an as-cast sample by carrying out measurement in nitrogen atmosphere with a continuous heating rate of 20 K/min. In DSC graph the curve shows a single exothermic peak, which represents the formation of both soft and hard phases within a narrow range of temperature while an endothermic peak represents the melting process of the composition. Li *et al.* [2] has obtained similar exothermic peak of Ŭ-Fe/$Nd_2Fe_{14}B$ based sample. According to Fig.5.1, initiation of crystallization occurs at 600ºC, peak temperature is 613ºC and the crystallization process is completed around 708ºC. At peak temperature the molecules may obtain enough freedom of motion to spontaneously arrange themselves into a crystalline form. This temperature known as crystallization temperature. There is a wide gap between initial and final crystallization temperature. Controlling annealing temperature and time in this region grain size and volume fraction of different crystalline phases can be controlled up to an optimized state.

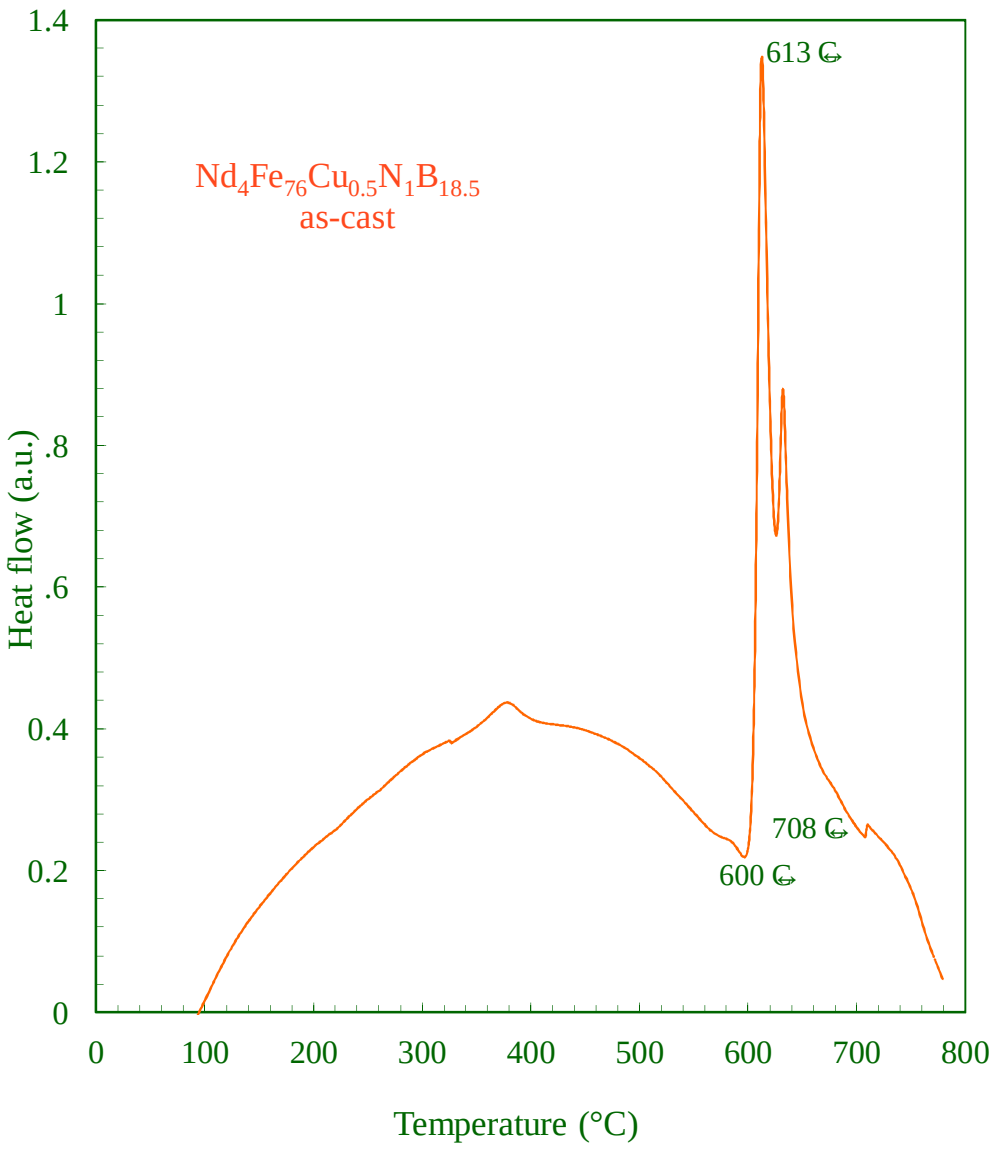

Fig.5.1: DSC trace of $Nd_4Fe_{76}Cu_{0.5}Nb_1B_{18.5}$ in the as-cast condition with a heating rate of 20 K/min

5.2. Identification of phases by X-ray Diffraction (XRD):

We used X-ray diffraction patterns to identify the different phases in the present composition. The X-ray diffraction patterns of as-cast and annealed samples at different annealing temperatures such as 873K, 903K, 913K and 933K are shown in Fig.5.2(a)(b)(c)(d). The XRD results show that major phases have been identified as Fe_3B and 2:14:1 phases. Any diffraction peaks from a probable Ŭ-Fe phase were not identified but might be present in small amount. At higher annealing temperature hard magnetic phases $Nd_2Fe_{14}B$ has started to form though in a small amount in association with soft phase Fe_3B. It was also seen from these patterns that the peak becomes narrower with higher intensity with the increase of annealing temperature. The grain size of the soft phase (Fe_3B) has been determined by using the Scherrerôs formula from Full Width Half Maxima (FWHM) of highest intensity peak (3 3 0) for the samples of different annealing conditions and presented in table (5.1). The formation of this particular nanostructure is ascribed to combined effects of Cu and Nb and their low solubility in iron. It is seen from the table (5.1) that the grain size increases with increasing annealing temperature. Harland *et al.* [12] used X-ray diffraction pattern to reveal the average $Nd_2Fe_{l4}B$ crystallite size which was ~ 32 nm for $Nd_9Fe_{86}B_5$ alloy and ~ 26 nm for $Nd_2Fe_{l4}B$ alloy, confirming the nanocrystalline nature of the materials. It was not possible to determine Ŭ-Fe grain size from the XRD data because the Fe peaks overlap with $Nd_2Fe_{l4}B$ peaks. The outstanding permanent magnet properties observed in ternary alloys Nd-Fe-B result from the formation of a new phase $R_2Fe_{14}B$ (R - rare earth) whose quadratic crystal structure was recently and independently determined by Herbst *et al.* and by Givord *et al*. In this structure, Nd atoms are distributed on 2 crystallographic sites of low symmetry, whereas Fe atoms occupy 6 different sites. Sagawa *et al.* have shown that the phase $R_2Fe_{14}B$ is stable with R = Nd to Tm and with Y. A quantitative study of the magnetic behavior of these compounds on single crystals should be very meaningful for a microscopic understanding of the permanent magnet properties observed. Very generally in R-M (M = transition metal) alloys the large 3d magnetic interactions are dominant and determine ordering temperature well above room temperature [7].

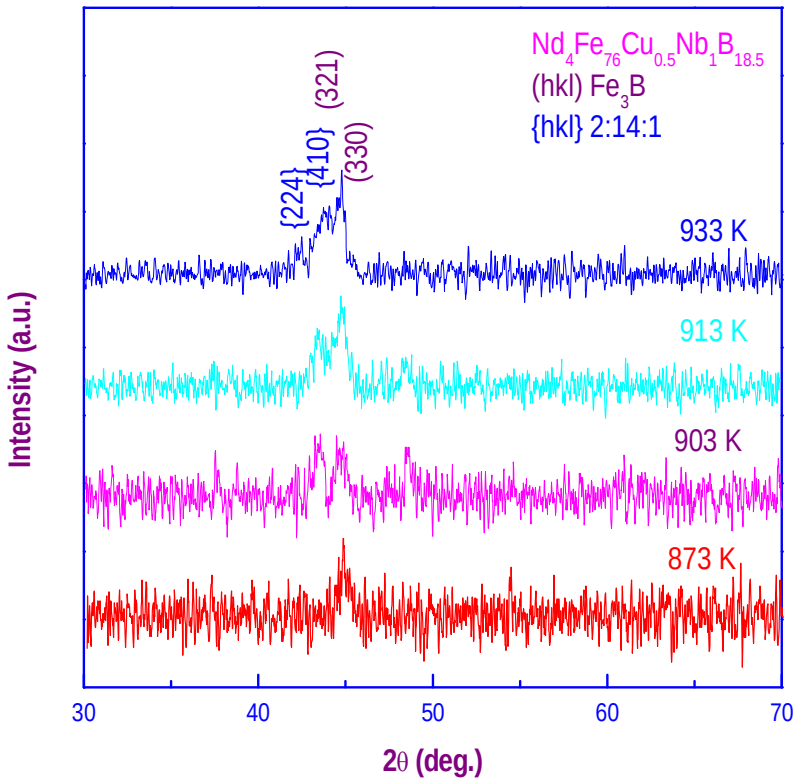

Fig.5.2: XRD patterns of $Nd_4Fe_{76}Cu_{0.5}Nb_1B_{18.5}$ for the samples annealed at different annealing temperatures.

5.3. Hysteresis loop analysis:

Hysteresis loops obtained at different annealing temperatures have been presented in Fig. 5.3(a)(b)(c)(d). With the variation of annealing temperature it has been found that the sample is magnetically very soft at 873K. At the annealing temperature of 873K hysteresis loop is constricted since the crystallization process has not been completed and phases are not exchange-coupled. For higher annealing temperature, with the evolution of phases exchange-coupling between Fe_3B and $Nd_2Fe_{14}B$ led the hysteresis loop to convex shape which resembles to the single phase hard magnetic materials.

The values of saturation magnetization M_s, coercivity H_c, remanent ratio M_r/M_s and the maximum energy product $(BH)_{max}$ derived from the hysteresis loops have been presented in table(5.1). The grain sizes of the soft phase of highest intensity peak for different annealed samples are also presented in table (5.1). While varying annealing temperature, coercivity, remanent ratio and maximum energy product increase with increase of temperature. It is seen from this table (5.1) that the highest value of maximum energy product is 9.87 MGOe for the annealing temperature 933K and the highest value of coercivity is 3.30 kOe for the same annealing temperature 933K. All the samples possess high remanent ratio. We have obtained the highest value of remanent ratio is 0.765. S. Manjura Hoque *et al.* obtained the highest value of coercivity, remanent ratio, and maximum energy product for the composition $(NdPr)_4Fe_{71}Co_5Cu_{0.5}Nb_1B_{18.5}$ which were 4.08 kOe, 0.747 and 11.07 MGOe respectively, while those values of $Nd_{3.5}Tb_1Fe_{76}Cu_{0.5}Nb_1B_{18.5}$ were 4.76 kOe, 719 and 9.43 MGOe respectively. It is also seen from this table (5.1) that the grain size increases with increasing annealing temperature and the highest value for our present composition is found around 12.28 nm.

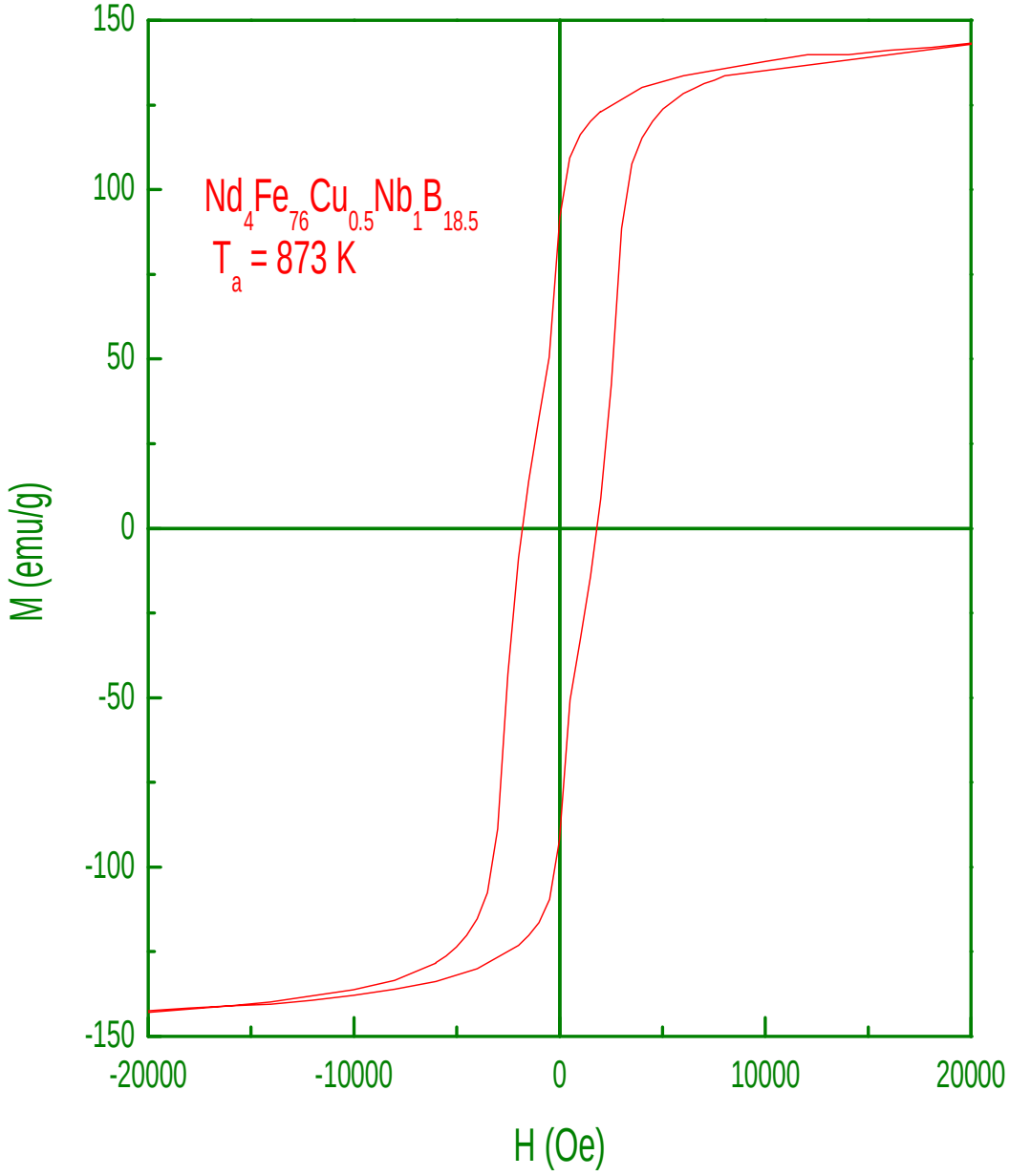

Fig.5.3(a): Hysteresis loop of sample of composition $Nd_4Fe_{76}Cu_{0.5}Nb_1B_{18.5}$ at 873K.

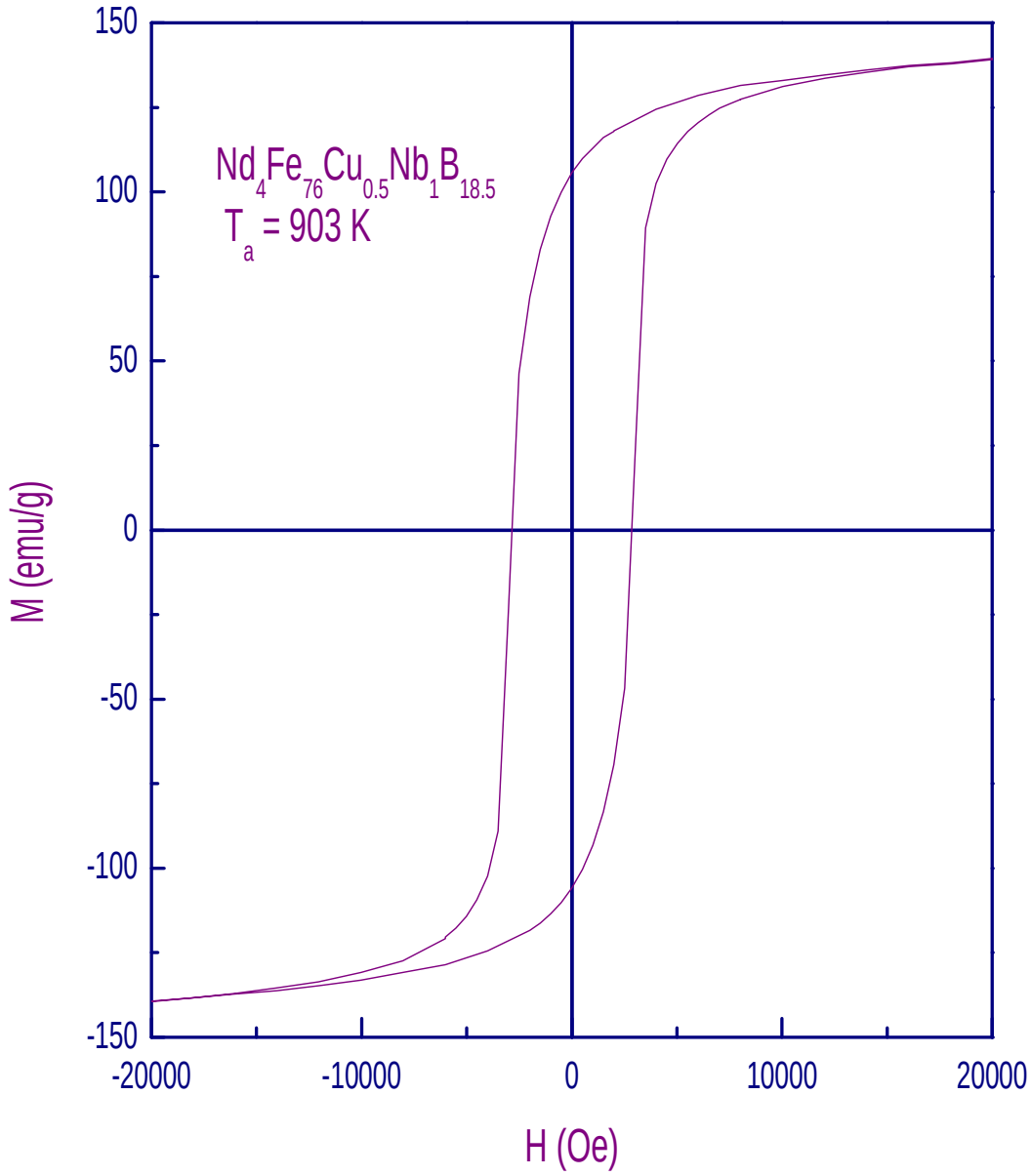

Fig.5.3(b): Hysteresis loop of sample of composition $Nd_4Fe_{76}Cu_{0.5}Nb_1B_{18.5}$ at 903K.

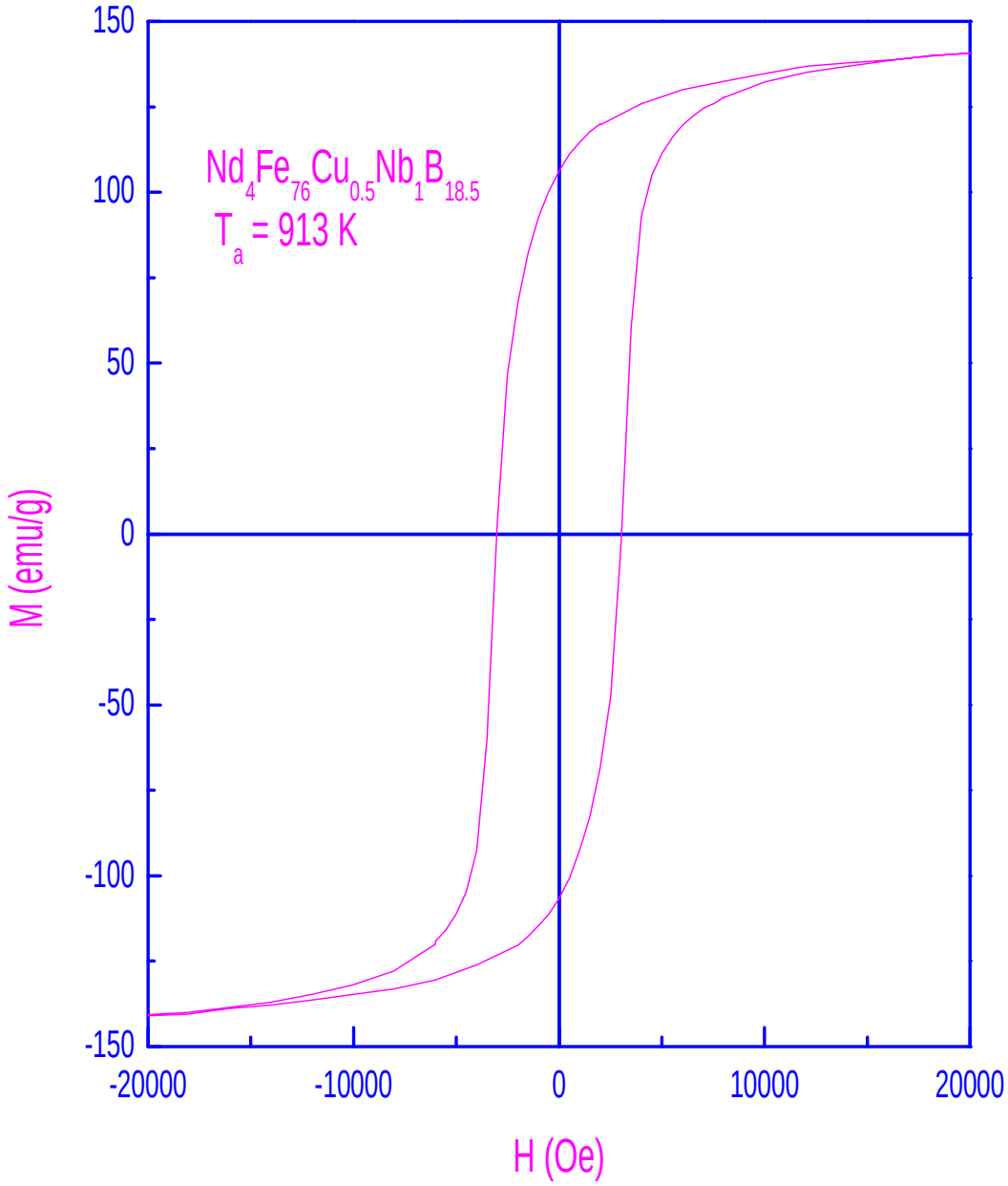

Fig.5.3(c): Hysteresis loop of sample of composition $Nd_4Fe_{76}Cu_{0.5}Nb_1B_{18.5}$ at 913K.

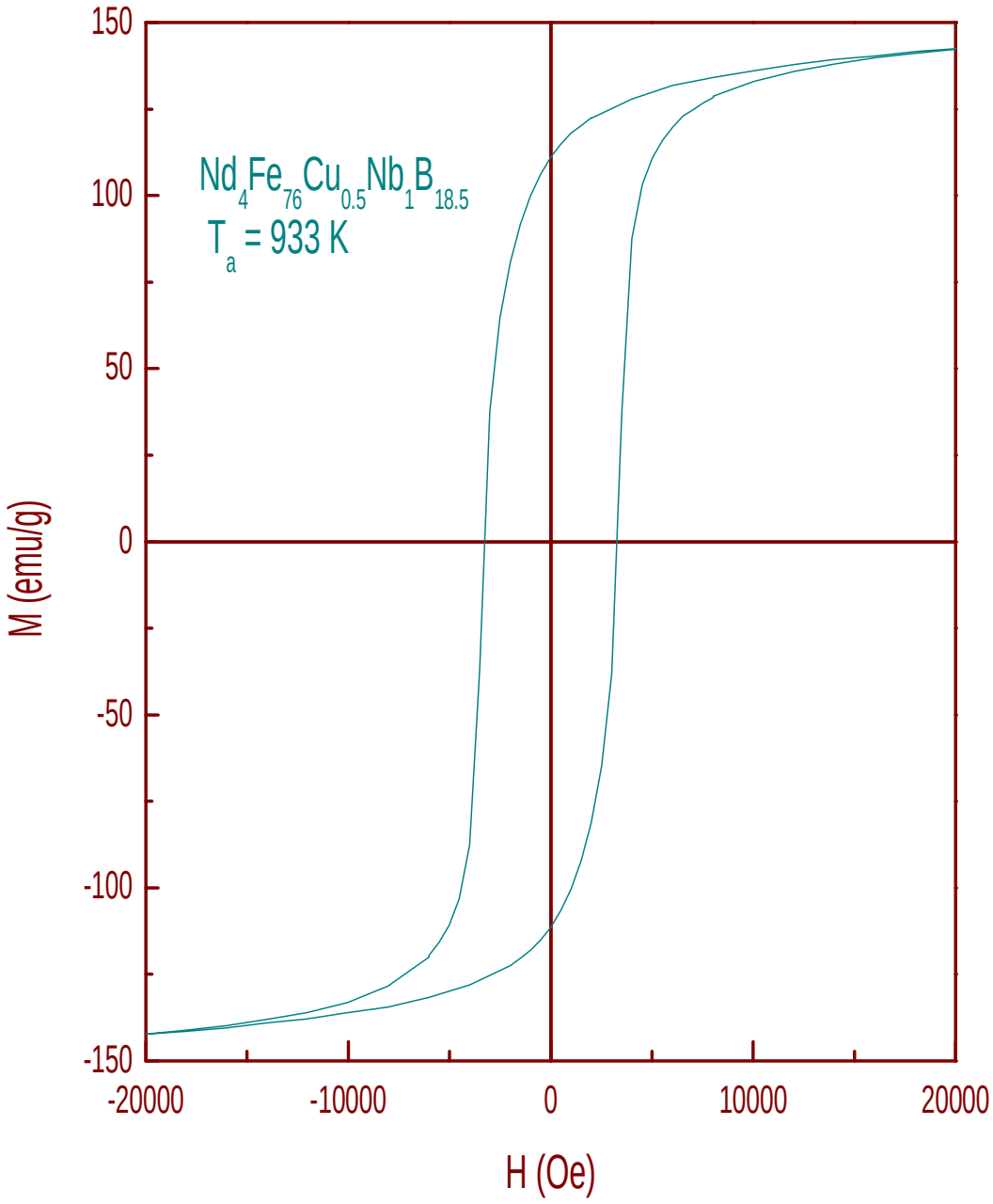

Fig.5.3(d): Hysteresis loop of sample of composition $Nd_4Fe_{76}Cu_{0.5}Nb_1B_{18.5}$ at 933K.

Table analysis: Table 5.1 Hysteresis parameters and grain size for $Nd_4Fe_{76}Cu_{0.5}Nb_1B_{18.5}$

Annealing temperature K	**Annealing time Min.**	**M_s emu / g**	**H_c kOe**	**M_r/M_s**	**$(BH)_{max}$ MGOe**	**Grain size of Fe_3B nm**
873	10	145	1.89	0.639	1.97	8.45
903	10	143	2.80	0.742	8.71	10.75
913	10	145	3.06	0.731	8.62	11.31
933	10	146	3.30	0.765	9.87	12.28

5.4. Recoil hysteresis loop analysis:

Fig.5.4(a) and (b) show room temperature (300K) hysteresis loops along demagnetization branch for the sample annealed at 903K and 933K i.e. in the initial and the over annealed condition. Some minor loops are shown the same figure, as they are obtained upon reducing the field to zero and re-increasing the field at various points along demagnetization curve. From these figures recoil loop area as a function of reverse field for annealed samples are presented in Fig.5.5. Kang *et al.* [5] observed in his experiment that the recoil loop area continues to increase and then decreases with increased reverse fields. Because recoils originating from increasingly negative fields represent an increased amount of phase reversal, the relative amount of reversing material during recoil becomes smaller, creating more closed recoil loops. As increasing portions of the hard phase reverse with increasing reverse field, there is less polarization oriented opposite to the applied field direction to keep the soft phase aligned. Consequently recoil loops measured at larger negative reverse field show a much smaller area [5]. These two annealed sample exhibit a maximum recoil area at 3000 Oe and 3200 Oe respectively, before and after which, however, significantly closed recoil loops are observed. That creates a narrow field distribution of recoil area. This result illustrates the slightly stronger exchange-spring character of these annealed states [5]. C. L. Harland [12] investigated the recoil behavior of nanocrystalline materials based on $Nd_2Fe_{l4}B$. The onset of recoil hysteresis, or attainment of appreciable area of the recoil loop, was determined and followed as a function of the reverse applied magnetic field. Its behavior was correlated with that of two other independent parameters: (i) the reversible portion of the recoil susceptibility and (ii) the recoil remanence. Both (i) (ii) provide information on the ease of remagnetization of the materials. The simultaneous appearance of extrema in a restricted internal field range in all three parameters strongly suggests that the area of the recoil loops in these materials may be taken as a measure of the extent of the intergranular exchange. The recoil behavior of nanocrystalline $Nd_2Fe_{l4}B$ and $Nd_2Fe_{l4}B$+Ŭ-Fe nanocomposite materials, as quantified by the normalized recoil loop area, the recoil remanence ratio B_{recoil}/B_r and the reversible recoil susceptibility $\chi_{rev,}$ is measured by Harland and analyzed to further elucidate the origins of the enhanced degree of intergranular coupling in these materials [12]. Harland *et al.* [12] have mentioned that the development of the area of the recoil curve with reverse field and temperature provides information about the breakdown of exchange coupling of $Nd_2Fe_{14}B$/Ŭ-Fe nanocomposites. Thus it can be observed in Fig.5.4(a)(b) that there is an evolution of recoil loop area with the increase of reverse field and recoil loop area is maximum at coercive field for which recoil loop does

not trace major demagnetization curve. The recoil permeability of the remagnetized recoil portion in the sample annealed at 933K is much higher than that found in 903K. Harland *et al.* found that the nominally stoichiometric $Nd_2Fe_{14}B$ sample does not exhibit significant recoil loop area at room temperature until 7 kOe, while the nanocomposite sample recoil area appears at much lower fields, around 3.5 kOe [12].

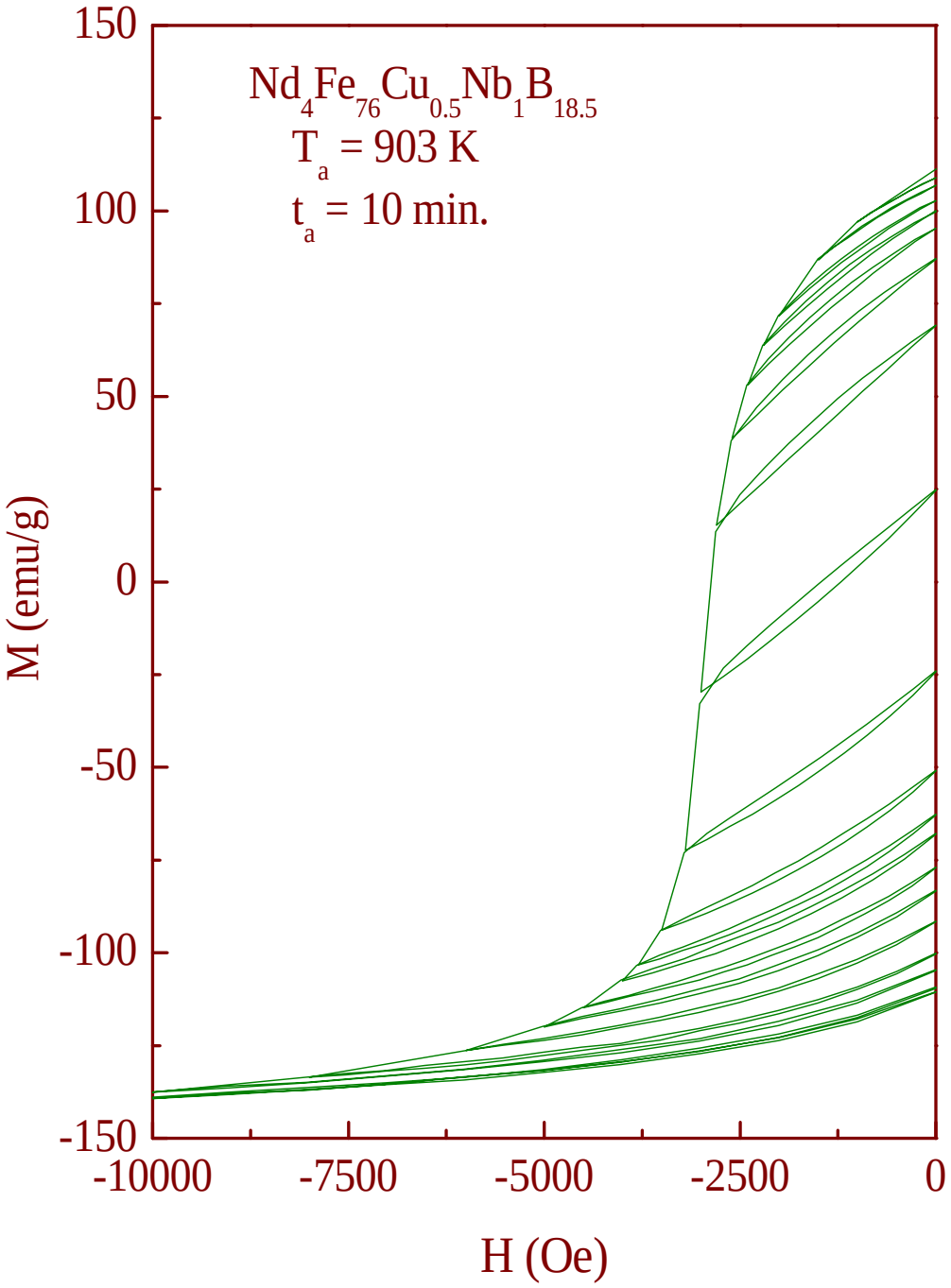

Fig.5.4(a): Recoil hysteresis loops for sample annealed at 903K for 10 minutes.

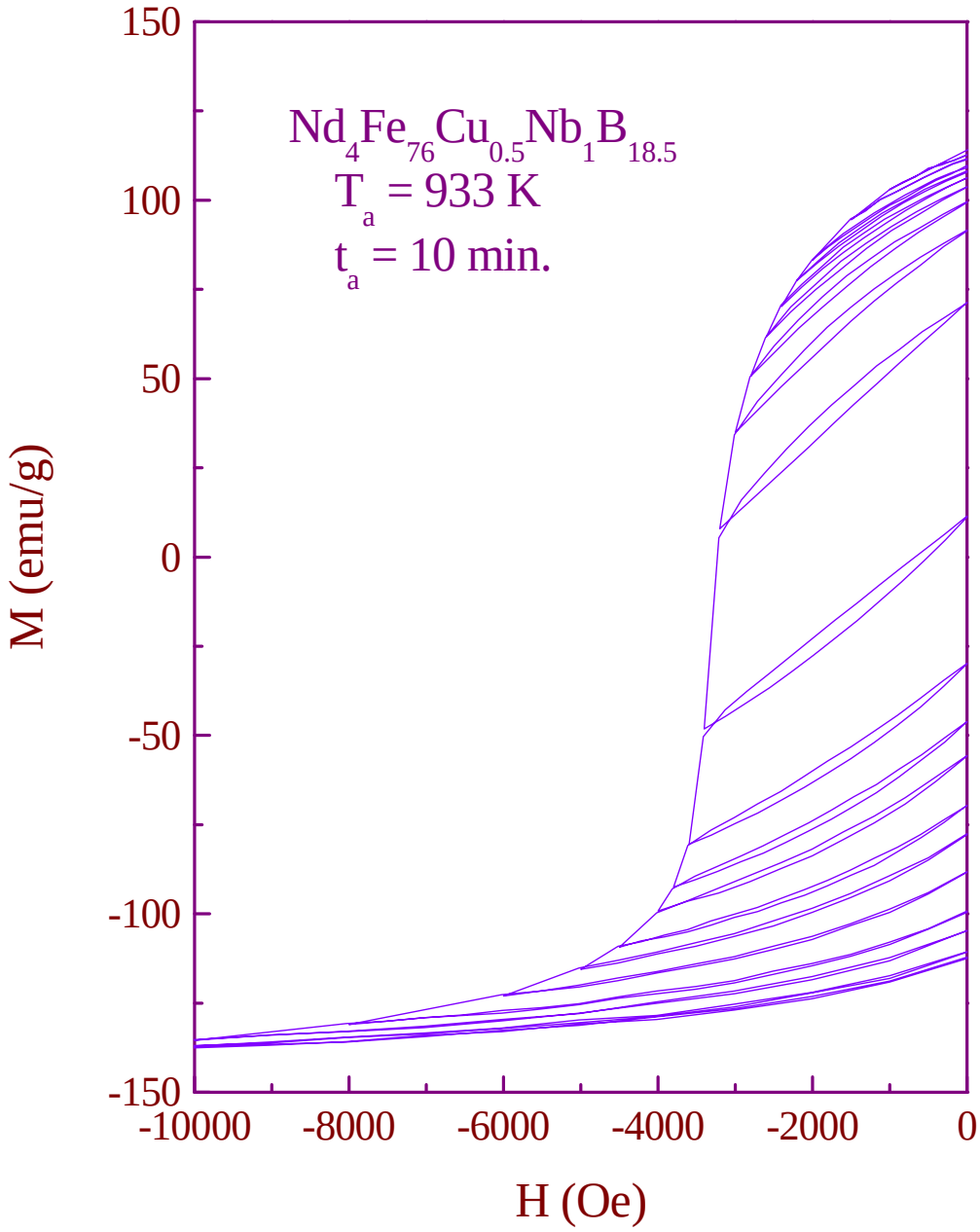

Fig.5.4(b): Recoil hysteresis loops for sample annealed at 933K for 10 minutes.

5.5. Analysis of total magnetization change:

Feütrill *et al.* carried out a simulation of the magnetization reversal process in a simplified permanent magnetic nanocomposite and concluded that reversal involves a unique interplay between the distribution of energy barriers of the flipped and unflipped states, as well as between the hard and soft components of the nanocomposite. Such work is notable for its examination of the reversible, irreversible and ñrecoverableò proportions of the total magnetization and magnetic susceptibility as determined by recoil curves recorded at different micromagnetic states conferred by given field and temperature conditions [12]. In Fig.5.5 the area of recoil loops normalized to the area of half of the major hysteresis loop are plotted as a function of the reverse field H. The areas have been extracted by numerical integration of the recoil curves of Fig.5.4(a)(b). Below the critical field, the magnetic moment when returning to the demagnetizing field is very close to the starting value. The sample annealed at 933K shows a narrow recoil area peak compared to the sample annealed at 903K. The development of the loop area is due to the decoupling of the magnetic moment between soft and hard phases [5]. The recoil area shows a pronounced maximum at the field where the largest number of hard phase grains switch magnetization direction. These fields are quoted in the Fig.6.5 and the amounts of these fields are 3000 Oe and 3200 Oe for the sample annealed at 903K and 933K respectively. Fig.5.5 shows a narrower recoil area peak for the sample annealed at 933K compared with that of 903K, reinforcing the conclusion of stronger exchange-spring character in the annealed state. Kang *et al.* [5] pointed out that the peak in the recoil area is coincident with the coercivity of the hard component while the departure from zero recoil area at low reverse fields corresponds to the inter-phase exchange field H_{ex}. It is to be noted that the peak values of the sample annealed at 903K and 933K for 10 minutes are closer to the coercivity value obtained from the hysteresis loop for this sample presented in table (5.1). Annealing produced the expected softening of the hard phase component; however, the annealing treatment is found to retard the development of low field recoil area. Harland *et al.* observed two main features from his experiment. The first feature to note is that significant changes in the reversible susceptibility coincide with the onset of recoil loop hysteresis in both samples, but only at room temperature. The second feature to note is that the fields corresponding to the onset of recoil hysteresis and the maximum in the reversible component of the recoil susceptibility differ to large degree, in a systematic manner, as the temperature is lowered [12].

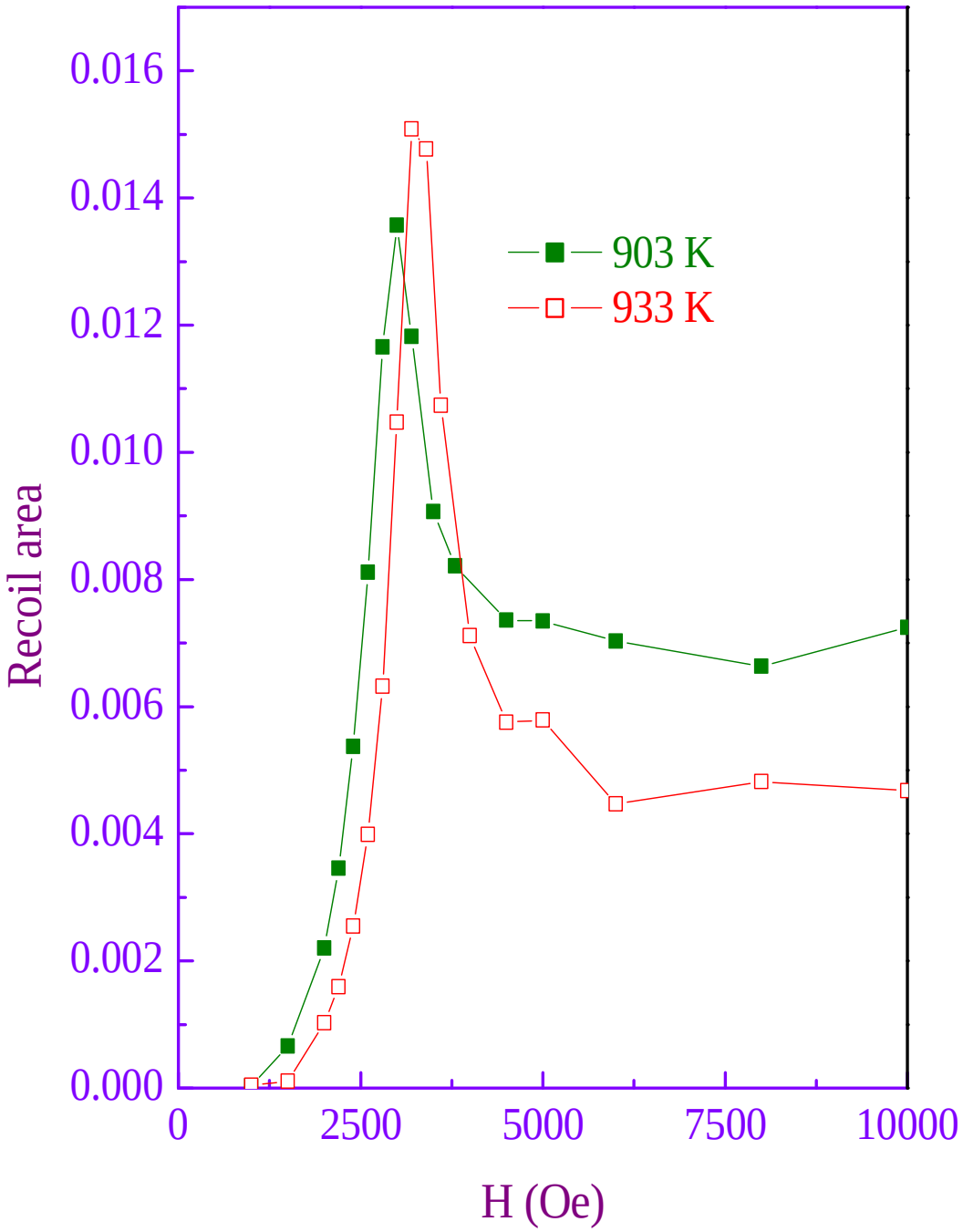

Fig.5.5: Recoil loop area as a function of reverse field for annealed samples.

In Fig.5.6 the reduced quantity/irreversible component of magnetization $D(H) = [M_r - M_d(H)]/2M_r = -\Delta M_{irrev}(H)/2M_r$ is plotted versus reverse field H, where M_r is the saturation remanence and $M_d\ (H)$ is the dc field demagnetization remanence i.e the remanence acquired after saturation in one direction and subsequent application of a dc field H in the opposite direction. The curves of Fig.5.6 provide information about the stability of the reversible state and the critical field of irreversible changes of the magnetization. For the sample annealed at 903K, the $D(H)$ versus H curve is characterized by relatively sharp change of $D(H)$ at the critical field where irreversible change in the hard phase is relatively large, whereas for the samples annealed at 933K the change is more gradual. Below the critical field of around 3000 Oe, change in ΔM_{irrev} is small and magnetization almost return to the remanent configuration when the field is decreased back to zero. Kang *et al.* pointed out a sharp drop in the remanent magnetization ratio, coincident with the determined irreversible magnetic field $H_{irr.}$ The wider field distribution of the magnetization drop in the remanent magnetization ratio is attributed to the wider distribution of exchange coupling strength [5]. C. L. Harland *et al.* Recoil curves in nanocrystalline permanent magnetic materials are typically not completely reversible with field and show a degree of hysteresis, which allows the area enclosed by the recoil curves to be determined as a function of the reverse applied field. So it is more appropriate for reversible magnetization to refer to the ñrecoverableò magnetization. To determined the recoverable change in magnetization, $M_{recov,}$ upon removal of the demagnetizing field such that $M_{demag}\ (H) = M_{recov} + M_{irr}$, where M_{irr} is the irreversible magnetization remaining at zero internal field. This irreversible magnetization is equivalent to the recoil remanence B_{recoil} in exchange coupled nanocrystelline magnets. The recoverable amount of magnetization obtained after demagnetization from a particular reverse field, M_{recov}/B_r, provides information about the stability of the magnetization against application of opposite magnetic fields [12].

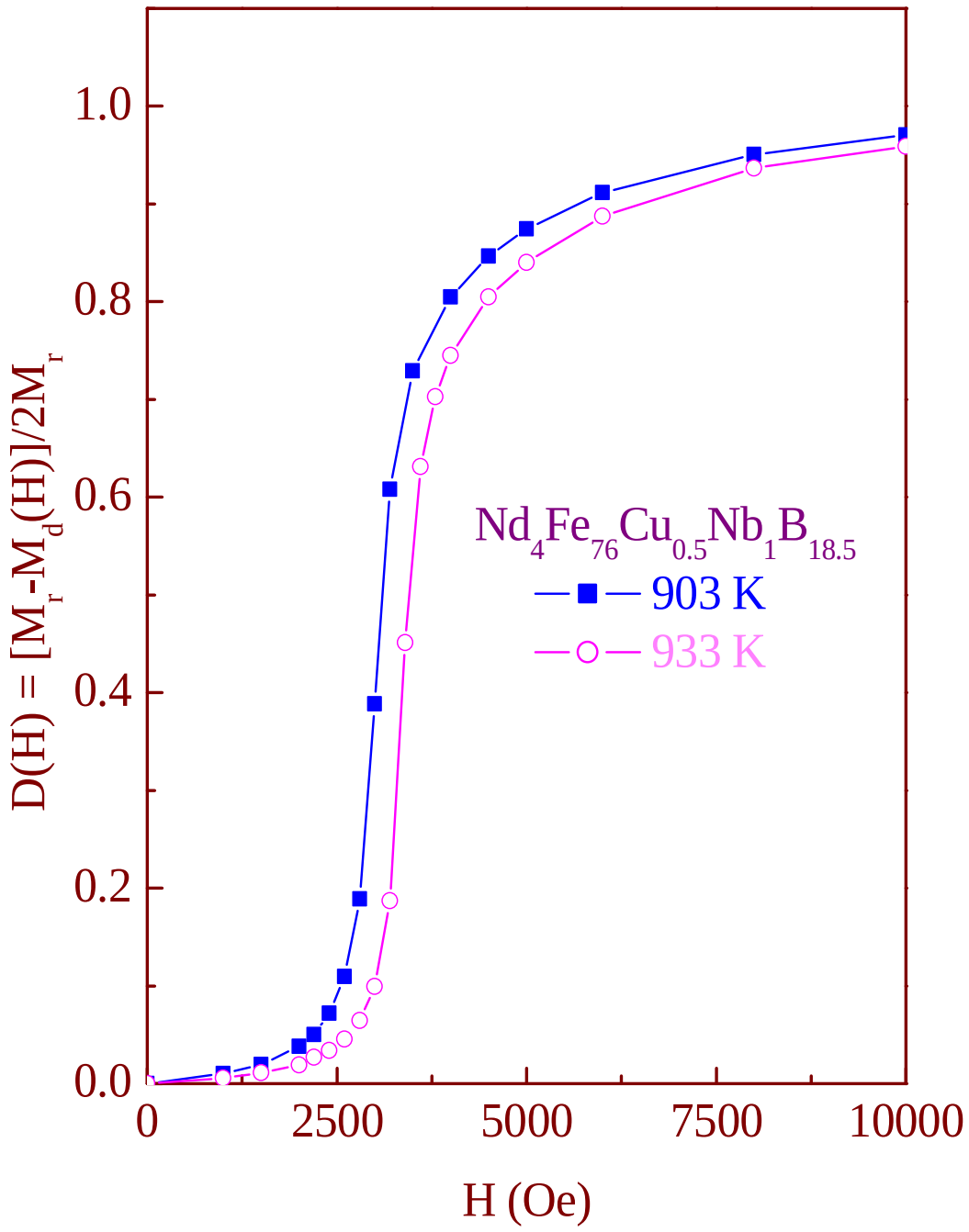

Fig.5.6: Measurements of the irreversible portion $D(H) = -æM_{irrever}(H)/2M_r$ versus H for the samples annealed at 903K and 933K.

5.6. Temperature dependent Properties

(I) Temperature dependent hysteresis loop:

The temperature dependence of the results provides information about the thermal evolution of the interphase exchange coupling; this information is not evident in major loop measurements [12]. The extent of the intergranular exchange coupling in these types of isotropic materials is typically evaluated by the remanence ratio. Materials with a remanence ratio greater than the theoretically predicted value of 0.5 show some degree of remanence enhancement due to the intergranular exchange, with a large remanence ratio indicative of greater remanence enhancement. While evaluation of remanence ratio is convenient, it does not provide specific information about the nature of the magnetic reversal that exists in the constituent phases, nor does it indicate the field dependence of the interphase exchange coupling breakdown [12]. For the sample annealed at 903K, temperature dependence of hysteresis loop has been obtained in the temperature range of 5K to 300K for 10 minutes with a maximum applied field of 2 tesla. Some representative hysteresis loops are shown in Fig.5.7(a)(b)(c)(d)(e)(f) and derived hysteresis loop parameters at different temperatures are shown in Fig.(5.8). The shape of the hysteresis loop changes at 100K and below, which is related to the spin re-orientation in the hard phase that occurs at low temperatures. This change in the shape of the hysteresis loops agree with the previous measurements[6-8]. In ref [11] it was observed that the hysteresis loop for $Nd_2Fe_{14}B$/Ŭ-Fe become constricted below spin re-orientation temperature, i.e. with the decrease of temperature the magnetization curve becomes more discontinuous at low field. At lower temperature, field dependence of magnetization shows discontinuous behavior at low fields. Hadjipanayis *et al.*[11] have reported similar discontinuity at low field at the temperature below135K, i.e. the spin reorientation temperature of $Nd_2Fe_{14}B$. Several authors have noticed the onset of a kink at low negative fields in the hysteresis loops of Nd-Fe-B permanent magnets at room temperature. In Givord experiment a new phenomenon has developed below 150K characterized by a kink which at 4.2K is such that æM/2M is ~ 20%. Unlike the previous kink at room temperature, the kink observed at 4.2K corresponds to a reversible mechanism. This kink in the hysteresis loops has been related to either oxidation, the existence of another phase, or to the occurrence of two distinct mechanisms in the coercivity process [6]. D. Givord observed that there is a much large anomaly in the hysteresis cycles at low temperature, revealed by a kink in low fields [6]. As suggested by Strnat *et al.* and Kuntze *et al.*, this phenomenon must be associated with the spin

reorientation occurring in the $Nd_2Fe_{14}B$ compound below 130K. They show that it results from combined effects of the spin reorientation and incomplete alignment of the grains in the magnets. Givord in his experiment found that the magnitude of the kink increases as the grain size of the sample decreases. These properties show that the magnets can be considered as an assembly of Ŭgrains with a high coercivity and 1 ï Ŭgrains with a reduced value of the coercivity [6]. Givord *et al.* [6,7] found from the studies of powdered and single crystalline $Nd_2Fe_{14}B$, that at temperature below 135K there is an angle ɗ between the easy magnetization direction and the c-axis that progressively increases and amount to about 30° at low temperatures.

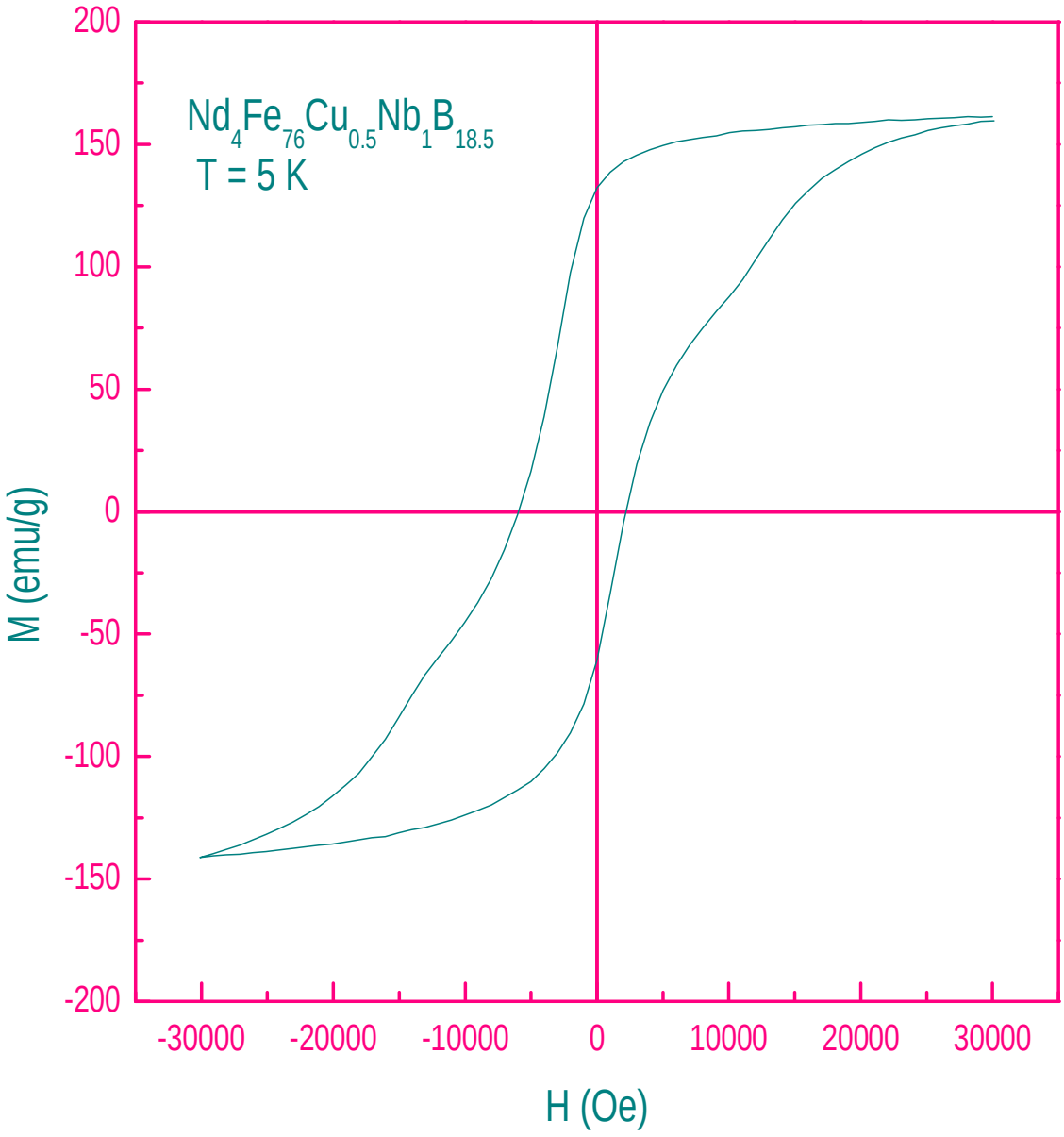

Fig.5.7(a): Temperature dependence (5K) of hysteresis loop for samples annealed at 903K for 10 minutes.

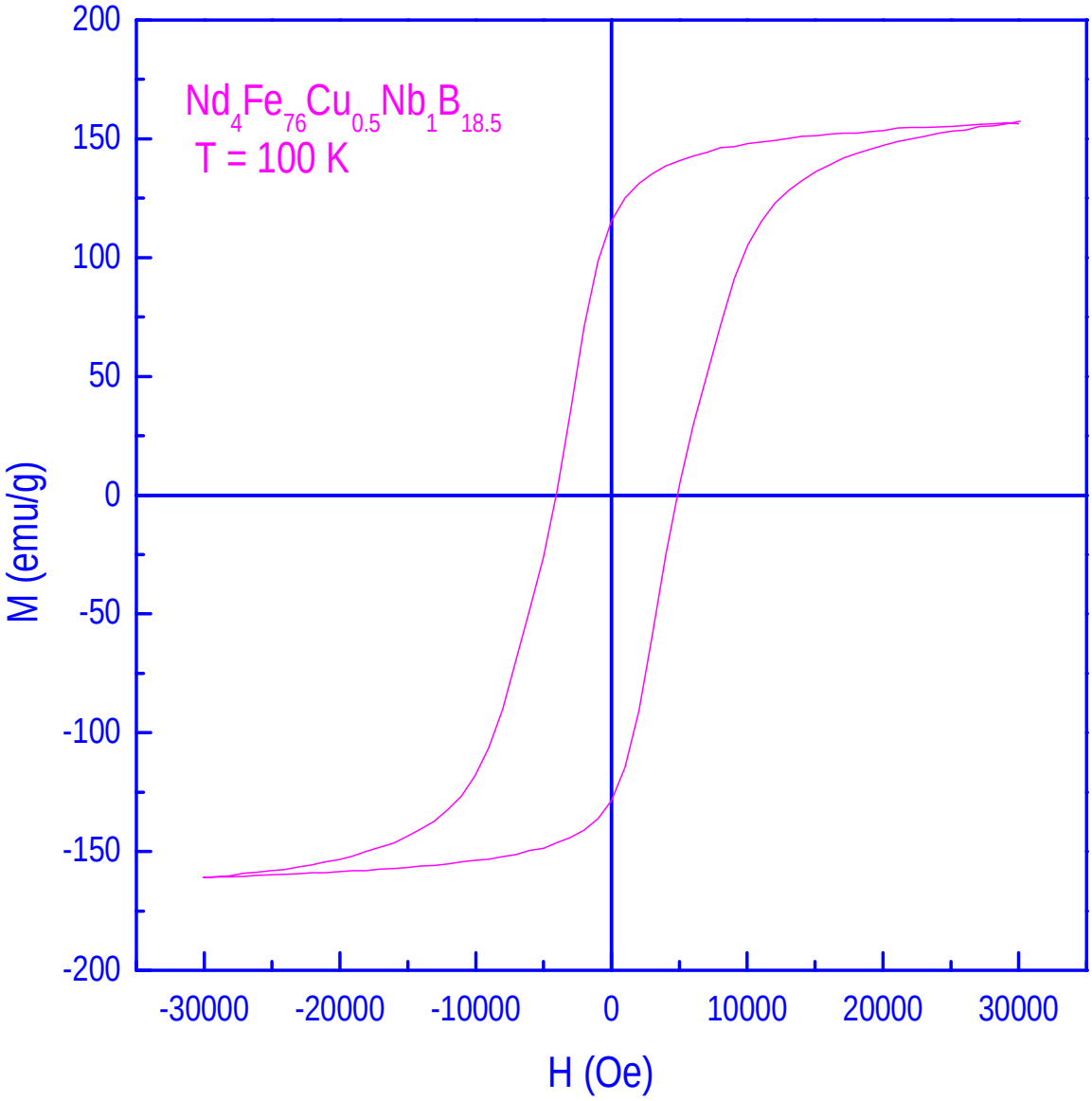

Fig.5.7(b): Temperature dependence (100K) of hysteresis loop for samples annealed at 903K for 10 minutes.

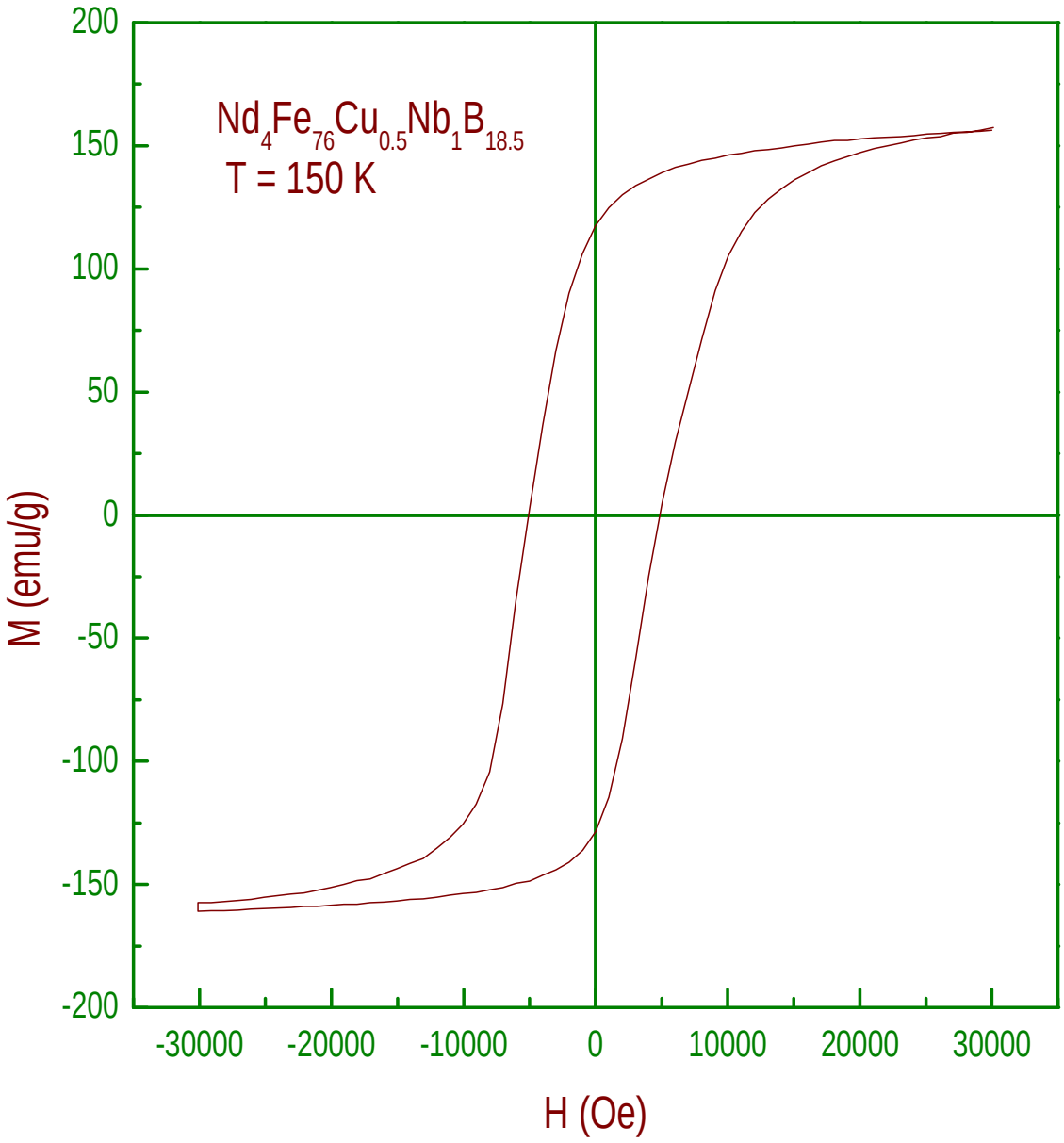

Fig.5.7(c): Temperature dependence (150K) of hysteresis loop for samples annealed at 903K for 10 minutes.

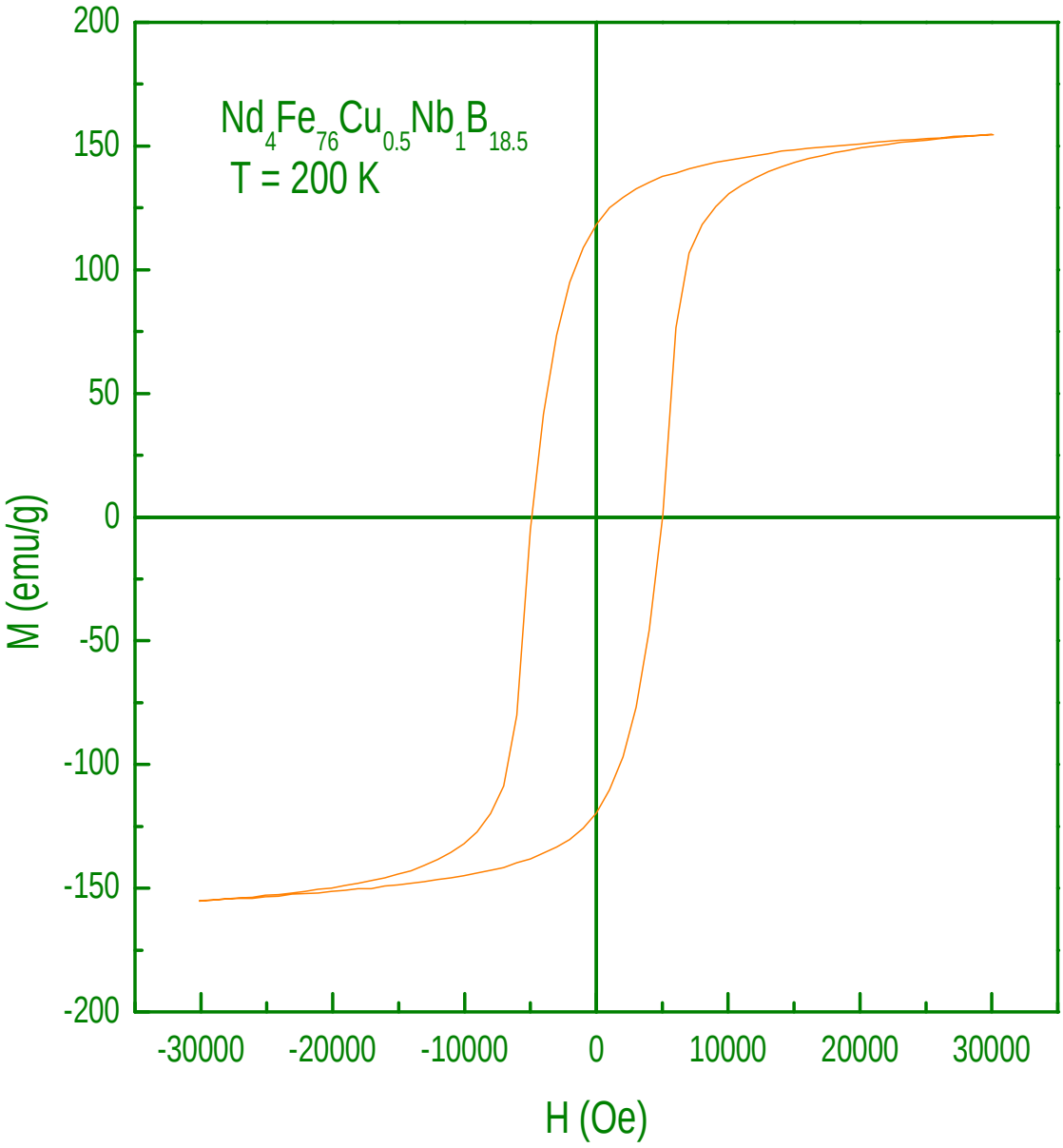

Fig.5.7(d): Temperature dependence (200K) of hysteresis loop for samples annealed at 903Kfor 10 minutes.

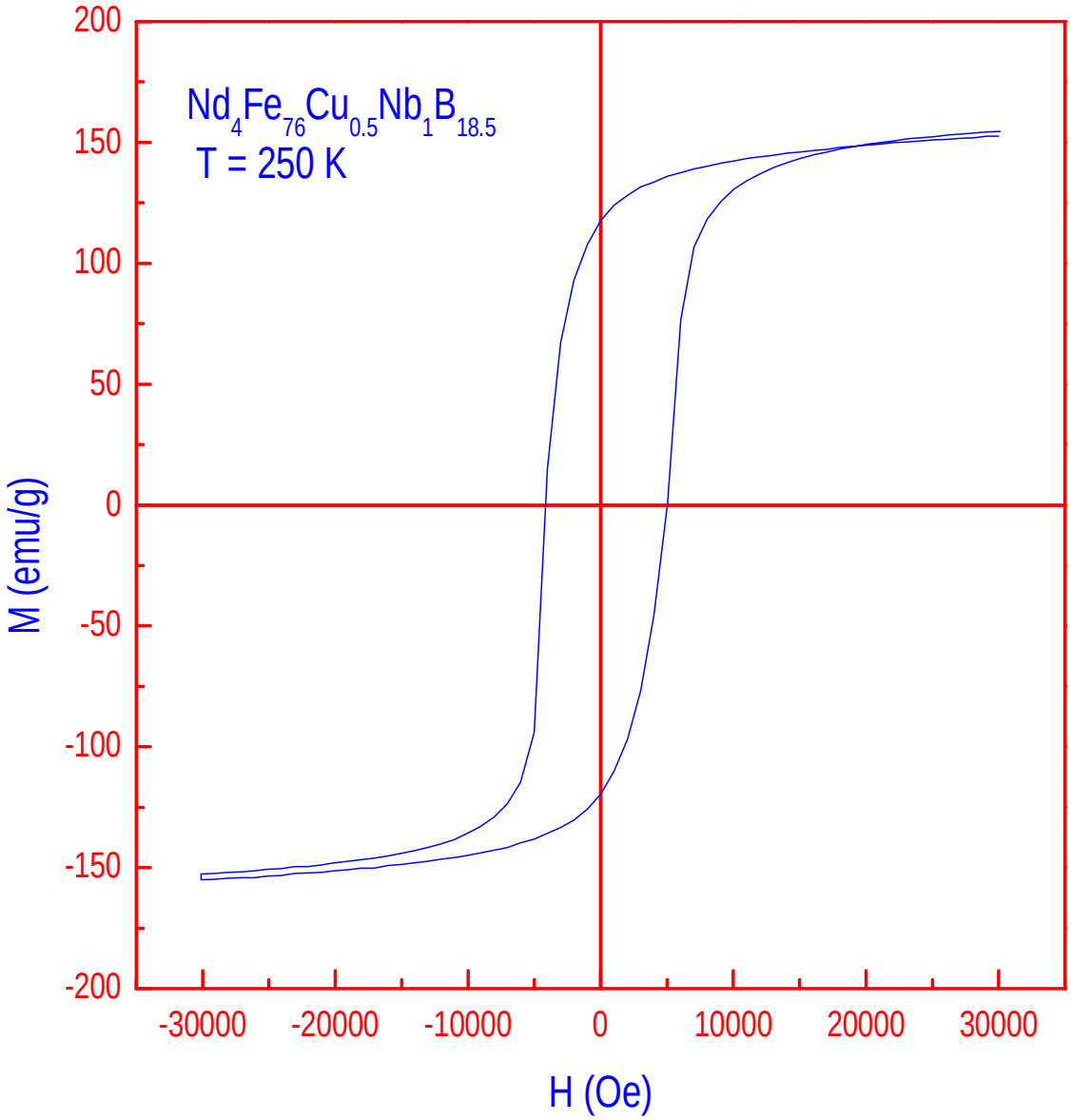

Fig.5.7(e): Temperature dependence (250K) of hysteresis loop for samples annealed at 903K for 10 minutes

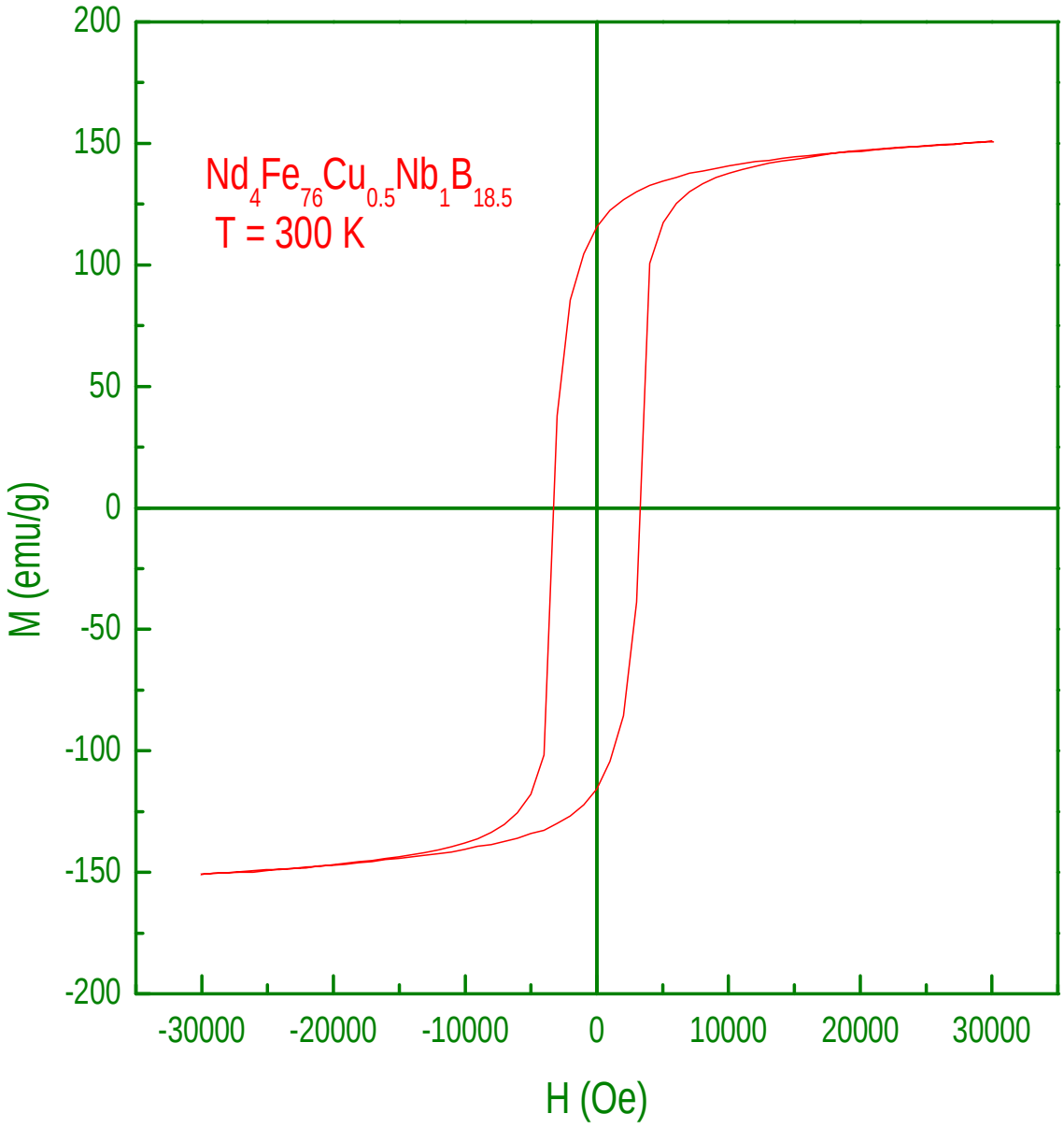

Fig.5.7(f): Temperature dependence (300K) of hysteresis loop for samples annealed at 903K for 10 minutes

(Π) Temperature dependent hysteresis loop parameters:

Hysteresis loop parameters have been derived from Fig.5.7 at different temperatures and plotted as a function of temperature in Fig.5.8. Here three parameters, temperature dependence of the coercivity (H_c), the remanent ratio M_r/ M_s and maximum energy product $(BH)_{max}$ are plotted. The coercivity increases with decreasing temperature. At 150K the coercivity is maximum and below this temperature there is a decrease of the slope of H_c (T). Further decrease of temperature i.e. below 100K there is a slight decrease. The decrease of the coercivity at low temperature is related to the spin re-orientation [7]. This behavior of H_c (T) may be compared with that reported in ref 7 in which a strong decay of the coercivity at low temperature is observed. Givord and Li *et al.* observed the magnetization reorientation at low temperature results from competition between exchange and anisotropy. The temperature dependence of remanent ratio is also governed by the temperature dependence of anisotropy field. The value of M_r / M_s decreases with the increase of temperature because of easier domain wall motion due to the reduction of the anisotropy field at higher temperature. Temperature dependence of maximum energy product $(BH)_{max}$ increases with increase of temperature at first, gives the highest value at 200K. $(BH)_{max}$ also decreases with further increase of temperature above 250K due to the reduction of anisotropy field. Harland *et al.* observations support the interpretation that at lower temperatures the magnetically soft portions of the material decoupled from the hard phases and reverse under the influence of a relatively small reverse fields, giving rise to open recoil curves. At yet higher reverse fields, the magnetically hard portions of the sample start to reverse at initial fields corresponding to the maximum in the G_{rev} signal. It is likely that the non-uniform grain structure of the melt-spun samples gives rise to a continuum in the portion of the sample that decouple and reverse at a given reverse internal field value. The correlation and identification of the onset of appreciable recoil loop area with the initiation of soft phase magnetic reversal, and of the maximum in the reversible susceptibility with the beginning of hard phase reversal, as well as the observed temperature dependence of these two experimental parameters, are consistent with accepted understanding of exchange coupling in magnetic nanocomposites. As the temperature is lowered, the magnetic exchange length decreases and the hard and soft phases no longer reverse at the same field, indicative of a breakdown in exchange coupling. Significantly, this breakdown is not manifest in the major hysteresis loop measurements, which still show a single-phase demagnetization, and can only be monitored by recoil loop measurements [12].

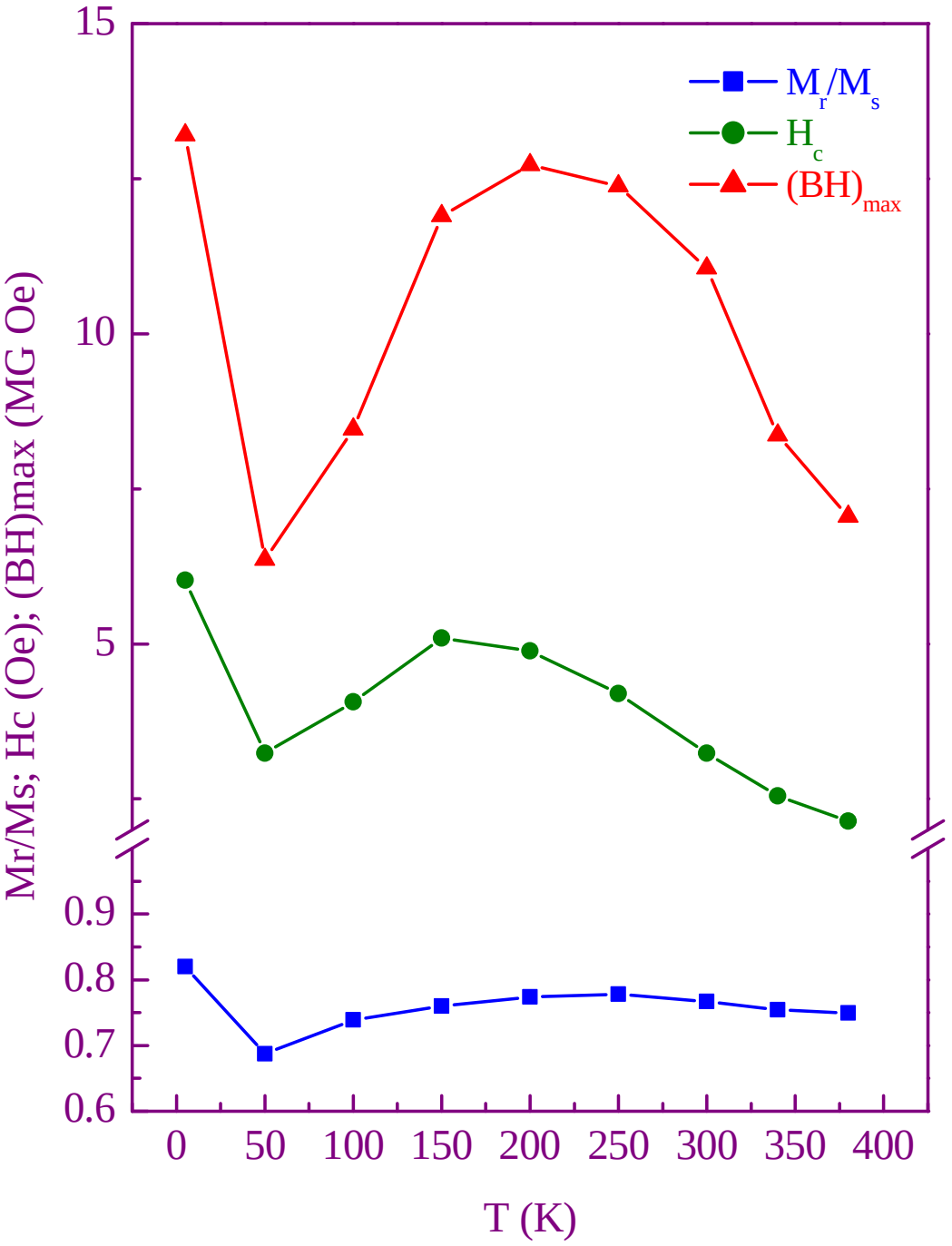

Fig.5.8: Temperature dependence of hysteresis loop parameters.

Conclusions

The permanent magnetic alloy of composition $Nd_4Fe_{76}Cu_{0.5}Nb_1B_{18.5}$ consisting of two suitably dispersed ferromagnetic and mutually exchange-coupled phases, one of which is hard magnetic (high magnetocrystalline anisotropy K) and thus provides a high resistance against irreversible magnetization reversal, while the other is magnetically soft having a high saturation induction J_s to provide a high average magnetization of the material.

Some metallurgical principles should be followed after the technological realization of such composites. Both the hard and soft phases must be crystallographically coherent as a necessary condition for mutual exchange coupling and, therefore, must emerge from a common matrix phase. This matrix phase must basically be soft, and magnetically hard inclusions in it (schematic model in Fig.3.7) may be obtained by, e.g., homogeneous precipitation, or by transformation of a suitably composed and distributed remainder of a primary continuous decomposition of matrix phase into other soft magnetic phases.

The key product in this process, a metastable common matrix phase of a suitable composition, is most conveniently obtained as the first crystallization product upon heating of a corresponding alloy glass, or directly by crystallization during liquid quenching of the melt. Both ways are equally suited to produce such highly metastable key phases. Finally, it is shown that a specific composite material produced along these lines exhibits precisely the characteristics magnetic properties as predicted by the theory.

The optimum microstructure of corresponding materials is a homogeneous distribution of hard phase in a magnetically soft matrix, with the lateral dimensions of both phases being about equal and equal to the critical diameter of the hard phase $b_m \backsimeq b_k \backsimeq b_m$ (e.g., Fig.3.7). In this case, the required volume fraction of the expensive hard phase(s) v_k is small, of the 10%, and if the hard phase is chemically very reactive, e.g., in cases of rare earth compounds, it is protected against corrosion by the soft matrix.

The magnetic behavior of such material is uniquely characterized by a reversible demagnetization curve, e.g., maximum recoil permeability and, in certain cases, also by an unusually high isotropic remanence ratio $m_r=M_r/M_s > 0.5$. With regard to the small portion of hard magnetic phase, the energy product $(BH)_{max}$ is potentially very high, mainly due to the high average saturation induction and the high barrier against irreversible magnetization reversal that may be attained in these composites. In an ideal system recoil curves will not deviate from the major demagnetization curve until the occurrence of irreversible magnetization changes [12].

We have studied the magnetization and demagnetization behavior of nanostructured single-phase and composite materials in order to understand the nature of interactions present in these materials. Inter-particle exchange interactions are known to account the remanence enhancement above the Stoner-Wolfarth limit in both single-phase and composite materials but exchange spring behavior is observed in the nanocomposite magnets. This is characterized by high reversibility in demgnetization curves, recoil permeability values and increased remanence coercivity to intrinsic coercivity ratio.

The two-phase nanocomposite alloy contains a large amount of soft phase, predominately Ŭ-Fe that provides regions of very low anisotropy and permits individual magnetic phase reversal at low internal fields [12]. δM plots indicate exchange type of interactions, but in the nanocomposite samples for fields higher than H_r, magnetostatic interactions become dominant giving rise to negative ŭM values. The negative part is increased in samples with higher soft phase content, as expected. The results of Harland study also provide information concerning the technical magnetic properties of the materials. Decreasing the measuring temperature increases the critical reverse field for appearance of recoil loop hysteresis in the nanocomposite sample, although this critical field is still significantly less than that determined for single-phase alloy. It is seen that the single-phase alloy maintains full exchange coupling to higher reverse fields than does the nanocomposite alloy, but with a smaller overall remagnetization response. The independent reversal of the soft phase in the nanocomposite signals a breakdown in the interphase exchange coupling and thus recoil curves of this material begin to show hysteresis at lower reverse fields than do the recoil curves of the single-phase alloy [12].

The normalized recoil loop area can be used as a measure of the field to which a high degree of exchange coupling is maintained. Using this technique it is then possible to determine the reverse field required to induce hysteresis in the recoil loop which is indicative of a decrease in the system. In this way, the effect of excess Ŭ-Fe in a $Nd_2Fe_{14}B$ alloy can be determined. The two phase alloy shows a higher degree of exchange coupling, but this coupling is maintained to lower the reverse magnetic fields than for single phase materials.

It should be emphasized that this specific material is just one representative example of a large class of two or more phase composites with exchange-spring behavior, which may be produced after the same technological principles as described also at quite different compositions in the same alloy system and likewise in other alloy systems.

From above all discussions, we can point out some characteristics regarding/of this material as follows:

(1) Simultaneous additions of Cu and Nb in $Nd_4Fe_{76}Cu_{0.5}Nb_1B_{18.5}$ gave rise to a stability of grain size of Fe_3B, which stabilized the hysteresis loop parameters for a wide range of annealing temperature.

(2) The sample of composition $Nd_4Fe_{76}Cu_{0.5}Nb_1B_{18.5}$ possesses high remanent ratio of around 0.765 and coercivity 3.30 kOe in the optimum annealing condition. The value of maximum energy product in the optimum annealing condition has been obtained as 9.87 MGOe using applied field of 3T.

(3) Reversible and irreversible magnetization behavior has been examined for all the samples annealed at optimum temperature by using recoil hysteresis and DCD technique.

(4) Recoil hysteresis loops are steep for all the samples having small recoil area and high recoil permeability, which is a characteristic of exchange coupled system. However, areas of the recoil loops are progressively increased with the increase of annealing temperature.

(5) Temperature dependence of hysteresis curves for the composition exhibit variation in shape around the spin reorientation temperature of 100K where field dependence of magnetization is discontinuous.

(6) Chemical modification of the magnetocrystalline anisotropy of the $Nd_2Fe_{l4}B$ compound may be achieved with the substitution of La, Y and Gd for Nd. As these elemental substitutions all exhibit spherical crystal field symmetry, they provide a decrease in the magnetocrystelline anisotropy of the $R_2Fe_{l4}B$ phase and thus are anticipated to foster improved interphase exchange coupling in exchange-spring magnets [2].

References:

[1] Kneller, E. F. and Hawig, R. ñThe exchange-spring magnet: a new material principle for permanent magnets.ò IEEE Trans. Magn. 27 (1991) 3588-3600.

[2] Li, S. D. Sun, W. S. and Quan, M. X. ñCrystallization and magnetic properties of melt-spun two-phase nanocrystalline Nd-Fe-B alloyò Mat. Lett. 30 (1997) 351-355.

[3] Cho, Y. S., Kim, Y. B., Kim, C. S. and Kim, T. S. ñMagnetic properties of new Nd-Fe-B nanocrystalline with Ű-Fe as main phase.ò IEEE Trans. Magn. 32 (1996) 1964-1966.

[4] Jurczyk, M., Collocott, S. J., Dunlop, J. B. and Gwan, P. B. ñMagnetic properties of nanocomposite $(Nd,Dy)_2(Fe,Co,Zr)_{14}B$ and $Nd(Fe,Mo)_{12}N_x$ materials with an excess of Feò J. Phys. D: Appl Phys. 29 (1996) 2284-2289.

[5] Kang, K. Lewis, L. H. Jiang, J. S. and Bader, S. D. *"Recoil hysteresis of Sm–Co/Fe exchange-spring bilayers."* J. Appl. Phys. 98 (2005) 113906 (1-7).

[6] Givord, D., Tenaud, P., and viadieu, T. ñAnalysis of hysteresis loops in N-Fe-B sintered magnetsò J. Appl. Phys. 60 (1986) 3263-3265.

[7] Givord, D., Li, H. S., Perrier R., de la Bathie ñmagnetic properties of $Y_2Fe_{14}B$ and $N_2Fe_{14}B$ single crystalsò Solid State Com. 51 (1984) 857-860

[8] Hadjipanayis, G. C, Hall, C., Kim, A. ñTemperature dependence of magnetic hysteresis in melt-spun and sintered Nd-Fe-B magnetsò IEEE Trans. Magn. 23 (1987)

[9] Withanawasam, L., Murphy, A. S., Hadjipanayis, G. C., and Krause, R. F., *"Nanocomposite $R_2Fe_{14}B$/Fe exchange coupled magnets."* J. Appl. Phys. 76 (1994) 7065-7067.

[10] Withanawasam, L., Hadjipanayis, G. C., and Krause, R. F. *"Enhanced remanence in isotropic Fe-rich melt-spun Nd-Fe-B ribbons."* J. Appl. Phys. 75 (1994) 6646-6648.

[11] Hajipanayis, G.C. and Gong, W., ñMagnetic hysteresis in melt-spun Nd-Fe-Al-B-Si alloys with high remanenceò J. Appl. Phys. 64 (1988) 5559-5561.

[12] Harland, C. L. Lewis, L- H. Chen, Z.and Ma, B.-M. *"Exchange coupling and recoil loop area in $Nd_2Fe_{14}B$ nanocrystalline alloys."* J. Magn. Mag. Mater. 271 (2004) 53-62.

[13] Manjura Haque, S., Khan, F.A., and Hakim, M.A, ñExchange-Spring behavior of nanocrystalline $(NdPr)_4Fe_{71}Co_5Cu_{0.5}Nb_1B_{18.5}$.ò Phys. Stat. sol. (a), (2007) 1-9.

[14] Dahlgren, M., Kou, X. C., Grossinger, R., Liu, J. F., Ahmed, I., Davies, H. A., and Koji Yamada ñCoercivity and Spin Reorientation Transitions in Nd-Fe-B

Nanocomposites Prepared By Meltspining.ò IEEE. Transaction on Magnetics, vol 33. No 3, (1997).

[15] Panagiotopolos, I., Withanawasam, L., Hadjipanayis G. C., ñExchange-Spring behavior in nanocomposite hard magnetic materialsò. Journal of magnetism and magnetic materials 152 (1996) 353-358.

[16] Suessa, D., Schrefl, T., Fähler, S., Kirschner, M., Hrkac, G., Dorfbauer, F., and Fidler, J., ñExchange spring media for perpendicular recordingò. Appl. Phys. Let., 87, (2005b) 012504.

[17] Schrefl, T., Fidler, J., Kronmüller, H. ñRemanence and coercivity in isotropic nanocrystalline permanent magnetsò. Phys. Rev. B 49 (1994) 6100-6110.

[18] Coehoorn, R., de Mooji, D. B., Duchateau, J. P. W. B. and Buschow, K.H.J. ñNovel permanent magnetic materials made by rapid quenching ò. J. de phys. 49(8) (1988) 669-670.

[19] Coehoorn, R., de Mooji, D. B. and de waard, C. ñMeltspun permanent magnet materials containing Fe_3B as the main phaseò J. Magn. Magn. Mater. 80 (1989) 101-104.

[20] Manaf , A., Leonowicz, M., Davies, H. A. and Buckley, R. A. ñEffec of grain size and microstructure on magnetic properties of rapidly solidified $Fe_{82.4}Nd_{13.1}B_{4.5}$ alloyò J. Appl. Phys. 70 (1991) 6366-6368.

[21] Manaf, A., Buckley, R.A., and Davies, H. A. ñNew nanocrystalline high remanence Nd-Fe-B alloys by rapid solidificationò J. Magn. Magn. Mater. 128 (1993) 302-306.

[22] J. J. Croat, ñCrystallization and magnetic properties of melt-spun neodymium-iron alloysò *J. Magn. Magn. Mat.,* vol. 24. (1981) p. 125.

[23] J. J. Croat, J., F. Herbst, R. W. Lee, and F. E. Pinkerton, ñPr-Fe and Nd-Fe-based materials: A new class of high-performance permanent magnets (invited)ò J. Appl, Phys., vol. 55. (1984) p. 2078.

[24] J. J. Becker, ñRapidly quenched metals for permanent magnet materials (invited)ò J. Appl. Phys., vol. 55, (1984) p.2067.

[25] K. H. J. Buschow, D. B. dc Mooij and H. M.van Noort, ñProperties of metastable ternary compounds and amorphous alloys in the Nd-Fe-B system.ò J. Less. Common Metals, vol. 125, (1986) p. 135.

[26] K. H. J. Buschow, D. B. dc Mooij and R. Coehoorn, ñMetastable ferromagnetic materials for permanent magnet.ò J. Less. Common Metals, vol. 145, (1988) p. 601.